





**ALEKSANDR LISSOVSKI**

Pulsed high-pressure discharge in argon:  
spectroscopic diagnostics,  
modeling and development



TARTU UNIVERSITY  
**PRESS**

This study was carried out at the Institute of Physics, University of Tartu, Estonia.

The Dissertation was admitted on July 2, 2010, in partial fulfilment of the requirements for the degree of Doctor of Philosophy in physics (optics and spectroscopy) and allowed for defence by the Council of the Institute of Physics, University of Tartu.

Supervisor: Dr. Alexey Treshchalov, Institute of Physics,  
University of Tartu, Estonia

Opponent: Dr. Andreas Ulrich, Technical University of Munich, Germany

Defence: September 7, 2010, at the University of Tartu, Estonia

ISSN 1406–0647  
ISBN 978–9949–19–434–6 (trükis)  
ISBN 978–9949–19–435–3 (PDF)

Autoriõigus: Aleksandr Lissovski, 2010

Tartu Ülikooli Kirjastus  
[www.tyk.ee](http://www.tyk.ee)  
Tellimus nr. 401

# CONTENTS

LIST OF PUBLICATIONS.....	7
1. INTRODUCTION.....	9
2. GENERAL BACKGROUND.....	11
2.1. VUV emission features of rare gas dimers and energy levels of argon.....	11
2.2. Methods of gas excitation .....	14
2.3. Diagnostics of excited species in plasma .....	15
2.4. Excitation regimes for VUV excimer lamp and laser .....	17
3. EXPERIMENTAL SETUP AND PROCEDURES .....	19
3.1. The object of investigation and electrical schemes for the discharge excitation .....	19
3.2. Experimental setup for VUV-VIS spectroscopic diagnostics of the discharge.....	21
3.3. Optical schemes for imaging diagnostics of the discharge.....	23
3.4. Scheme for the dye laser absorption probing of the discharge .....	24
4. SPATIAL STRUCTURE AND SURVEY VUV-VIS SPECTRA OF THE DISCHARGE .....	26
4.1. Images of the discharge .....	26
4.2. Longitudinal fragmentation of the discharge.....	28
4.3. Survey spectra of the discharge .....	31
5. THE NATURE AND MODELING OF UV-VIS CONTINUUM.....	34
5.1. Spectra of UV-VIS continuum in the pulsed arc and homogeneous discharges .....	34
5.2. Kinetics of UV-VIS continuum and Ar <sup>**</sup> red lines.....	39
6. KINETICS OF KEY SPECIES IN PLASMA .....	42
6.1. Emission and absorption bands (lines) used for the diagnostics.....	42
6.2. Kinetic model.....	44
6.3. Comparison of the experimental and modeling kinetics.....	47
6.4. The role of electrons in the formation of Ar <sub>2</sub> <sup>*</sup> excimers.....	51
6.5. Conditions for amplification of VUV emission from Ar <sub>2</sub> <sup>*</sup> excimers.....	53
7. THE THIRD CONTINUUM EMISSION IN THE DISCHARGE AT A REDUCED PRESSURE .....	56
7.1. About the nature of the third continuum .....	56

7.2. Spatial structure and time dependent spectra of the third continuum emission.....	58
7.3. The excitation mechanism of the third continuum.....	60
7.4. The modeling of the third continuum emission kinetics.....	64
7.5. Emission of 190 nm band in the afterglow stage.....	65
SUMMARY.....	67
SUMMARY IN ESTONIAN.....	69
ACKNOWLEDGEMENTS.....	71
REFERENCES.....	72
PUBLICATIONS.....	77
CURRICULUM VITAE (CV).....	143
ELULOOKIRJELDUS (CV).....	144

## LIST OF ORIGINAL PUBLICATIONS

### List of publications included to the thesis:

- I. A. Lissovski, A. Treshchalov, “VUV-VIS imaging of high-pressure pulsed volume discharge in argon”, *IEEE Transactions on Plasma Science* **36**(4), 958–959 (2008)
- II. A. Treshchalov, A. Lissovski, “VUV-VIS spectroscopic diagnostics of a pulsed high-pressure discharge in argon”, *Journal of Physics D: Applied Physics* **42**, 245203 (14pp) (2009)
- III. A. Lissovski, A. Treshchalov, “Emission of the third continuum of argon excited by a pulsed volume discharge”, *Physics of Plasmas* **16**(12), 123501 (9pp) (2009)
- IV. A. B. Treshchalov; A.A. Lissovski, “Spectroscopic diagnostics of a pulsed discharge in high-pressure argon”, *Quantum Electronics* **40**(3), 234–240 (2010)
- V. A. Treshchalov, A. Lissovski, “VUV-VIS imaging of high-pressure pulsed discharge in argon”, *Proc. SPIE: Atomic and molecular pulsed lasers VII* **6938**, 69380Y (10pp) (2008)
- VI. A. Treshchalov, A. Lissovski, “Dye laser absorption probing of high-current pulsed volume discharge in argon”, *Proc. SPIE: Atomic and Molecular Pulsed Lasers VI* **6263**, 62630L (8pp) (2006)

### List of other publications, related to the current work:

1. A. Lissovski, A. Treshchalov, “Spatial-time modulations of VUV-VIS emission of high pressure pulsed volume discharge in argon”, *Proc. XXVIII International Conference on Phenomena in Ionized Gases (ICPIG)*: (Eds.) J. Schmidt, M. Šimek, S. Pekárek, V. Prukner, Inst. Physics Acad. Sci. Czech Republic, 1135–1138 (2007)
2. A. Treshchalov, A. Lissovski, “Spatial-time modulation in VUV and VIS emission of pulsed argon discharge at high pressure” (in Russian), *Proc. Conf. on Physics of low temperature plasma – 2007*: (Ed.) A. D. Hahaev, Russia, 69–73 (2007)
3. A. Lissovski, A. Treshchalov, “Kinetics of VUV-VIS spontaneous emission of high-current pulsed volume discharge in argon”, *Proc. SPIE: Atomic and Molecular Pulsed Lasers VI* **6263**, 62630H (10pp) (2006)
4. G. Gerasimov, R. Hallin, B. Krylov, A. Treshchalov, A. Morozov, A. Lissovski, G. Zwereva, A. Arnesen, “The Intense VUV narrow band emission from an inert gas mixture discharge”, *Proc. SPIE: Atomic and Molecular Pulsed Lasers VI* **6263**, 626311 (6pp) (2006)
5. A. Lissovski, A. Treshchalov, “VUV-VIS spectroscopic study of pulsed high-pressure volume discharge in argon”, *Proceedings of 18-th Europhysics Conference on the Atomic and Molecular Physics of Ionized Gases: July 12–16, 2006*, European Physical Society, 117–118 (2006)

6. A. Treshchalov, A. Lissovski, E. Chikeev, “High-current discharge pumping of ArF, F2 lasers without cathode hot spots and filament instabilities”, *Proc. SPIE: Atomic and Molecular Pulsed Lasers IV* **4747**, 253–260 (2002)

**Author’s contribution**

The author participated actively in spectroscopic and optical measurements and data analyses, in preparation of all accompanying publications and conference presentations. He developed the kinetics model for argon plasma and did all modeling calculations.

# I. INTRODUCTION

For more than three decades, the rare gas dimers ( $R_2^*$ ) have attracted spectroscopists and laser physicists because these molecules are known as very efficient sources of vacuum ultraviolet (VUV) radiation. The origin of this radiation is the well-known second continuum band ( $Ne_2^*$  - 96 nm,  $Ar_2^*$  - 126 nm,  $Kr_2^*$  - 147 nm,  $Xe_2^*$  - 172 nm), caused by transition from the vibrationally relaxed bound excited electronic  $R_2^*$  state to the repulsive potential in the ground state. The interest to VUV spectral range is connected with the capability of high-energy photons to split most of the chemical bonds both in organic and inorganic materials, thus various scientific and industrial applications in photochemistry, surface cleaning and material deposition processes is possible. Nowadays this field of activity is covered mostly by compact low-intensity VUV excimer lamps, excited by the dielectric barrier discharge [1–4] and the electron beam [5]. High conversion efficiency of up to 42% (VUV emitted light energy/deposited energy) has been obtained for these devices at the low excitation power density and medium gas pressure (lower than 1 bar).

For the operation of  $R_2^*$  excimer lasers, excitation conditions should be quite different from that, optimized for excimer lamps. The small radiative lifetime and broad spectral width of bound-free  $R_2^*$  transitions require an extremely high excitation power density, while high pressure (tens of bars) is necessary to ensure that the excimer formation is faster than the radiative decay. It explains why the operation of  $R_2^*$  excimer lasers has been achieved so far only by powerful electron beam pumping:  $Xe_2^*$  [6–9],  $Kr_2^*$  [10] and  $Ar_2^*$  [11]. These devices are usually very bulky and expensive. Therefore, the development of discharge-pumped  $R_2^*$  VUV lasers is an important and demanding task. Several discharge schemes for the pulsed excitation of rare gases at high pressure have been tested to achieve the laser threshold [12–17], but these attempts have not been successful as yet. The first lasing effect was demonstrated in [18] for  $Kr_2^*$  excimers under the discharge excitation of Kr at 9 bar (the laser wavelength 148 nm, pulse energy  $\sim 150 \mu J$ ). Very low efficiency and small pulse energy of this laser provoke discussion in the scientific community and has not been explained as yet.

Many of applied problems in high-current, high-pressure discharges are very difficult to solve without a detailed understanding of the basic physical and chemical processes that determine the properties and evolution of non-stationary, non-equilibrium discharge plasma. The reliable spectroscopic diagnostic data for energy flow kinetics in plasma is of great importance for a successful development of discharge-excited VUV light sources. Quantitative experimental data about densities of key excited atomic and molecular species are necessary for the estimation of discharge pumping efficiency and how close to the lasing threshold conditions we are able to approach in the real discharge devices.

The aim of the present thesis is the experimental and modeling study of high-pressure (1–10 bar) argon plasma under high-power pulsed volume discharge excitation to reveal the processes, which have influence to the production of key atomic and molecular excited species and visible-vacuum ultraviolet (VIS-VUV) emission of plasma in the breakdown and recombination stages of the discharge.

Spatial-time spontaneous emission and dye laser absorption probing data were used for the diagnostics of several electron-assisted processes (excitation, recombination, mixing, quenching) which are especially actual under the powerful pulsed excitation. The quality of the discharge was monitored by VUV-VIS imaging techniques with nanosecond time resolution.

The thesis is organized as follows.

The general background is given in Chapter 2. The general VUV emission features and schematic energy level diagram of argon are discussed in this chapter. The existed experimental methods for argon excitation and diagnostics of excited species as well as the estimation of the VUV amplification properties of the active medium consisted of  $\text{Ar}_2^*$  excimers are briefly overviewed.

Chapter 3 describes electrical circuits for the discharge excitation and several experimental schemes (procedures) used for the plasma diagnostics in this thesis.

The structure and spatial-time behaviour of the discharge in argon and survey VUV-VIS spectra are presented in Chapter 4 (Papers I, II, IV and V).

The nature and modeling of UV-VIS continuum in argon discharge plasma is discussed in Chapter 5 (Papers II and IV).

The experimental and modeling data for the densities of key species in argon discharge plasma are presented in Chapter 6 (Papers II, IV, and VI). The threshold density needed to obtain lasing at 127 nm on  $\text{Ar}_2^*$  excimers and possibilities of the laser operation under the discharge excitation are discussed.

Chapter 7 is dedicated to the observation of discharge-excited emission of the third continuum in argon (Paper III).

The summaries in English and Estonian highlight the main results and conclusions of this thesis.

Supplementary data (video-files of discharge images) are available from <http://hdl.handle.net/10062/15133>

## 2. GENERAL BACKGROUND

### 2.1. VUV emission features of rare gas dimers and energy levels of argon

In the rare gas light sources the broad VUV continuum emission is the most interesting feature which has been attracted the attention of spectroscopists. At high gas pressure the spectral shapes of continuum bands for different gases look very similar and don't depend on the methods of gas excitation (e-, proton-, ion-beams [19–22],  $\alpha$ -particles [23], discharge [1–4]). Figure 1 shows e-beam (13 keV) excited  $R_2^*$  excimer emission spectra of Xe, Kr, Ar, Ne and He gases at 1 bar [24]. At reduced pressures spectra change significantly. As an example, in the insert of Fig. 1 one can see that along with partly self-absorbed resonant  $Ar^*$  lines at 104.8 and 106.7 nm (they are not resolved in this spectrum), two bands are observed: the first (109 nm) and the second (127 nm) continuum.

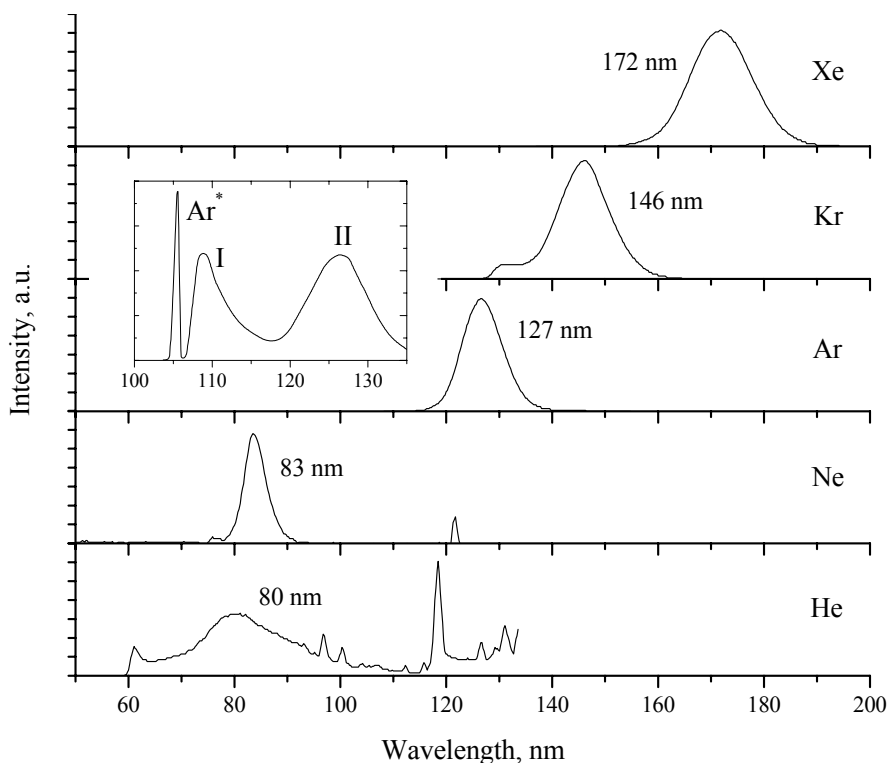


**Figure 1.**  $R_2^*$  excimer emission spectra of Xe, Kr, Ar, Ne and He gases at 1 bar [24]. The electron beam (13 keV) excitation was used. **Insert:** VUV spectrum of argon by excitation of 4-MeV proton at 0.26 mbar [25].

To illustrate the origin of these continua we used as an example schematic energy level diagram of argon (see Fig. 2), since other rare gases have similar molecular structure. The ground state for  $R_2$  molecules are basically repulsive except for a weak Van der Waals binding for Kr and Xe. At the same time, all rare gases form stable positive  $R_2^+$  diatomic ions with a strong binding in its lowest  $^2\Sigma_u^+$  state. Numerous bounded and repulsive  $R_2^{**}$  molecular states are also formed from  $R^{**}$ ,  $R^*$  atomic states [26, 27].

As the argon discharge is the object for investigation in this work, some details about  $Ar_2^*$  states are presented below. The bound  $Ar_2^+$  ionic  $^2\Sigma_u^+$  state has the well depth of 1.25 eV with the minimum at 2.43 Å [28–30]. The ground state repulsive curve has been well defined in [31]. The well depth of the  $^3\Sigma_u^+$  excimer potential was determined as 0.78 eV [32]. Based on the theoretical estimate of the spin-orbit effect, the singlet  $^1\Sigma_u^+$  excimer state lies between 0.074 and 0.1 eV above the triplet  $^3\Sigma_u^+$  state [27].

Of particular importance for the relaxation processes following the electron-impact excitation at high gas density, are the curve crossings and the high density of states that allow the energy to flow easily from the initial states to the final radiative excimer. Thus an atomic  $Ar^+$  ion, associated with Ar atom in three-body collision, relaxes to the bottom of the  $Ar_2^+$  well, then recombines with an electron and dissociates to an intermediate  $Ar^{**}$  excited state. From this state by collision with another Ar atom, it falls down to the lowest excited atomic manifold ( $Ar^*$ , 4s). From there it finally associates in three-body collisions with Ar atom into the  $^1, ^3\Sigma_u^+$   $Ar_2^*$  excimer states which do not interact with the ground state and can only decay by radiation with time constants of 4.2 ns (singlet state) [33] and 2.8  $\mu$ s (triplet state) [33]. The first continuum is ascribed to transitions from high vibrational levels of the lowest excited  $^1, ^3\Sigma_u^+$   $Ar_2^*$  excimer states to the ground state  $^1\Sigma_g^+$ ; and the second continuum band originates from the low lying vibrational levels of these excimers. The theoretical conversion efficiency of the second continuum emission of argon at 127 nm (quantum energy of about 9.85 eV) can achieve 62.5 % in assumption, that minimal energy of 15.75 eV for ionization of argon atom is expended. This value is rather close to the experimentally obtained efficiency under the excitation by low-power continuous electron beam [5].

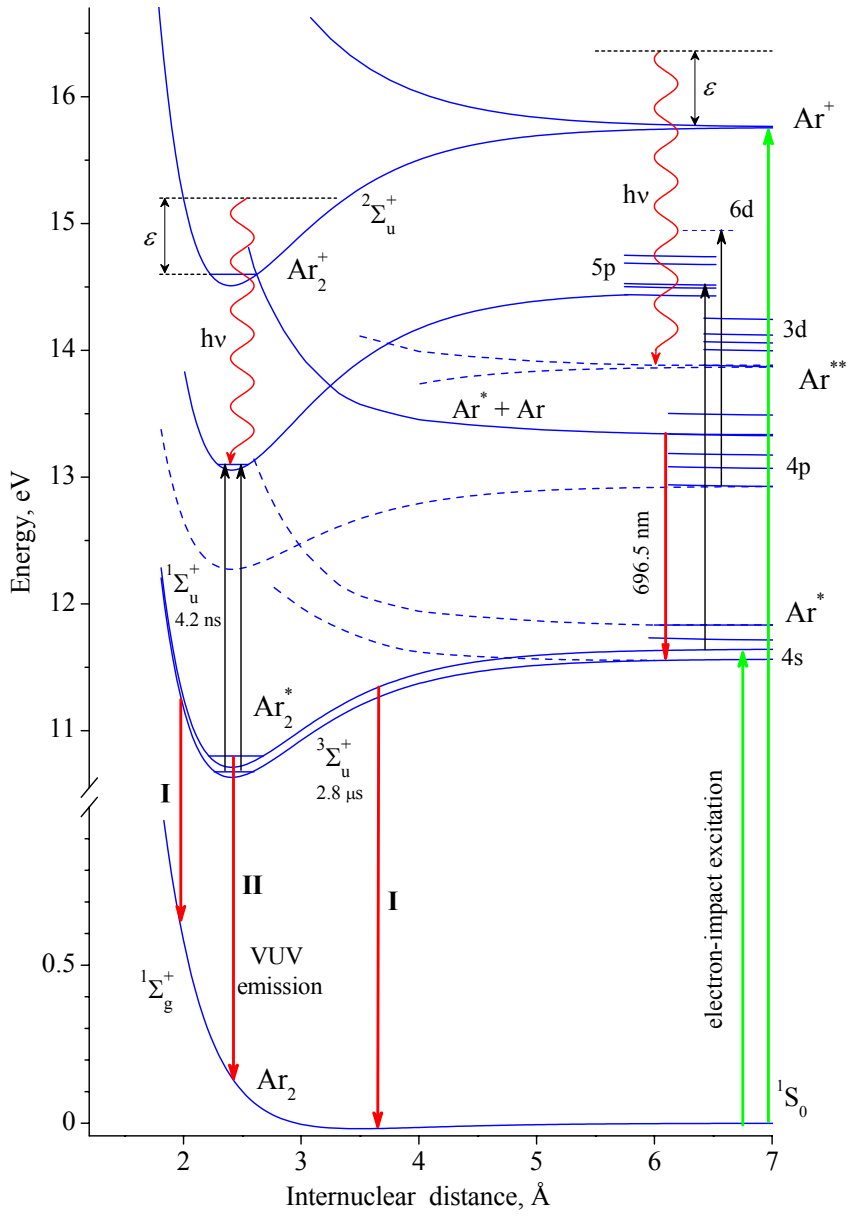


**Figure 2.** Schematic energy level diagram of argon. The absorption (emission) transitions used for the diagnostics in this work are shown by upward (downward) arrows.

## 2.2. Methods of gas excitation

The existed gas excitation methods can be divided by different types of plasma creation: beam, photon and discharge excitation. Further we consider their advantages and shortcomings.

**Beam-excitation:** this class of excitation includes the excitation by electron-, proton-beams, and also by various heavy projectiles from  $\alpha$ -particles to ions. The beam is usually formed in a high vacuum part of the setup and injects into a gas through a thin foil. Thickness and material of these foils determine the energy which is necessary to deposit into the gas by projectile particles. Usually beam generators need huge devices such as accelerators, where beams achieve energies of about several MeV. This makes difficult to use such systems in commercial applications. Another disadvantage is connected with large energy losses during the passing of the beam through the metal foil accompanying with roentgen radiation. The elegant decision of this problem has been recently demonstrated [34] by using thin ceramic membrane as the entrance foil for the low-energy (10 to 20 keV) electron beam. At a thickness of about 300 nm and 1 mm size, membranes made from silicon nitride can withstand pressure differentials up to 5 bar and demonstrate less than 10 % loss in the membrane. Vacuum tight metal foils are typically 10 times thicker and it requires electron energies of at least 50 keV for 10% loss in the foil. A practical advantage of the novel foil is that accelerating voltages below 20 keV are easy to handle. This technique, operated in pulsed or continuous modes, is very effective for excitation of dense rare gases and applies in commercially available compact excimer lamps.

**Photon excitation:** this type of excitation has no big practical importance, but provides some benefits in comparison with the beam and discharge excitations in investigations of energy level structure of excimers and their decay kinetics. For example, VUV synchrotron radiation in selected narrow wavelength range permits one to excite specific  $R^*$  atomic and  $R_2^*$  molecular states without gas ionization [35]. It excludes the presence of electrons and their participation in formation (quenching) processes of excited species. In such experiments, two components of spontaneous emission decay from  $Ar_2^*$  – singlet  $^1\Sigma_u^+$  (fast emitted species) and triplet  $^3\Sigma_u^+$  (long-lived species) have been easily separated. The same excitation is possible to achieve with multiphoton processes in the focus of the laser beam, which however leads at very high photon intensity to the optical breakdown. Laser-induced breakdown of high-pressure argon ( $\sim 10$  bar), in the focus of Ti:sapphire laser (pulse duration of 150 fs, wavelength 780 nm and laser intensity of about  $10^{15}$  W cm $^{-2}$ ) was used in [36, 37] to demonstrate the amplification of  $Ar_2^*$  radiation at 126 nm (small-signal gain coefficient of about 0.05 cm $^{-1}$  was obtained). The shortcomings of such method are the very expensive equipment and the low efficiency of the excitation.

**Discharge excitation:** this is the most widespread and the least expensive method for plasma creation. The main advantages of the discharge devices are compactness, high efficiency and relatively low energy consumption. In general case, the discharge excitation could be described as a breakdown of a gas when the voltage between electrodes exceeds the critical value. Thus, the energy deposited into the gas is determined by the resistance of plasma and duration of the discharge current. The main problem of high-pressure gas discharge is its instability, which leads very quickly to constriction and transformation of the volume discharge to the arc [38, 39]. Therefore, it is impossible to carry out the volume discharge in direct current mode and pulsed mode operation is necessary at high pressure.

Pulsed volume discharge is realized when a high-voltage with a very steep front (about 1 kV/ns) is applied to the discharge gap. It is well known that during pulsed excitation the gap can endure the overvoltage several times higher than the static breakdown voltage [40]. Along with overvoltage, several other criteria should be satisfied to avoid constrictions in the discharge (intense and uniform preionization, short rise time for the discharge current, uniform electric field in the discharge gap...).

### 2.3. Diagnostics of excited species in plasma

Several spectroscopic methods are used for the diagnostics of discharge plasma. Temporal behaviours of excited species are usually measured by spontaneous emission technique. In application to a high-pressure discharge in argon excited by a pulsed discharge, the main emitted species are  $\text{Ar}^{**}$  atoms (strong red lines) and  $\text{Ar}_2^*$  excimers (strong VUV emission of the second continuum). The emission from the lowest excited  $4s \text{ Ar}^*$  states (see Fig. 2) is absent. Two of them are metastables, therefore radiation from these states is forbidden; and two VUV resonance lines emitted from  $4s$  states are strongly reabsorbed due to the high gas density. At the same time reabsorption of VUV emission from  $\text{Ar}_2^*$  excimers is absent because their ground state is repulsive.

Spontaneous emission provides information only about the relative populations of excited species in plasma. For determination of their absolute densities the absorption probing technique is used. According to the Beer–Lambert law, the intensity of the probing beam decreases exponentially along the length  $l$ , in assumption of uniformly distributed absorption species:

$$I(\lambda) = I_0 \cdot \exp(-\kappa_\lambda \cdot l) \quad (1)$$

where  $\lambda$  is the wavelength of the probing radiation,  $\kappa_\lambda$  is the absorption coefficient. The absorption coefficient at the centre of the Lorencian spectral line with the bandwidth  $\Delta\lambda_L$  (full-width at half-maximum, FWHM) is expressed by formula (2) [41]:

$$\kappa = \frac{g_k}{g_i} \frac{\lambda_{ki}^4}{4\pi^2 c} \frac{A_{ki}}{\Delta\lambda_L} N_i \left( 1 - \frac{g_i}{g_k} \frac{N_k}{N_i} \right) \quad (2)$$

where  $g_i$  and  $g_k$  are the statistical weights of the lower  $i$  and upper  $k$  levels respectively,  $\lambda_{ki}$  – the transition wavelength,  $c$  – velocity of light,  $A_{ki}$  – the spontaneous emission probability,  $N_i$  and  $N_k$  – the population densities of excited species on the levels  $i$  and  $k$  respectively.

The term  $\frac{g_i}{g_k} \frac{N_k}{N_i}$  in formula (2) can be neglected, because in the afterglow stage of high-pressure discharge  $N_i \gg N_k$  due to the fast collisional quenching cascades  $\text{Ar}^{**} + \text{Ar} \rightarrow \text{Ar}^* + \text{Ar}$  [42, 43]. Thus, in this approximation the population  $N_i$  on the probing level can be presented as follows:

$$N_i = 4\pi^2 c \frac{g_i}{g_k} \frac{\kappa}{\lambda_{ki}^4} \frac{\Delta\lambda_L}{A_{ki}} \quad (3)$$

The absorption probing technique is easily applied for  $\text{Ar}^*$  atomic levels, because the reliable data of  $A_{ki}$  coefficients are available for many  $\text{Ar}^*$  atomic transitions [44].

Along with  $\text{Ar}^*$  atomic lines several transitions between excited states of  $\text{Ar}_2^*$  excimers have been investigated by absorption probing spectroscopy of argon under the electron-beam and pulsed corona discharge excitation [45–47]. The main molecular absorption bands are attributed to transitions from the long-lived lowest triplet  $\text{Ar}_2^*$  state  $4s, {}^3\Sigma_u^+$  to the manifold of higher excited molecular  $np, nf$  Rydberg states. At high gas pressure the rotational structure of these transitions is not resolved due to pressure broadening and produces broad red-shaded bands. Formula (3) is inapplicable in this case, because the correspondent data for  $A_{ki}$  coefficients are absent. For monitoring the density  $N_{\text{mol}}$  of triplet  ${}^3\Sigma_u^+ (v=0)$  excimers at pressure  $p$  we used the simplified formula (4):

$$N_{\text{mol}} = \kappa_p \frac{\Delta\lambda_p}{\Delta\lambda_1 \sigma_1} \quad (4)$$

where the absorption cross section  $\sigma_1$  for  $4s, {}^3\Sigma_u^+ (v=0) \rightarrow 5p, {}^3\Sigma_g^+ (v=0)$  band at 512.0 nm for argon pressure of 1 bar has been determined in [48]:  $\sigma_1 = (3.3 \pm 0.5) \times 10^{-16} \text{ cm}^2$ .  $\kappa_p$  and  $\Delta\lambda_p$  are the experimentally measured absorption coefficient and molecular band width (FWHM) at gas pressure  $p$  respectively. The probing absorption and spontaneous emission transitions used for the diagnostics in this work are shown in Fig. 2 by upward (download) arrows.

## 2.4. Excitation regimes for VUV excimer lamp and laser

To consider formation kinetics of rare gas excimers, we assume that the gas is ionized by a short single pulse excitation (see Fig. 3). The peak of VUV emission delays from the excitation pulse because of the finite time required for several plasm-chemical reactions. The gas pressure has a significant role, because the rates of key reactions (dimerization of  $R^+$  ions, formation of  $R_2^*$  excimers) increase quadratically with this parameter. At relatively low gas pressure (lower than 1 bar), which is used in excimer lamps, the VUV emission kinetics is slow and the peak density of excimers is low. However, the time-integrated emission energy can be reasonably high. This high-efficient regime is obtained usually at low power excitation conditions.

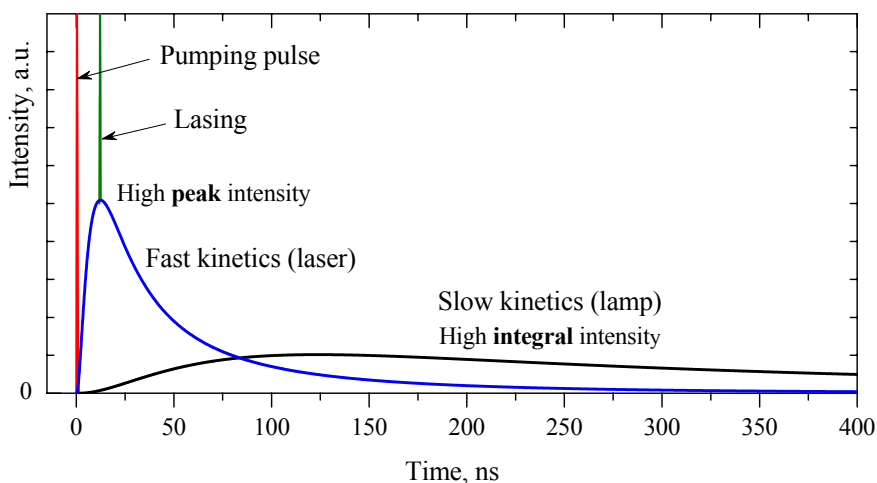


**Figure 3.** Idealized kinetics for VUV emission of rare-gas excimer molecules after a short single pulse excitation.

The optimal excitation conditions for lamps are different comparing with the excimer laser, where achievement of a high peak density of excimers is a key parameter. Thus powerful pumping and very high gas pressure are needed for the acceleration of plasm-chemical reactions. At high pumping power density, these reactions can be quite different from low-power excitation conditions – for example electron-assisted processes (mixing, quenching) are especially actual.

The excimer laser active medium is characterized by the gain coefficient  $g_0$  (in  $\text{cm}^{-1}$ ). To estimate the amplification properties of the active medium, consisting of  $\text{Ar}_2^* \ ^1\Sigma_u^+(v=0)$  excimer molecules with the density  $N$  (in  $\text{cm}^{-3}$ ), we

applied the formula for the gain coefficient  $g_0$  (in  $\text{cm}^{-1}$ ) used, for example, in [49]:

$$g_0 = \frac{\lambda^4 A_{21}}{8\pi c \Delta\lambda} N = 1.2 \times 10^{-17} N \quad (5)$$

where  $\lambda = 127 \text{ nm}$  is the peak wavelength of the second continuum band,  $A_{21} = 2.4 \times 10^8 \text{ s}^{-1}$  [33] is the radiative transition probability of  $\text{Ar}_2^* \text{ } ^1\Sigma_u^+$  excimers,  $\Delta\lambda$  is the spectral width (FWHM, in nm) of the emission band. According to the experimental [50] and calculated [51] data,  $\Delta\lambda$  for the spontaneous emission of  $\text{Ar}_2^* \text{ } ^1\Sigma_u^+(v=0)$  excimers is 7.1 nm. The minimal gain which is usually considered in the literature for the theoretical estimation of the excimer lasing threshold is about  $0.01 \text{ cm}^{-1}$ . Such gain can be obtained, according to formula (5), with the excimer density of about  $10^{15} \text{ cm}^{-3}$ . This value is about two orders of magnitude higher than for the well-developed rare gas halide exciplex lasers, such as ArF, KrF, XeCl [52]. This estimation shows that the development of discharge-pumped  $\text{R}_2^*$  excimer lasers is a very challenging task.

### 3. EXPERIMENTAL SETUP AND PROCEDURES

#### 3.1. The object of investigation and electrical schemes for the discharge excitation

The object of research is the argon plasma created by a pulsed discharge between two parallel cylindrically profiled electrodes. The gas pressure depending on the assigned task was varied from 0.17 to 10 bar. The electrodes made from tungsten and nickel had the length of 25 and 220 mm respectively. The gap spacing in all experiments was 1.4 mm and the width of the discharge was about 1 mm. As an illustration, the typical image of the pulsed discharge in argon, measured by ns-gated ICCD (intensified charge coupled device) camera, is shown in Fig. 4. To avoid the constriction of the discharge and to achieve a highly efficient VUV emission a thyatron-switched (commutator HY-11 (EG&G)) charge transfer compact circuits were designed. Two circuits, which electrical schemes are shown in Fig. 5, were used to investigate the discharge in different excitation regimes: high-current (scheme a) and low-current (scheme b) excitation. For the scheme (a) the storage capacitor  $C_0$  transfers its energy to the peaking capacitor  $C_p$  after the triggering of the thyatron. This transfer occurs through a sliding discharge on a sapphire plate (with a thickness of 0.6 mm) that was placed laterally to the cathode electrode. A sliding

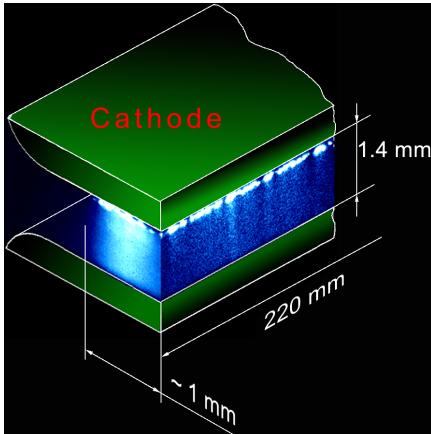


**Figure 4.** The typical image of the investigated discharge: Ar pressure – 4 bar; delay – 16 ns from the breakdown; exposure time – 4 ns; Ni electrodes; optical filter bandwidth – 400–680 nm.

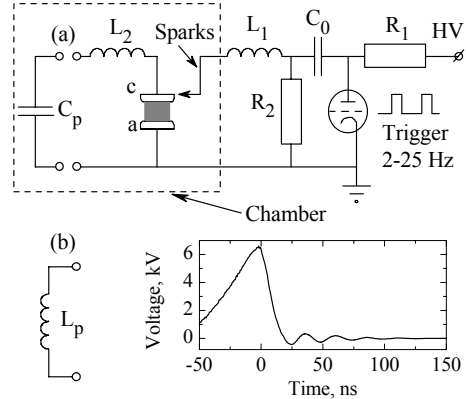


**Figure 5.** Electrical circuits for the discharge excitation. Two schemes were used for different regimes: high-current (a) and low-current (b) excitation. Lower insert shows the voltage on the discharge gap for 4 bar of Ar (scheme (a),  $\rho = 0.56 \Omega$ ).

discharge was used as a powerful and very homogeneous automatic VUV preionization for the main discharge. More experimental details about the design and characteristics of the sliding discharge are available in [53–56]. The peaking capacitors (KVI-3 doorknob high-frequency ceramic capacitors) were placed inside the chamber along the cathode as close as possible to the discharge. This design ensures a very low inductance  $L_2$  (several nH) and allows for a steep current build-up of the main discharge, resulting in a high-power energy deposition to the gas. The values of  $C_0$ ,  $C_p$  and  $L_2$  can be varied according to the required excitation regimes. The active resistance of the peaking circuit inside the chamber is mainly concentrated in the plasma; the resistance of contacts is negligible.

From the electrotechnical point of view, the energy from the peaking capacitor can be effectively transferred to the discharge plasma during a single excitation pulse without oscillations only under the overdamped or the critically damped regime, where the plasma resistance  $R_{pl}$  is more or close to  $2\rho$ , defined as  $\rho = (L_2 C_p^{-1})^{0.5}$ . For a powerful discharge in high-pressure argon this condition is very difficult to fulfil and the plasma resistance usually falls below  $2\rho$  (underdamped regime) just after the breakdown, thus the energy deposition spreads out in time from a single pulse to several successive peaks. High-voltage 75 MHz probe P 6015 (Tektronix) and 500 MHz digital oscilloscope TDS 3054B (Tektronix) were used to measure the voltage difference between the anode and the cathode. In the data analysis, these signals were carefully corrected for the inductance of the excitation circuit. As an example, the voltage on the discharge gap for 4 bar of Ar and low-inductive peaking circuit ( $L_2 = 2.3$  nH,  $C_p = 7.7$  nF,  $\rho = 0.56$   $\Omega$ ,  $f = 37$  MHz) is shown in Fig. 5. This waveform indicates that the real energy deposition to the plasma is a superposition of the first powerful breakdown pulse and several successive weak peaks – an analogue of damped radio frequency excitation ( $f \sim 10$ – $100$  MHz). The frequency  $f = 1/2\pi (L_2 C_p)^{0.5}$  is dependent only on  $L_2$  and  $C_p$  parameters because the plasma resistance is much lower than  $2\rho$ . The discharge current was difficult to measure correctly because of the very compact peaking circuit; therefore the deposition power to the discharge could be only estimated. According to this estimation for the circuit with low  $\rho$ , during the first excitation pulse of about 7 ns, 80 % of the energy, stored in the peaking capacitor, is deposited into the volume discharge. At 4 bar of Ar, the maximal spatially averaged current and excitation power density are estimated as 4 kAcm<sup>-2</sup> and 50 MWcm<sup>-3</sup>, respectively.

Secondary discharge pulses complicate the interpretation of experimental results and the modeling of plasma-chemical kinetics. To avoid this problem the scheme (b) in Fig. 5 was used, where the peaking capacitor  $C_p$  was replaced by the inductor  $L_p = 500$  nH. The role of inductor is to transfer a sliding discharge current which is necessary for preionization. After the breakdown the energy stored in  $C_0$  is loaded into the discharge from a thyatron contour with a high  $\rho$  parameter. This excitation regime gives very homogeneous single pulse

(duration of about 10 ns) weak excitation of the discharge with a reduced current density in the pressure range of 0.17–3 bar. The resistance of the discharge plasma remains relatively high during this excitation.

### 3.2. Experimental setup for VUV-VIS spectroscopic diagnostics of the discharge

Spontaneous emissions of the discharge in the VUV-UV and UV-VIS spectral ranges were measured by two independent schemes, which are shown in Fig. 6. The image of the discharge was directed into the entrance slit of the spectral devices by the concave aluminium mirror objective. The slit served as a spatial filter, allowing to separate the emission from different zones across the discharge (positive column and near electrode zones). The observation axis was slightly tilted from the long axis of the discharge and a 2 mm diaphragm was placed on the output MgF<sub>2</sub> windows of the chamber to avoid any stray light from the sliding discharge and defocused light from other discharge regions. This geometry made it possible to reduce the depth of the emitted plasma zone to several millimetres. As a consequence, the possible reabsorption effects have been minimized.

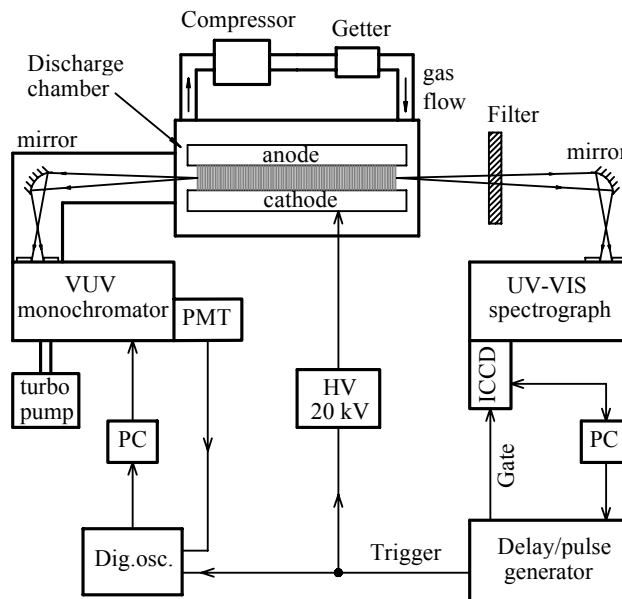


**Figure 6.** Schematic of VUV-VIS spectroscopic diagnostic apparatus.

The UV–VIS emission of the plasma was detected by 0.3 m, f/4 Shamrock 303i imaging spectrograph (Andor Technology) with 300 lines  $\text{mm}^{-1}$  grating (with a resolution of 0.27 nm  $\text{pixel}^{-1}$ ) and ns-gated ICCD camera Intraspec V (Andor Technology). A spectral fragment, selected by this spectrograph, is restricted to about 170 nm by the size of the ICCD photocathode (18 mm) and dispersion of the spectrograph. The available spectral range, determined by the ICCD photocathode, was 200–850 nm. It was possible to cover this range with four partly overlapped spectra. The absence of chromatic aberrations for a mirror objective is very important for a careful measurement of the absolute emission intensity in such a broad spectral range. Glass filters were used to avoid any overlapping of different orders of diffraction in the spectrograph. The minimal exposure time of the ICCD camera was 2.2 ns. The discharge triggering and ICCD gate pulses were synchronized by a computer controlled delay generator DG-535 (Stanford Research Systems Inc.) with a total jitter of about  $\pm 1$  ns.

The VUV–UV emission spectra and kinetics in the 110–300 nm spectral range were measured by a 0.5 m vacuum monochromator M12 (Vemo) with a 1200 lines  $\text{mm}^{-1}$  concave grating (with a spectral resolution of 0.05 nm) and solar blind photomultiplier R1080 (Hamamatsu). The rise time of the photomultiplier anode current pulse on the load of 50  $\Omega$  was 2.5 ns. For a better time resolution, the fast UV photomultiplier R3377 (Hamamatsu) with a synthetic silica window and a rise time of 0.7 ns was used for the kinetics and spectra measurements in the range of 160–410 nm. The emission kinetics were recorded by a digital oscilloscope TDS 3054B and stored in a computer for further data processing. To correct the spectral sensitivity of the registration system in the UV–VIS spectral range, the calibrations using DDS-30 deuterium lamp (180–400 nm) and tungsten ribbon filament standard SIRSH 8.5-200-1 lamp (280–800 nm) were carried out.

It is well known that the VUV emission from  $\text{Ar}_2^*$  excimer molecules is very sensitive to gaseous impurities; therefore special attention has been paid to the purity of the gas system. The discharge chamber (with a volume of  $\sim 5$  l), made of aluminium, and relevant gas handling system were evacuated by a turbomolecular oil-free pumping system to  $10^{-4}$  mbar. Argon gas with a purity of 6.0 was used in the experiments. Nevertheless, the continuous outgassing of materials inside the discharge chamber led to an accumulation of gaseous impurities in the gas after the pure argon refilling. To avoid these contaminants, the gas was continuously recirculated through the heated getter purifier Omni III 200 (NuPure) during the experiments. The gas circulation was organized by the diaphragm compressor N143ST.9E (KNF). According to the technical data of the purifier, at room temperature the getter removes  $\text{H}_2\text{O}$ ,  $\text{O}_2$ ,  $\text{CO}$ ,  $\text{CO}_2$  contaminants down to the ppb level. The getter heated to about 300  $^\circ\text{C}$ , alongside with the cold regime, removes  $\text{N}_2$  and  $\text{CH}_4$  impurities.

### 3.3. Optical schemes for imaging diagnostics of the discharge

The quality of the discharge and its spatial-time development were monitored by the ICCD camera Istar-740 (Andor Technology) with photocathode sensitivity from 110 to 850 nm. The front and side-view images of the discharge were built by the achromatic glass objective Jupiter-37A (it gives the resolution of 45 lines  $\text{mm}^{-1}$ ) with different glass filters. However, in front-view geometry it is difficult to separate emission from different zones along the discharge and only major structure (volume discharge and bright emission zone with cathode spots) could be detected (see Fig. 10). For a better spatial resolution a side-view image of the discharge was built by 45° aluminium mirror and high-quality objective (see Fig. 7). In this scheme only a small longitudinal fraction (about 5 mm) of the whole interelectrode plasma is accessible; however the spatial resolution is rather good and estimated as about 50  $\mu\text{m}$ . This scheme is possible to use in UV-VIS range, but not for VUV light, because of the absence of good VUV objectives.

For VUV imaging, a pinhole optical scheme was used as shown in Fig. 8. The observation axis is slightly tilted from the long axis of the discharge and ns-gated snap-shot of the whole interelectrode plasma is available for detection. VUV  $\text{Ar}_2^*$  emission band at 127 nm is selected by FN 125-N filter (Acton Research Corp.). This filter has a maximum transmission of 21 % at 125 nm and spectral width (FWHM) of 19 nm, with visible light depression of  $10^4$ . The emission of visible continuum and  $\text{Ar}^{**}$  red lines are separated by glass filters with transmission bands of 340–600 nm (SZS-21 filter) and 580–850 nm (OS-14 filter) respectively. Pinhole diaphragm is one of few types of objectives suitable for image building in the VUV spectral range. It allows one to get acceptable resolution along the object (large depth of sharpness) both in VIS and VUV light. According to [57], the optimal resolution could be achieved when the image of a point source, calculated by geometrical optics, is equal to the spot size obtained by Fraunhofer diffraction on a small aperture. This

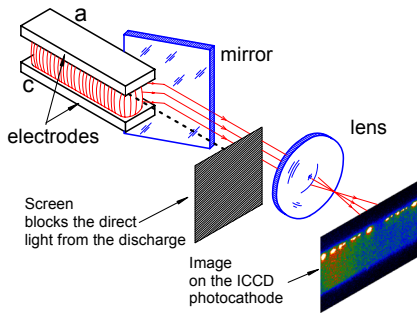


**Figure 7.** Optical scheme for side-view imaging of the discharge.

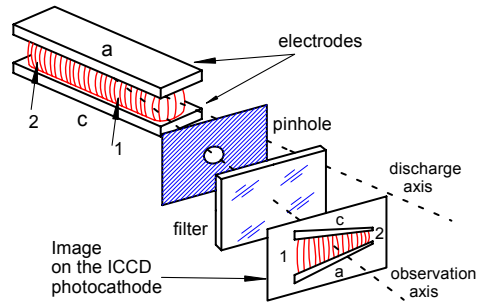


**Figure 8.** Optical scheme in pinhole imaging experiments.

resolution is defined by a criterion  $s^2 \approx 0.61 \lambda d$ , where  $s$  is a pinhole diameter,  $\lambda$  – wavelength,  $d$  – distance between a pinhole and ICCD photocathode. The estimation gives the optimal size of a pinhole in our geometry of about 0.25 mm for  $\lambda = 700$  nm and 0.1 mm for  $\lambda = 127$  nm. However, because of the weakness of spontaneous emission light, the pinhole with a larger diameter (0.37 mm) was used. This allowed to increase detected signal and to neglect diffraction phenomena. The resolution, which is approximately equal to the pinhole size, became worse, but remained quite sufficient to observe the general spatial structure of the discharge.

### 3.4. Scheme for the dye laser absorption probing of the discharge

In addition to above-described spontaneous emission diagnostics methods, the experiments where plasma has been investigated as an absorption medium were carried out. Figure 9 shows experimental setup for the dye laser absorption probing.

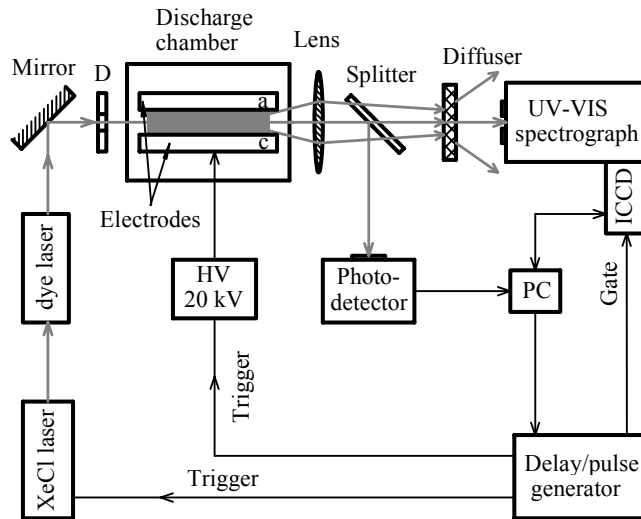


**Figure 9.** Schematic of the experimental apparatus for the absorption probing of the discharge.

The dye laser beam with diameter of about 1 mm, pulse duration of 4 ns and the line width of 0.012 nm (FWHM) was propagated through the long axis of the discharge. Dye laser (VL-10, Vemo) was pumped by the excimer XeCl laser (ELI-75, Semento) with the pulse energy of 50 mJ. Before entering the discharge, the dye laser beam was attenuated by neutral filters in order to avoid the saturation of the optical transitions and distortion in the populations of investigated excited species. The following dyes were applied: Coumarin-120 (423–468 nm), Coumarin-30 (485–530 nm) and Nile blue-A (685–747 nm). Spatial diffuser in front of the spectrograph was used for homogenization of the illumination of the entrance slit and to eliminate influence of the probing beam deflection [Paper VI]. The probing discharge, XeCl pumping laser and ICCD camera gate pulse were synchronized by DG-535 delay generator with a total jitter of about  $\pm 1$  ns.

If the probing dye laser is tuned to the peak of specific absorption line, time behaviours of the densities of excited species is possible to measure by ICCD camera (Intraspec V) through the Shamrock 303i spectrograph by varying the delay between the discharge and the probing laser pulse. The absorption spectrum at the fixed point of time was measured by a photodiode by scanning the dye laser wavelength.

## 4. SPATIAL STRUCTURE AND SURVEY VUV-VIS SPECTRA OF THE DISCHARGE

### 4.1. Images of the discharge

In experiments the charging voltage and parameters of the excitation circuit ( $C_0$ ,  $C_p$ ,  $L_2$ ) were optimized in order to get a homogeneous discharge, which gives a maximal output of the VUV emission. As an example, Fig. 10(a) and 11 shows the front and side-view images of the discharge, excited by a high-current circuit with  $\rho = 0.56 \Omega$  (Ni electrodes) at 4 bar of Ar. These images were measured using the glass filter SZS-23 with a bandwidth of 400–680 nm. An exposure time of 4 ns was fixed at 16 ns after the breakdown (the time point at the end of the first and most intensive excitation pulse). For the front-view image in Fig. 10(a), the spatial resolution is poor because of the small depth of imaging sharpness along the electrodes; hence, only the major structure can be seen: the positive column and the bright emission zone with a manifold of cathode spots. Under non-optimal conditions (for example, low charging voltage, weak or inhomogeneous preionization) instead of the homogeneous volume discharge, narrow bright arc channels were observed independent of the electrode material (W or Ni). The example of a bright single spark is shown in Fig. 10(b). The intensity of spark in visible light is several orders of magnitude higher than for the homogeneous discharge. As was revealed experimentally, spark discharge produces very weak VUV emission from  $\text{Ar}_2^*$  excimers therefore such kind of discharge is extremely undesirable.

To get a better spatial resolution, a side-view imaging scheme (see Fig. 7) were used. Figure 11 shows the 4.6 mm fragment of the discharge with the spatial resolution of about  $50 \mu\text{m}$ . The volume discharge plasma in the positive column was very uniform in the build-up phase of the excitation pulse; however, the discharge lost its perfect uniformity already during the second half of this pulse and seeds of micro-arcs (filaments) appeared in the positive column at the secondary discharge pulses. These filaments started from the hot

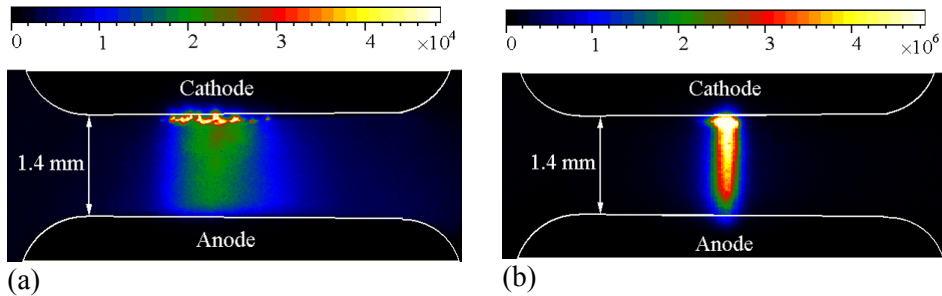


**Figure 10.** Front-view images of the homogeneous (a) and spark (b) discharges. Ar pressure – 4 bar;  $\rho = 0.56 \Omega$ ; Ni electrodes; delay – 16 ns from the beginning of the discharge; exposure time – 4 ns; filter bandwidth – 400–680 nm.

cathode spots, which exploded several nanoseconds after the maximum of the discharge current pulse. The local breakdown of the cathode layer in the spots is caused by a field-enhanced thermionic emission of electrons from microprotrusions, rapidly switched to the explosive emission [40]. The ignition of spots is usually accompanied by the evaporation of the cathode material, which is detected by the appearance of the corresponding metal atomic lines. For example, for the nickel cathode, the strong  $\text{Ni}^*$  atomic lines in the spectral range of 215–235 nm were emitted from the exploded cathode spots. The positions of the spots change stochastically from shot to shot. The density of cathode spots for the nickel electrode was estimated as about  $10 \text{ spots mm}^{-1}$ , so the discharge with  $\sim 6 \text{ kA}$  current had about 2000 spots and the average current density was several amperes per spot. A similar behaviour was observed in the discharges applied for the pumping of rare-gas-halide exciplex lasers [58, 59].

The stable homogeneous discharge was possible to ignite with nickel electrodes at the gas pressure up to 6 bar. In contrast to nickel, the use of tungsten, as a more high-melting material for the cathode, ensured a more uniform volume discharge and allowed increasing the pressure of up to 10 bar, that is illustrated in Fig. 12. Here, the image detection is made by the optical scheme similar to that shown in Fig. 8, but instead of a pinhole the objective Jupiter-37A was used. The depth of the imaging sharpness in this scheme is high enough to build the image of the whole length of short electrodes (25 mm). Only a few cathode spots with low emission intensity were observed in the discharge with tungsten electrodes. According to suggestion in Paper II, a small duration of the excitation pulse is not enough for the breakdown of the cathode layer in the local microprotrusions on the tungsten surface. As a result, only very weak  $\text{W}^*$  atomic lines are detected in the cathode zone.

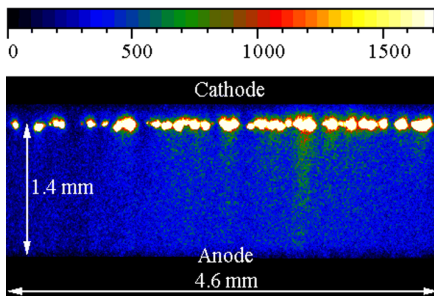


**Figure 11.** Side-view image of the discharge. Ar pressure – 4 bar;  $\rho = 0.56 \Omega$ ; long nickel electrodes; delay – 16 ns from the beginning of the discharge; exposure time – 4 ns; filter bandwidth – 400–680 nm.

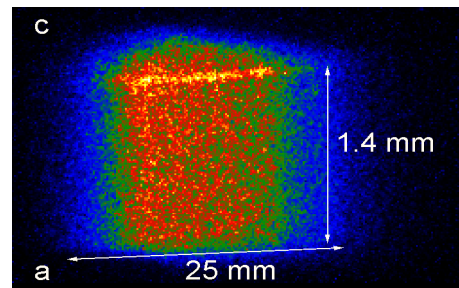


**Figure 12.** Image of a high-current argon discharge at 10 bar. Short (25-mm) tungsten electrodes were used; delay – 4 ns from the beginning of the discharge; exposure time – 2 ns; filter bandwidth – 400–680 nm.

Temporal behaviours of the discharges are available as video-files in <http://hdl.handle.net/10062/15133>

## 4.2. Longitudinal fragmentation of the discharge

Figure 13 shows time-resolved images of plasma emission, detected by a pinhole scheme (see Fig. 8) with different filters. The emission in all spectral ranges is homogeneous and fills the whole space between the electrodes in the beginning (breakdown) phase of the discharge until the appearance of cathode spots. The experimental data indicate, that  $\text{Ar}^{**}$  atoms and  $\text{Ar}_2^*$  excimers are created exclusively in the positive column of the discharge, which is a positive factor for getting the amplification on excimer molecules in the discharge plasma. However, it was revealed, that the discharge has a tendency of longitudinal fragmentation into separate zones at the elevated gas pressure (Papers I, V). The fragmentation is connected with the cathode spots and observed during the secondary discharge excitation pulses. For better visualization the emission kinetics from two spatially separated specific zones 1 and 2 is built in Fig. 14.

The oscillations of UV-VIS continuum and  $\text{Ar}^{**}$  red lines emission has an opposite behaviour in comparison with the VUV emission. Oscillations in zone 1(2) are connected with secondary half-waves of well-defined polarity: “cathode-top” (“cathode-bottom”) correspondently. The asymmetry between two electrodes appears after the first and most powerful excitation pulse. At the end of this pulse manifold of evenly distributed hot spots explode on the cathode surface (upper electrode). These spots serve as relatively long-lived electron emission centers for several successive “cathode-top” half-waves. Really, according to the experimental data in [60] the temperature of the local spot on the nickel surface, heated by ns-pulsed laser, decay with the characteristic time of about 50 ns. The speed of heat dissipation to the cold bulk metal depends on the thermal conductivity of the metal. Moreover, in our case of exploded hot spots the dense long-lived metal plasma above the hot electrode with very high electron density serves as an excellent plasma cathode with a high electron emissivity. This plasma provides very high local discharge current density along with a low voltage of the cathode fall and has been used widely in “superdense glow” discharge in pseudosparks (see for example [61, 62]).

The surface of lower electrode remains cold and after the first change of electrode polarity, when it becomes a cathode, the same process of hot spots ignition takes place. However, in this case the current is much lower and the number (density) of exploded spots is less than for the upper electrode.

It should be noted that the spatially averaged discharge current during secondary oscillations is mostly the same for all zones along the electrodes. However, local current density is much higher in those regions, where bright cathode spots are ignited compared with zones without cathode spots. In these “over-pumped” zones of the partly constricted discharge the high local density of electrons effectively destroy  $\text{Ar}_2^{**}$  excimer molecules and we see minima of VUV emission during the maxima of the discharge current (voltage) – see Chapter 6.3 of this work.

Images in Fig. 13 indicate that cathode spots in the lower electrode are mostly ignited from those zones where the first powerful breakdown pulse was minimal. This behaviour is not totally understood and is possibly caused by desorption of argon and trace gas impurities ( $\text{H}_2\text{O}$ ,  $\text{O}_2$ ,  $\text{CO}$ , hydrocarbons...) from the electrode surface, induced by electrons or VUV photons. It is well

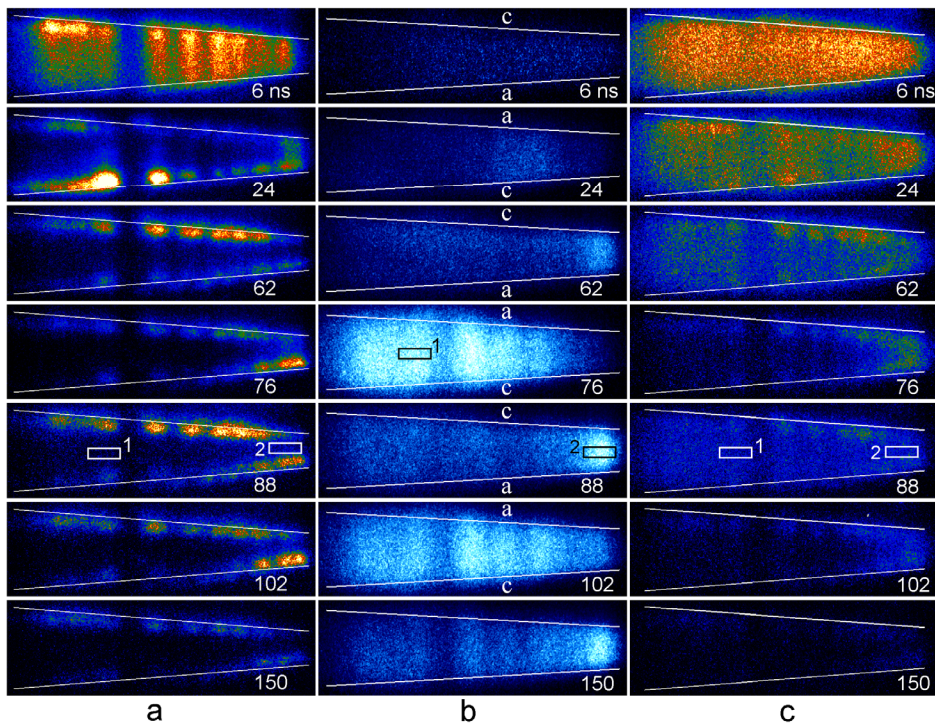


**Figure 13.** Pinhole images of UV-VIS continuum (a); VUV  $\text{Ar}_2^*$  (b);  $\text{Ar}^{**}$  red lines (c) emission in 4 bar Ar discharge at different time moments ( $t = 0$  ns is the beginning of the breakdown, exposure time – 4 ns). The high-current circuit with  $\rho = 0.56 \Omega$  and long nickel electrodes are used. The vertical size of the images corresponds to the gap size (1.4 mm) and the horizontal size – to the whole length of the discharge (200 mm).

Temporal behaviour of the discharge image in VUV light is available as video-file in <http://hdl.handle.net/10062/15133>

known that coefficient of secondary electron emission is very sensitive to the purity and condition of the real surface of the cold cathode [63]. It is significantly higher for contaminated surface than for a clean one, but in any case it is lower than for heated zones of the upper electrode in Fig. 13. Experiment shows that the effect of discharge fragmentation becomes more pronounced in the contaminated argon gas (dis-charge without gas cleaning system). The fragmentation is very undesirable for possible application of the discharge as an active medium for the VUV Ar<sub>2</sub> laser.

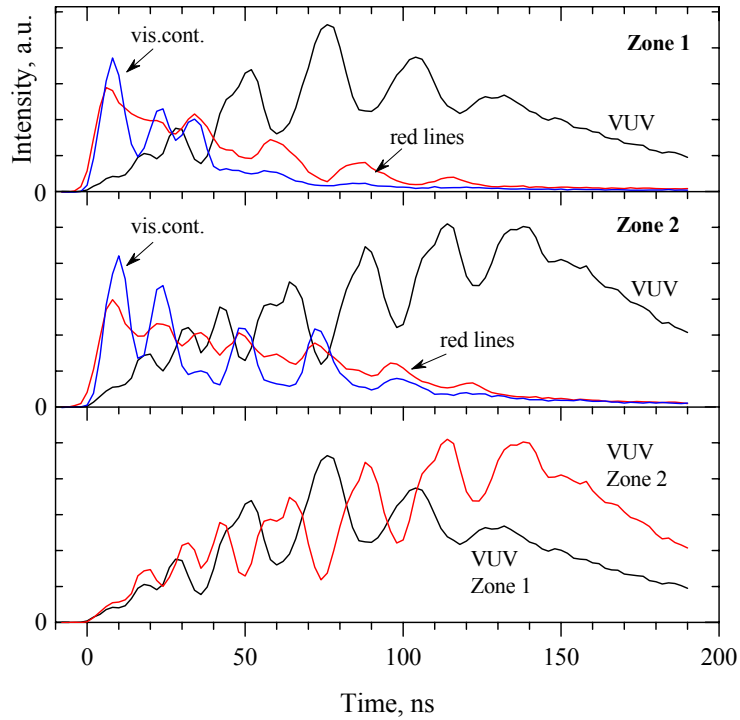


**Figure 14.** Kinetics of VUV Ar<sub>2</sub>\* emission, UV-VIS continuum and Ar\*\* red lines in specific local zones 1 and 2 from Fig. 13.

### 4.3. Survey spectra of the discharge

Imaging spectrograph with ICCD camera permits one to measure time-dependent spatial-resolved spectra emitted from different zones of the discharge plasma. For this experiment the scheme shown in Fig. 7 was modified: instead of the ICCD photocathode the entrance slit of the spectrograph with the ICCD camera on its output was placed. As an example, Fig. 15(b) presents a fragment of the spatial-resolved spectrum of the same discharge as shown in Fig. 11. According to Fig.15 (b) the red  $\text{Ar}^{**}$  lines have a very uniform spatial distribution across the positive column of the discharge. However, UV–VIS continuum is emitted very uniformly from the positive column only at the breakdown stage of the discharge, but at the high-current stage it was concentrated mainly in the near cathode zone [Paper V]. The electrons, accelerated in the high electric field of the cathode layer, are retarded in this local zone and produce a strong ionization resulting in a negative glow effect [64–67]. The negative glow zone is characterized by a high density of electrons. In this zone, a strong Stark broadening of several weak  $\text{Ar}^{**}$  ( $6p, 6p' \rightarrow 4s$ ) lines at 346–357 nm is observed. In the positive column these lines remained narrow during the emission kinetics. As there are no data about the Stark broadening constants [68] for these lines, it was difficult to estimate the density of electrons in the negative glow zone.

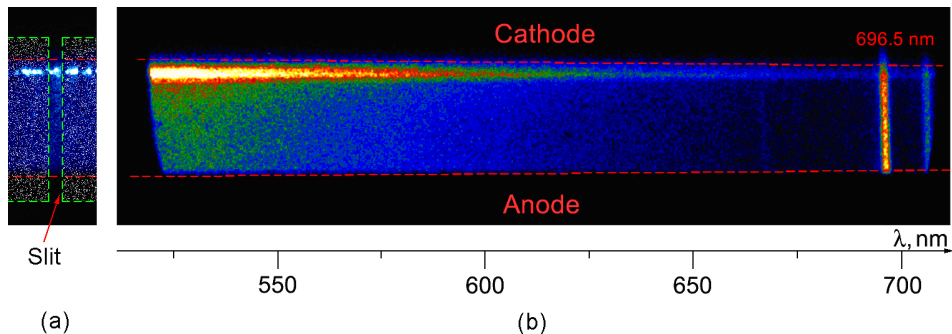


**Figure 15** Side-view image of the discharge from Fig. 11 which is projected into the entrance slit of the spectrograph (a) and fragment of its spatially-resolved spectrum (b). The intensity of emission is shown with pseudo-colours. The exposure time – 4 ns, delay – 16 ns from the beginning of the discharge.

Temporal behaviour of the spectrum is available as video-file in <http://hdl.handle.net/10062/15133>

The emission of the discharge plasma in argon has several spectral components with specific time behaviours, which varied significantly with the gas pressure and excitation regimes. As a general overview, Fig. 16 shows the spectra of the homogeneous volume discharge at 4 bar of Ar with tungsten electrodes and high-current excitation circuit, not corrected to the spectral sensitivity of the registration systems. These time-integrated spectra (the exposure time is 10 ns, with zero delay time from the beginning of the discharge) were measured by several detectors and spectrometers. The VUV spectral range, measured by a solar blind photomultiplier and VUV monochromator, is characterized by the well-known intense second continuum band centred at 127 nm (emission from vibrationally relaxed levels of singlet  $\text{Ar}_2^*(^1\Sigma_u)_{(v=0)}$  excimers). At a high gas pressure, the vibrational relaxation is fast; therefore, the first continuum (emission from vibrationally hot levels of singlet  $\text{Ar}_2^*(^1\Sigma_u)_{(v)}$  excimers) is very weak. The spectral range from 160 to 410 nm, measured by the UV photomultiplier and VUV monochromator, is characterized by a broad UV–VIS continuum. The survey spectrum of this continuum, measured by the ICCD camera and UV–VIS spectrograph, is shown in Fig. 16(b). In addition to the continuum, several lines are observed: weak blue lines (395–434 nm), which belong to  $\text{Ar}^{**}(5p, 5p' \rightarrow 4s, 4s')$  transitions and strong red lines (696.5–850 nm) of  $\text{Ar}^{**}(4p', 4p \rightarrow 4s, 4s')$  transitions. No emission from  $\text{Ar}^{+**}$  lines was observed in the discharge at pressure of 1–10 bar. The gas recirculation through the heated getter purifier eliminated almost all impurity emission lines. The following spectral components practically totally disappeared in the spectrum during the gas circulation: 130.5 nm ( $\text{O}^*, 3s\ ^3S^0 \rightarrow 2p^4\ ^3P_2$ ); 174.5 nm ( $\text{N}^*, 3s\ ^2P \rightarrow 2p^3\ ^2P^0$ ); 307.8 nm ( $\text{OH}^* \text{ A } ^2\Sigma^+_{(v=0)} \rightarrow \text{X } ^2\Pi_{(v=0)}$  band); 337.1 nm ( $\text{N}_2^* \text{ C } ^3\Pi_{u(v=0)} \rightarrow \text{B } ^3\Pi_{g(v=0)}$  band). The intensities of the carbon lines at 165.7 nm ( $3s\ ^3P^0 \rightarrow 2p^2\ ^3P$ ) and 193.1 nm ( $3s\ ^1P^0 \rightarrow 2p^2\ ^1D$ ) were also significantly reduced.

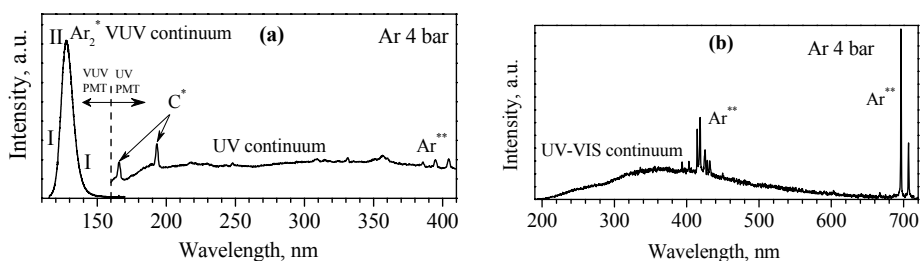


**Figure 16.** Emission spectra of the homogeneous volume discharge at 4 bar of Ar (high-current excitation circuit, tungsten electrodes), measured by (a) VUV monochromator, solar blind (VUV) and UV photomultipliers; (b) ICCD camera and UV–VIS spectrograph; zero delay time, exposure time – 10 ns.

At non-optimal discharge excitation conditions, where narrow bright arc channels are created, a very weak  $\text{Ar}_2^*$  VUV emission and red  $\text{Ar}^{**}$  lines are observed, whereas the emission of UV–VIS continuum exceedingly increased. Different spectral components observed in emission of argon plasma can be classified depending on the discharge conditions (homogeneous discharge or spark) and gas pressure. This classification is given in Table 1.

**Table 1:** Characterisation of different spectral components in emission of argon plasma, depending on the discharge conditions and gas pressure

<b>spectral component</b>	<b>behaviour with the increase of the pressure</b>	<b>spark</b>	<b>homogeneous discharge</b>	<b>zone of the discharge</b>
II continuum 127 nm	acceleration in kinetics, growth of intensity	weak or absent	intense	positive column
III continuum 190 nm	acceleration in kinetics, decrease of intensity	absent	weak	negative glow zone
UV-VIS continuum 200–800 nm	growth of intensity	very intense	weak	more intense in the negative glow zone
$\text{Ar}^{**}$ lines 395–434 nm and 696.5–850 nm	growth of intensity	weak or absent	intense	positive column
$\text{Ar}^{+*}$ lines 280–400 nm	decrease of intensity	absent	weak	negative glow zone

The third continuum of argon, centred at 190 nm (see Paper III and Chapter 7 of the thesis) is also included to the table. This band together with a number of  $\text{Ar}^{+*}$  lines in the UV range were detected under the lower-current discharge excitation at the reduced gas pressure. The imaging experiments with ICCD camera show that the third continuum and  $\text{Ar}^{+*}$  lines emitted exclusively from the negative glow zone, not from the positive column of the discharge.

## 5. THE NATURE AND MODELING OF UV-VIS CONTINUUM

### 5.1. Spectra of UV-VIS continuum in the pulsed arc and homogeneous discharges

The attention paid to the UV-VIS continuum emission in rare gases is historically caused by a wide use of arc plasma in analytical applications. The continuum radiation in plasma originates from the interaction of free electrons with ions and neutral atoms. In application to argon, the main processes, responsible for the continuum emission, are:

1. free-bound transition by the capture of free electron with its subsequent radiative transition into the bound level (photorecombination  $\text{Ar}^+ + e \rightarrow \text{Ar}^* + h\nu$ ) [69–71];
2. free-free transition by electron-ion interaction with the deceleration of free electron in the electric field of ion (bremsstrahlung on ions  $\text{Ar}^+ + e \rightarrow \text{Ar}^+ + e + h\nu$ ) [69–71];
3. free-free transition where free electron losses part of its kinetic energy by the interaction with an atom (bremsstrahlung on atoms:  $\text{Ar} + e \rightarrow \text{Ar} + e + h\nu$ ) [71–73].

It should be noted that only atomic  $\text{Ar}^+$  ions are taken into account in the listed publications for the modeling of the UV-VIS continuum, which is well justified for the dense and equilibrium plasma of the arc discharge. In this case, according to the estimation in [71], the photorecombination emission is about ten times higher than the bremsstrahlung on ions; hence the latter mechanism was not taken into account in the modeling in this thesis.

In the case of the homogeneous volume discharge in a cold argon gas, the positive charge carriers are totally different from the arc condition, because atomic  $\text{Ar}^+$  ions rapidly convert to molecular  $\text{Ar}_2^+$  ions. Hence the assignment of the UV-VIS continuum in a high-pressure discharge is not an easy task.

As was revealed in the experiment (Paper II), the spectral shape of the UV-VIS continuum is dependent on the homogeneity of the discharge. By changing the excitation circuit parameters, three discharge regimes were obtained: homogeneous volume discharge, totally constricted arc discharge and intermediate regime where the uniform volume discharge phase coexists with micro-arcs (filaments) during and after the excitation pulse. Figure 17 shows the experimental spectra, measured for a high-quality volume discharge (a) and pulsed arc discharge (b) at 4 bar of argon. The intensity scale is proportional to  $\text{W nm}^{-1}$  (correction of the spectral sensitivity of the registration system was carried out). The intensity of the arc spectrum is much higher than that of the homogeneous one. However, to emphasize the spectral variation of the emissivity, both continuous spectra were normalized at 500 nm. In the spectral

range of 280–710 nm, the spectra were registered by UV-VIS spectrograph with ICCD camera and in the range of 190–410 nm – by VUV monochromator with UV photomultiplier. As follows from Fig. 17, the UV side of the normalized spectrum (200–400 nm) is significantly higher for the uniform volume discharge than for the constricted one.

For tungsten electrodes and low-impedance circuit, the high-current discharge remained homogeneous during the first and even secondary discharge excitation pulses. As a consequence, the shape of the UV-VIS continuum spectrum did not change throughout the kinetics and remained close to the spectrum (a). For nickel electrodes and especially for the peaking circuit with high  $\rho$ , the constriction was developed already at the second half of the main excitation pulse. The beginning of the constriction was clearly detected by the change of the spectral shape of the UV-VIS continuum in the time-resolved spectra. For the nickel electrodes, the continuum spectrum was always close to the constricted shape (b) during and after the secondary excitation pulses.

In Fig. 18 the (b)-shape continuum spectrum from Fig. 17 is compared with the experimental spectrum from [71]. The latter one was obtained for the direct current arc discharge in Ar at 4 bar and  $T_e$  of about 1.2 eV in the conditions of the local thermal equilibrium. Both continuum spectra are rather close to each other in spite of the very different conditions of the discharges.

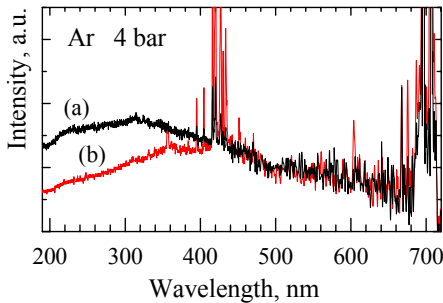


**Figure 17.** The spectra of UV-VIS continua of the discharge at 4 bar of argon at different regimes of the excitation: (a) homogeneous volume discharge; (b) pulsed arc discharge.

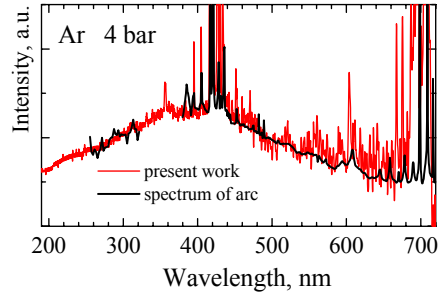


**Figure 18.** The spectra of UV-VIS continua of the pulsed arc discharge (spectrum (b) in Fig. 17) and direct current arc discharge (from [71]) at 4 bar of Ar.

As was suggested in Paper II, the change in the spectral shape of UV-VIS continuum is connected with the difference of the positive charge carriers in the arc and homogeneous discharge plasmas. According to [78] for inductively coupled argon plasma at atmospheric pressure, the fraction of molecular  $\text{Ar}_2^+$  ions with respect to  $\text{Ar}^+$  ions depends strongly on the gas and electron densities and their temperatures. The main reactions that have an influence on the formation and destruction of  $\text{Ar}_2^+$  molecular ions are listed in Fig. 19.

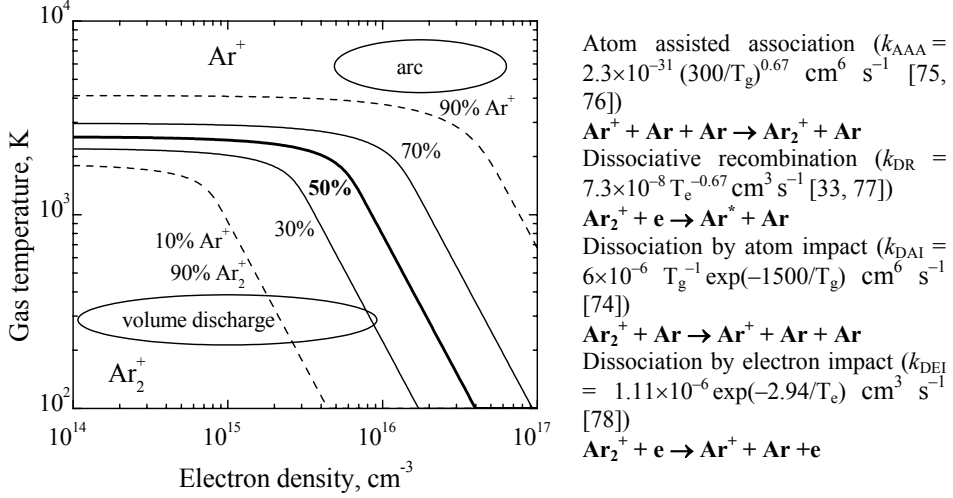


**Figure 19.** Calculated diagram for percentage of  $\text{Ar}_2^+$  and  $\text{Ar}^+$  ions in a pulsed discharge, depending on the electron density  $n_e$  and gas temperature  $T_g$ . The argon density and electron temperature are fixed at  $n_a = 10^{20} \text{ cm}^{-3}$  and  $T_e = 0.9 \text{ eV}$  respectively.

In plasma at (quasi-) stationary conditions, the balance between the formation and destruction of molecular  $\text{Ar}_2^+$  and atomic  $\text{Ar}^+$  ions can be written as

$$k_{AAA}n_a^2n_{\text{Ar}^+} = k_{DR}n_en_{\text{Ar}_2^+} + k_{DAI}n_an_{\text{Ar}_2^+} + k_{DEI}n_en_{\text{Ar}_2^+} \quad (6)$$

which together with the charge neutrality

$$n_{\text{Ar}^+} + n_{\text{Ar}_2^+} = n_e \quad (7)$$

leads to

$$n_{\text{Ar}_2^+} = \frac{k_{AAA}n_a^2n_e}{k_{AAA}n_a^2 + k_{DR}n_e + k_{DAI}n_a + k_{DEI}n_e} \quad (8)$$

where  $n_a$ ,  $n_{\text{Ar}^+}$ ,  $n_{\text{Ar}_2^+}$  and  $n_e$  are the densities of Ar atoms,  $\text{Ar}^+$ ,  $\text{Ar}_2^+$  and electrons, respectively. The calculation of the percentage of  $\text{Ar}_2^+$  and  $\text{Ar}^+$  ions depending on the electron density and gas temperature was carried out (see Fig. 19) at fixed electron temperature ( $T_e = 0.9 \text{ eV}$ ) and gas density ( $10^{20} \text{ cm}^{-3}$ ), which corresponds to the Ar pressure of 4 bar at the gas temperature  $T_g = 300 \text{ K}$ . These assumptions are reasonable, because after the powerful nanosecond pulsed excitation the gas is instantly heated, and  $n_a$ ,  $T_g$ ,  $T_e$  don't

change considerably in a time scale of about 100 ns. The chosen value for  $T_e$  is close to that, calculated in [33], where the electron temperature in the recombination stage is stabilized at about 0.8 eV after the powerful e-beam excitation pulse and remained changeless for several hundreds of nanoseconds.

In contrast to the arc channels, the homogeneous pulsed discharge leads to a very small gas heating. In the paper [79], where similar excitation conditions were used for helium discharge at 5 bar, the so-called “internal nitrogen molecular thermometer” was used for gas temperature monitoring. The trace admixture of nitrogen ( $\sim 0.1$  mbar) to the gas has a small effect on the plasma-chemical kinetics in the discharge. Rotational-translational relaxation is very fast at a high pressure, so the temperature calculated from the measured rotational structure of  $N_2^* C^3\Pi_u(v=0) \rightarrow B^3\Pi_g(v=0)$ , 337.1 nm emission band is close to the gas temperature. According to the experimental data [79], the gas is heated from 325 to about 380 K during the discharge excitation pulse. The accuracy of this thermometer is rather high (about  $\pm 10$  K). Thus, according to the diagram in Fig. 19, the main positive charge carriers in the homogeneous discharge plasma are molecular  $Ar_2^+$  ions.

Next, we try to consider the spectrum, which can be the result of photorecombination of  $Ar^+$  ions. According to principles developed in [38], after the electron capture in a field of  $Ar^+$  ion and its transition into the discrete  $Ar^*$  level  $n$  (a schematic energy level diagram for argon is shown in Fig. 2), the photon with the energy  $h\nu = (E_1 - E_n) + \varepsilon$  is emitted, where  $E_1 - E_n$  is the difference between the argon ionization energy and  $Ar^*$  discrete level  $n$ , and  $\varepsilon$  is the energy of electron. For the electrons in the energy interval  $\varepsilon \div \varepsilon + d\varepsilon$ , the total emitted photorecombination energy  $J_{\nu n}$  with the formation of excited  $Ar^*$  atom on the level  $n$ , per unit time and per unit volume, can be expressed as

$$J_{\nu n} d\nu = h\nu n_{Ar^+} n_e \sigma_n^{rec} \sqrt{\frac{2\varepsilon}{m_e}} f(\varepsilon) d\varepsilon, \quad (9)$$

where  $\sigma_n^{rec}$  is the cross section of an electron capture to the  $Ar^*$  level  $n$ ,  $f(\varepsilon)$  is the electron energy distribution function, that here was taken as Maxwellian. The total spectrum of the photorecombination emission is the sum of terms  $J_{\nu n}$ . As the capture of electron occurs into the discrete levels, the emission spectrum has specific sharp edges of series. The cross section  $\sigma_n^{rec}$  can be determined from its relationship with photoionization cross section  $\sigma_n^I$ , given in [80]:

$$\sigma_n^{rec} = \sigma_n^I \frac{g_n}{u_i c} \frac{h\nu}{\sqrt{2m_e \varepsilon}}, \quad (10)$$

where  $g_n$  is the statistical weight for the atomic level  $n$  and  $u_i$  – partition function for  $Ar^+$  ion. The photoionization cross sections as a function of

wavelength for 4s, 4p and 3d  $\text{Ar}^*$  levels were taken from [81]. Our model takes into account totally 26  $\text{Ar}^*$  sublevels. The data about sublevels and their statistical weights were used from [44]. The main input into the photorecombination in the UV-VIS spectral range is caused by the capture of electrons with an energy of up to about 2 eV into 4s (4s'), 4p (4p'), 3d (3d')  $\text{Ar}^*$  levels. The photorecombination to higher  $\text{Ar}^{**}$  levels gives mainly infrared radiation, and these transitions are not taken into account in the model. The photorecombination to 4s, 4s' levels is negligible because of the small photoionization cross section [81]. Figure 20 demonstrates the calculated inputs of photorecombination transitions to 4p, 4p', 3d, 3d'  $\text{Ar}^*$  states for  $T_e = 1.0$  eV and their sum along with the experimental spectrum (a) from Fig. 17 for comparison. This simple model clearly shows the sharp edge of 4p, 4p' series at about 460 nm, which is not observed in UV-VIS continuous spectra measured in this work.

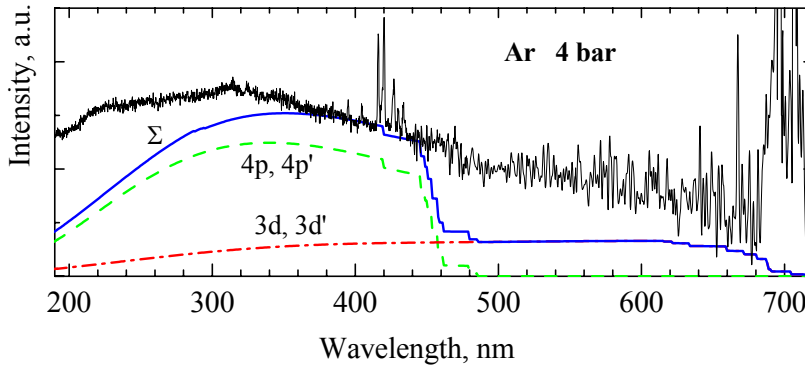


**Figure 20.** The experimental continuous spectrum (shape (a) in Fig. 17) and calculated inputs of photorecombination transitions to 4p, 4p', 3d, 3d'  $\text{Ar}^*$  states for  $T_e = 1.0$  eV and their sum ( $\Sigma$ ). The intensity scale is proportional to  $\text{W nm}^{-1}$ .

More complicated model, suggested in [82], well describes the continuum spectrum of the arc discharge by the photorecombination of  $\text{Ar}^+$  ions. The calculation in [82] takes into account the interaction between the radiating atom and surrounding plasma particles. This interaction (effect of plasma microfields) gives a 'red' shift and spread of the photoionization thresholds. However, it becomes apparent only in dense plasma conditions ( $n_e \sim 10^{17} \text{ cm}^{-3}$ ). At a lower electron density, the model also predicts sharp spectral edges in the photorecombination continuum of  $\text{Ar}^+$  ions.

In the case of homogeneous volume discharge, it is impossible to describe the spectral shape of UV-VIS continuum (spectrum (a) in Fig. 17) by the existing photorecombination [71, 38, 82] or bremsstrahlung [72, 73] models. The same spectral shape is observed even at the early stage of the breakdown,

when the density of electrons is low and the effect of plasma microfields is negligible. Thus sharp spectral edges should be observed in assumption of photorecombination of  $\text{Ar}^+$  ions.

The alternative hypothesis of the origin of UV-VIS continuum in the homogeneous high-pressure volume discharge in the cold gas could be the interaction of  $\text{Ar}_2^+$  ions with electrons. This suggestion seems to be reasonable, because at these conditions the positive charge carriers are mainly  $\text{Ar}_2^+$  molecular ions (see Fig. 19). On the analogy of photorecombination of atomic  $\text{Ar}^+$  ions (right wavy arrow in Fig. 2), the electron could be captured by molecular  $\text{Ar}_2^+$  ion and transferred into  $\text{Ar}_2^*$  energy level with the emission of a photon:  $\text{Ar}_2^+ + e \rightarrow \text{Ar}_2^* + h\nu$  (left wavy arrow in Fig. 2). According to the Frank-Condon principle, such radiative transition can realize mainly as a vertical one without change of the internuclear coordinate. It is difficult to calculate the photorecombination spectrum for  $\text{Ar}_2^+$  molecular ions, as the required data for manifold of  $\text{Ar}_2^*$  states and photoionization cross sections are absent. Each specific  $\text{Ar}^*$  atomic state gives, in principle, a number of  $\text{Ar}_2^*$  molecular bound and repulsive states, arising from  $\text{Ar} + \text{Ar}^*$  combinations of molecular orbitals (see, for example, the estimated potential curves for  $\text{Ar}_2^*$  in [27]). One may speculate that due to a larger number of  $\text{Ar}_2^*$  states in comparison with  $\text{Ar}^*$  states, the photorecombination spectrum of  $\text{Ar}_2^+$  ions should be similar to the spectrum of  $\text{Ar}^+$  ions, but spectrally more smoother. Any description of this mechanism has not been found in the literature. Certainly, this question calls for a special theoretical consideration – this task could be a good challenge for theoreticians.

## 5.2. Kinetics of UV-VIS continuum and $\text{Ar}^{**}$ red lines

The photorecombination nature of the UV-VIS continuum is confirmed by the experimental emission kinetics in the recombination stage. Under high-pressure conditions, the dissociative recombination is the main channel for the loss of electrons. This statement holds true not only for the pulsed homogeneous volume but also for the constricted arc discharge. The rate constant for three-body electron–ion recombination  $\text{Ar}^+ + 2e \rightarrow \text{Ar}^{**} + e$  ( $k_{ee} = 7.2 \times 10^{-27} T_e^{-9/2} \text{ cm}^6 \text{ s}^{-1}$ ) [83, 84] is too low, because  $T_e$  is high in the afterglow stage. According to Fig. 19, the fraction  $\alpha$  of  $\text{Ar}_2^+$  ions is determined mainly by gas temperature  $T_g$  in a recombined plasma with a low degree of ionization:  $n_{\text{Ar}_2^+} = \alpha \cdot n_e$ . Electrons disappear by a recombination law (11) with the effective recombination constant  $k_{DR}\alpha$

$$n_e(t) = \frac{n_{e0}}{1 + n_{e0} k_{DR} \alpha t}, \quad (11)$$

where  $n_{e0}$  is the initial electron density. For homogeneous volume discharge,  $\alpha = 1$  and recombination is fast. For the arc condition  $\alpha \ll 1$  and recombination could be retarded in spite of the fact that the density of electrons is very high. Fig. 21 demonstrates the experimental kinetics of continuous radiation at 550 nm and Ar<sup>\*\*</sup> red line (4p' [1/2]<sub>1</sub> → 4s [3/2] transition, 696.5 nm) during the recombination stage of the discharge at 4 bar of Ar. The kinetics of the electron density  $n_e(t)$  were described by the recombination law (11). The initial time of the kinetics was selected in the afterglow stage, when the secondary discharge oscillations have totally disappeared and the density of electrons is significantly reduced.

If one suggests that the UV-VIS continuum is caused by bremsstrahlung on atoms, then its intensity should be proportional to  $n_e(t)$  (the upper curve in Fig. 21), which is not observed in the experiment. Both experimental kinetics are well described by  $n_e^2(t)$  dependence, which confirms the photo-recombination origin of the continuum. It should be noted that the perfect experimental behaviours, proportional to  $n_e^2(t)$ , indicate that  $k_{DR} \propto$  value remains unchanged during the kinetics. It means that  $T_e$  (influence on  $k_{DR}$ ) and  $T_g$  (influence on  $\alpha$ ) really do not change considerably in the afterglow stage, which confirm the assumptions of suggested model.

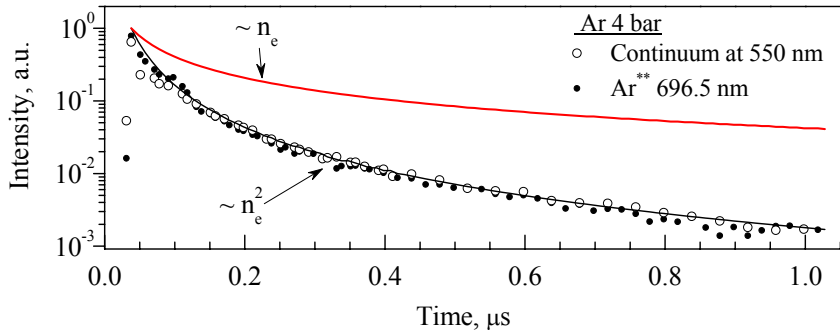


**Figure 21.** Experimental kinetics of continuous emission at 550 nm, Ar<sup>\*\*</sup> red line 696.5 nm (4p' [1/2]<sub>1</sub> → 4s [3/2] transition) during the recombination stage of the discharge at 4 bar of Ar. Kinetics of  $n_e$  were modelled by the recombination law (11). The upper curve shows the calculated emission intensity in the case of its linear dependence with  $n_e$ .

Ar<sup>\*</sup> 4p' levels are known to be selectively populated by dissociative recombination of Ar<sub>2</sub><sup>+</sup> ions [85, 86]. There are three possible ways of decay for these states: spontaneous emission, deactivation by free electrons and deactivation by Ar atoms. The total radiative decay time of Ar<sup>\*</sup> 4p' [1/2]<sub>1</sub> state, considering the optical transitions to all possible lower levels, is 25 ns [43, 44]. The rate constant of the electron-impact-induced excitation transfer between Ar<sup>\*</sup>

levels is  $2 \times 10^{-7} \text{ cm}^3 \text{ s}^{-1}$  [87], which corresponds to 50 ns for electron density of  $10^{14} \text{ cm}^{-3}$  (estimated density of electrons in the recombination tail in Fig. 21). The deactivation rate constant for  $\text{Ar}^* 4p' [1/2]_1$  level by collisions with Ar atoms is equal to  $5.3 \times 10^{-11} \text{ cm}^3 \text{ s}^{-1}$  [43]. This constant corresponds to the characteristic time of about 0.2 ns for 4 bar, which is practically instant compared with the duration of kinetics, shown in Fig. 21. Thus, the emission of the  $\text{Ar}^*$  red lines together with the radiation of UV-VIS continuum reflects completely the loss of electrons by dissociative recombination in the afterglow plasma.

## 6. KINETICS OF KEY SPECIES IN PLASMA

### 6.1. Emission and absorption bands (lines) used for the diagnostics

For the diagnostics of plasma the following spontaneous emission bands and their kinetics were chosen:

1. 115 nm – emission of the first continuum of  $\text{Ar}_2^*$  excimers;
2. 127 nm – emission of the second continuum of  $\text{Ar}_2^*$  excimers;
3. 550 nm – corresponds to the emission of UV-VIS continuum. It was specially verified that the kinetics of UV-VIS continuum was the same in the spectral range of 400–700 nm;
4. 695.6 nm – one of the most intense red  $\text{Ar}^{**}$  lines, emitted from the  $4p' [1/2]_1$  state (this transition is  $2p_2 \rightarrow 1s_5$  in Paschen notation). The temporal behaviours of all  $\text{Ar}^{**}$  red lines are the same.

The kinetics of these bands (lines) were detected according to the scheme in Fig. 6., where the observation axis was slightly tilted from the long axis of the discharge to eliminate the possible reabsorption.

Additionally to spontaneous emission, the diagnostics of plasma was carried out by the dye laser absorption probing, which permits one to determine the absolute densities of excited species. The description of the method and experimental procedures are given in Chapters 2.3 and 3.4. To measure the density of  $4s$  and  $4p$   $\text{Ar}^*$  levels (see the energy levels diagram in Fig. 2), the following absorption lines were considered:  $4s[3/2]^\circ \rightarrow 5p[5/2]$  ( $1s_4 \rightarrow 3p_8$  in Paschen notation), 430.0 nm,  $A_{ki} = 3.94 \times 10^5 \text{ s}^{-1}$  and  $4p[1/2] \rightarrow 6d[1/2]$  ( $2p_{10} \rightarrow 6d_5$  in Paschen notation), 516.2 nm,  $A_{ki} = 1.98 \times 10^6 \text{ s}^{-1}$  respectively (see also Paper VI). There are much less reliable data for  $\text{Ar}_2^*$  molecular transitions than for  $\text{Ar}^*$  atomic one. For monitoring the densities of  $\text{Ar}_2^*$  excimers in the triplet state, the 0–0 molecular absorption band  $4s \ ^3\Sigma_u^+ (v=0) \rightarrow 5p, \ ^3\Sigma_g^+ (v=0)$  at 512.0 nm was used. For this R-type branch the absorption cross-section was determined in [48] at the argon gas pressure of 1 bar:  $\sigma = (3.3 \pm 0.5) \times 10^{-16} \text{ cm}^2$ . The red side of this band has the well-developed rotational structure [88]. At high gas pressure this structure is not resolved and produces a broad red-shaded band. Therefore, the spectral width of the absorption band  $\Delta\lambda_p$  (FWHM) is defined as a double width of the blue side of the R branch. The density of  $\text{Ar}_2^*$  excimers in the  $4s \ ^3\Sigma_u^+$  state was determined from the experimental absorption coefficient  $\kappa_p$  according to formula (4), where  $\Delta\lambda_p$  and  $\Delta\lambda_1$  are the spectral widths (FWHM) of 512.0 nm band for the gas pressure  $p$  and 1 bar respectively.

The measurements were carried out according to the scheme, shown in Fig. 9. High-current excitation circuit (a) in Fig. 5 with long (220 mm) nickel electrodes were used. For a general overview, Fig. 22 shows fragments (503–524 nm) of absorption spectra of the discharge in Ar at 2 bar, measured on 40<sup>th</sup>

and 260<sup>th</sup> ns from the breakdown. After the excitation pulse strong absorption lines from Ar\* atomic 4p and 4s states are detected at t = 40 ns. At the late stage of the discharge (t = 260 ns) absorption from relatively short-lived atomic Ar\* states is strongly reduced whereas the absorption from the long-lived 4s  $^3\Sigma_u^+$  Ar<sub>2</sub>\* triplet excimers to 5p,  $^3\Sigma_g^+$  and 5p,  $^3\Pi_g$  states is still rather strong. The rotational structure of the red-shaded Ar<sub>2</sub>\* molecular bands is not resolved due to pressure broadening, but vibronically excited excimer molecules Ar<sub>2</sub>\* 4s  $^3\Sigma_u^+$  (v=1) are clearly detected. Hot vibronic states are populated significantly only when the Ar<sub>2</sub>\* molecules are far from the thermal equilibrium with the cold gas in the volume discharge – mainly during the creation reaction of excimers:  $\text{Ar}^* + 2\text{Ar} \rightarrow \text{Ar}_2^* + \text{Ar}$ .

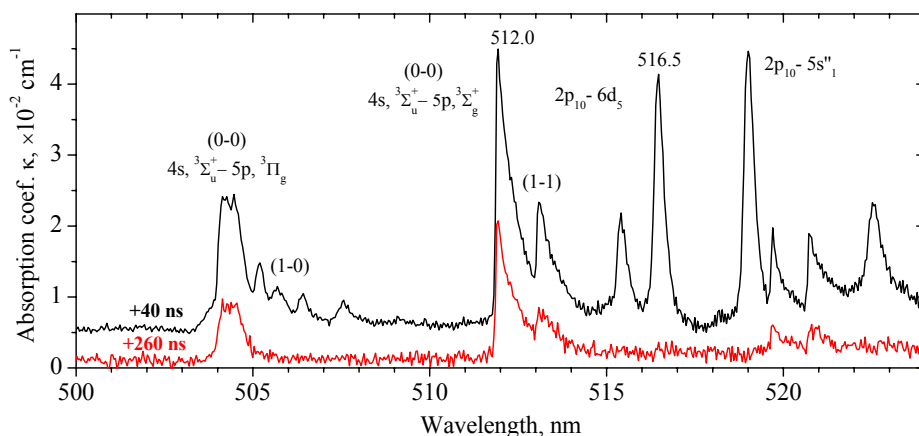


**Figure 22.** Fragments of the absorption spectra of the high-current discharge at Ar pressure of 2 bar, measured at 40 and 260 ns after the breakdown.

Under the high pressure conditions the Doppler broadening is negligible and absorption lines are mainly broadened due to elastic collisions with Ar atoms. This statement is confirmed by Fig. 23, where experimentally measured bandwidths (FWHM) for Ar\* atomic absorption lines (Ar<sub>2</sub>\* molecular band) increase linearly with Ar pressure.

To investigate the temporal behaviour of excited species the dye laser was tuned to the peak of specific absorption line and the delay time between the discharge and the probing laser pulse was varied. Further, the densities of excited species (Ar\* atoms in 1s<sub>4</sub>, 2p<sub>10</sub> states and Ar<sub>2</sub>\* excimer molecules in 4s  $^3\Sigma_u^+$  (v=0) state) were calculated by formulas (1), (3) and (4) according to the experimentally measured absorption kinetics.

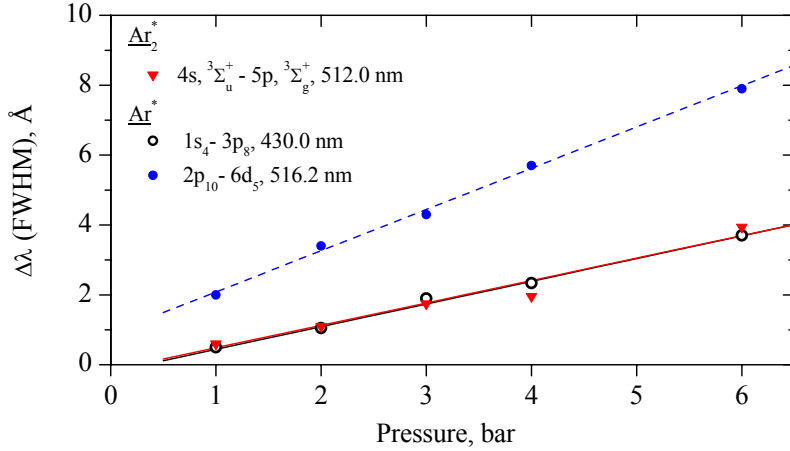


**Figure 23.** Experimentally measured pressure broadening  $\Delta\lambda$  (FWHM) of  $\text{Ar}^*$  atomic and  $\text{Ar}_2^*$  molecular absorption lines.

## 6.2. Kinetic model

For the simulation of the experimental kinetics and estimation of plasma parameters after the pulsed excitation the kinetic model was developed. Key plasma-chemical reactions, which have a strong influence to the kinetics of  $\text{Ar}_2^*$  excimers, were included in the model. The constants of these reactions are summarized in Table 2. The system of differential kinetic equations was solved for several specific plasma species:

$$\partial\rho_i / \partial t = \sum_l F_{il}^+ - \sum_m F_{im}^- \quad (12)$$

where  $\rho_i$  is the density of the  $i^{\text{th}}$  plasma component and  $F_{il}^+$  and  $F_{im}^-$  are the creation and destruction fluxes of the  $\rho_i^{\text{th}}$  component in reactions  $l$  and  $m$ . The following 12 components are included in the model: electrons, ions  $\text{Ar}^+$  and  $\text{Ar}_2^+$ , excited  $\text{Ar}^*$  atoms in 4s ( $s_2$  and  $s_4$  resonant;  $s_3$  and  $s_5$  metastable levels in Paschen notation) and 4p states, high-lying ( $v$ ) and the relaxed ( $v=0$ ) vibrational levels of  $\text{Ar}_2^*$  excimers in the singlet  $^1\Sigma_u^+$  and triplet  $^3\Sigma_u^+$  states.

In a high-current pulsed excitation the peak electron density is very high (about  $10^{16} \text{ cm}^{-3}$ ). In this case the interelectron interaction is extremely fast, therefore Maxwellian electron energy distribution function is assumed. The accurate calculation of the electron temperature  $T_e$  was not carried out, since the modeling of the real electric field in the positive column of highly conductive high-pressure discharge plasma is a rather complicated task. In the developed model, the electron temperature  $T_e$  is a variable parameter. Before the breakdown,  $T_e$  is fixed at 2 eV, which allows one the modeling of the avalanche

electron multiplication due to direct and step-wise excitation (ionization) of argon atoms (reactions R1, R2, R6 and R7). The calculated rate constants of reactions R1 and R2 are approximated by the analytical formulas for the electron temperature range of 0.5–10 eV. The rate constants and their temperature dependences for the ionization of  $\text{Ar}^*$  (R6) and  $\text{Ar}_2^*$  (R7) by fast electrons were taken identical, as was proposed in [33, 51].

**Table 2.** Overview of the main reactions and their rate constants

No	Process	Rate Constant	Reference
R1	$\text{Ar} + e \rightarrow \text{Ar}^* + e$	$6 \times 10^{-9} T_e^{0.75} \exp(-11.5/T_e)$	calculation <sup>a</sup>
R2	$\text{Ar} + e \rightarrow \text{Ar}^+ + e$	$1.7 \times 10^{-8} T_e^{0.5} \exp(-15.8/T_e)$	calculation <sup>a</sup>
R3	$\text{Ar}^+ + 2\text{Ar} \rightarrow \text{Ar}_2^+ + \text{Ar}$	$2.3 \times 10^{-31} (300/T_g)^{0.67} \text{ cm}^6 \text{ s}^{-1}$	[75, 76]
R4	$\text{Ar}_2^+ + e \rightarrow \text{Ar}^* + \text{Ar}$	$7.3 \times 10^{-8} T_e^{-0.67} \text{ cm}^3 \text{ s}^{-1}$	[33, 77]
R5	$\text{Ar}_2^+ + e \rightarrow \text{Ar}^+ + \text{Ar} + e$	$1.11 \times 10^{-6} \exp(-2.94/T_e) \text{ cm}^3 \text{ s}^{-1}$	[78]
R6	$\text{Ar}^* + e \rightarrow \text{Ar}^+ + 2e$	$1 \times 10^{-6} \exp(-4/T_e) \text{ cm}^3 \text{ s}^{-1}$	[33]
R7	$\text{Ar}_2^* + e \rightarrow \text{Ar}_2^+ + 2e$	$1 \times 10^{-6} \exp(-4/T_e) \text{ cm}^3 \text{ s}^{-1}$	[19]
R8	$\text{Ar}^*(1s_5) + 2\text{Ar} \rightarrow \text{Ar}_2^*(^3\Sigma_u) + \text{Ar}$	$1.3 \times 10^{-32} F(n_e/n_a) \text{ cm}^6 \text{ s}^{-1}$	[33, 90]
R9	$\text{Ar}^*(1s_4) + 2\text{Ar} \rightarrow \text{Ar}_2^*(^1\Sigma_u) + \text{Ar}$	$1.5 \times 10^{-33} F(n_e/n_a) \text{ cm}^6 \text{ s}^{-1}$	[33, 90]
R10	$\text{Ar}_2^*(v) + \text{Ar} \rightarrow \text{Ar}_2^*(v=0) + \text{Ar}$	$1.2 \times 10^{-10} \text{ cm}^3 \text{ s}^{-1}$	[91]
R11	$\text{Ar}_2^* + e \rightarrow \text{Ar}^* + \text{Ar} + e$	$1 \times 10^{-8} \exp(-1/T_e) \text{ cm}^3 \text{ s}^{-1}$	[33]
R12	$\text{Ar}^*(i) + e \leftrightarrow \text{Ar}^*(j) + e$ $i, j = 1s_5, 1s_4, 1s_3, 1s_2$	$2 \times 10^{-7} \text{ cm}^{-3} \text{ s}^{-1}$	[92]
R13	$\text{Ar}_2^*(^3\Sigma_u)_{(v=0)} + e \rightarrow \text{Ar}_2^*(^1\Sigma_u)_{(v=0)} + e$	$5 \times 10^{-8} \text{ cm}^3 \text{ s}^{-1}$	[33, 92]
R14	$\text{Ar}_2^*(^1\Sigma_u) \rightarrow 2\text{Ar} + h\nu$	$2.4 \times 10^8 \text{ s}^{-1}$	[33]
R15	$\text{Ar}_2^*(^3\Sigma_u) \rightarrow 2\text{Ar} + h\nu$	$3.5 \times 10^5 \text{ s}^{-1}$	[33]
R16	$\text{Ar}_2^* + \text{Ar}_2^* \rightarrow \text{Ar}_2^+ + 2\text{Ar} + e_{\text{fast}}$	$5 \times 10^{-10} \text{ cm}^3 \text{ s}^{-1}$	[93]
R17	$\text{Ar}^* + \text{Ar}_2^* \rightarrow \text{Ar}^+ + 2\text{Ar} + e_{\text{fast}}$	$5 \times 10^{-10} \text{ cm}^3 \text{ s}^{-1}$	[93]
R18	$\text{Ar}^* + \text{Ar}^* \rightarrow \text{Ar}^+ + \text{Ar} + e_{\text{fast}}$	$5 \times 10^{-10} \text{ cm}^3 \text{ s}^{-1}$	[93]
R19	$\text{Ar}^*(4p) + \text{Ar} \rightarrow \text{Ar}^*(4s) + \text{Ar}$	$2 \times 10^{-11} \text{ cm}^3 \text{ s}^{-1}$	[90]
R20	$\text{Ar}^* + e \rightarrow \text{Ar} + e_{\text{fast}}$	$3 \times 10^{-10} \text{ cm}^3 \text{ s}^{-1}$	[19]

$T_e$  and  $T_g$  – electron and gas temperature in eV and K, respectively; function  $F$  is defined in [33] as  $F = (1 + 30000 n_e/n_a)^{-1}$ .

<sup>a</sup> Rate constant was calculated in this work according to the cross section from [94].

As the discharge current grows and the electron density achieves the level of about  $10^{14} \text{ cm}^{-3}$ ,  $T_e$  begins to drop because of the decrease of the electric field in the plasma and stabilizes at the equilibrium temperature of about 0.7 eV in the afterglow stage. This value was estimated from the balance between the electron heating (Penning ionization R16-R18 and super-elastic collisions R20) and cooling (R6 and R7) processes at the interaction with a long-lived reservoir of excited neutrals ( $\text{Ar}^*$ ,  $\text{Ar}_2^*$ ). More sophisticated model calculations [33] also show that after the powerful e-beam excitation pulse, when about 90 % of electrons have recombined,  $T_e$  is stabilized at about 0.8 eV during several hundreds of nanoseconds. According to the assumption in Paper II, during the secondary discharge pulses in the partially recombined plasma, the electron temperature follows the electric field oscillations. It is important to note that after the powerful excitation pulse the cooling of electrons is very fast by inelastic collisions with a reservoir of excited neutral species (reactions R6 and R7). According to the estimation, the characteristic time, which is necessary for reducing  $T_e$  from 0.9 to 0.7 eV is about 12 (1.2) ns for  $10^{15}$  ( $10^{16}$ )  $\text{cm}^{-3}$  reservoir of excited species. The cooling of electrons in elastic collisions with Ar atoms is a slower process. For example, according to [89], the characteristic time for the cooling of electrons from 0.9 to 0.7 eV is about 20 ns at 4 bar of argon.

At high pressure conditions,  $\text{Ar}^+$  ions very rapidly convert to molecular ions  $\text{Ar}_2^+$  by three-body collisions with Ar atoms (reaction R3). Dissociative recombination of  $\text{Ar}_2^+$  ions with electrons (reaction R4) leads to the build-up of the population of low-lying  $\text{Ar}^*$  levels (4s, 4s'), which brings to the growth of  $\text{Ar}_2^*$  excimers by formation reactions R8 and R9. According to [90, 95], the rate constants for the direct formation of  $\text{Ar}_2^*$  excimers in singlet and triplet states have the ratio of about 1: 9 in favour of the triplet. As was proposed in [33], constants R8, R9 depend on the function  $F = (1+30000 n_e/n_a)^{-1}$ , which shows a decrease of the excimer formation rates with the increase of the plasma ionization degree (here  $n_e$  and  $n_a$  correspond to the electron and buffer gas density respectively). This influence is caused by an especially liable dissociation of  $\text{Ar}_2^*$  excimers in high-excited vibrational states in collisions with electrons. Vibrationally relaxed excimers  $\text{Ar}_2^* \ ^3\Sigma_u^+ (v=0)$  may be also dissociated by plasma electrons (R11), however this effect is of minor importance since electrons with higher energy are necessary for this process.

The rate constants for electron-impact-induced excitation transfer from triplet to singlet  $\text{Ar}_2^*$  states (R13) were taken similarly to 4s states of  $\text{Ar}^*$  (R12). According to [92] and [33] these constants are about  $5 \times 10^{-8} \text{ cm}^3 \text{ s}^{-1}$  at  $T_e \approx 1 \text{ eV}$ . The rate constant for the reverse excitation transfer reaction (from singlet to triplet  $\text{Ar}_2^*$  excimers) is three times higher according to the ratio of statistical weights of these states.

For the simplification of the model, it was assumed that the population of 4s levels occurs as a result of dissociative recombination in accordance with their statistical weights. The existence of  $\text{Ar}^{**}$  states lying higher than 4s levels has not been taken into account in the kinetics simulation, since according to

reaction R19, these states are quenched rapidly by argon at high gas pressure to  $\text{Ar}^* 4s$  states, as the electric field is absent. Calculations show that electron collision-induced mixing (R12) is the main mechanism that holds the population of four  $4s$  levels according to their statistical weights. The electron collisions also effectively converts the reservoir of long-lived triplet  $\text{Ar}_2^*$  molecules to fast-emitted singlet  $\text{Ar}_2^*$  excimers. This mechanism predominates in the production of singlet excimers.

### 6.3. Comparison of the experimental and modeling kinetics

The experimental data along with the modeling kinetics for the high-current discharge at different Ar pressure are presented in Fig. 24. Our simple kinetic model disables to simulate the experimental kinetics during the first excitation pulse (the build-up and fall stages of the pulse). The time start point for the model calculation is shown by the arrow that corresponds to the end of the first (the most powerful) excitation pulse and the beginning of the recombination flow. The variation of the initial electron density  $n_{e0}$  and the time behaviour for the electron temperature  $T_e$  were carried out to get the best coincidence with the experimental kinetics. In these experiments the high-current excitation circuit with  $\rho = 0.68 \Omega$  ( $L_2 = 1.6 \text{ nH}$ ,  $C_p = 3.55 \text{ nF}$ ,  $f = 66 \text{ MHz}$ ) was used. This circuit enables to get the most powerful excitation in the first peak with the smallest secondary discharge peaks and the highest peak intensity of the VUV emission at 127 nm.

The first peak in the kinetics of  $\text{Ar}^*$  species has a sharp build-up front independent of the gas pressure. The powerful direct electron-impact excitation (reaction R1) under condition of a high electron temperature takes place during the breakdown stage. The subsequent steep drop in  $\text{Ar}^*$  kinetics is caused by the replacement of the direct excitation (R1) to the stepwise excitation (ionization) because of the decrease of the electron temperature. The rate of the next relatively flat build-up of the density of low-lying  $\text{Ar}^*$  states, depends on the gas pressure and is connected with the recombination return flow. The experimentally observed characteristic return time decreases strongly with the pressure increase: from  $\sim 40 \text{ ns}$  at 1 bar to  $\sim 24$ ; 8; 6 ns at 2; 4; 6 bar respectively. This time is caused by the chain of several pressure-accelerated reactions: dimerization of  $\text{Ar}^+$  ions to  $\text{Ar}_2^+$  ions (R3); dissociative recombination of  $\text{Ar}_2^+$  ions (R4); electron (atom)-collisional cascades [42, 43]. These processes rapidly collapses the excited argon atomic manifold to the lowest excited  $\text{Ar}^* 4s, 4s'$  states. It should be noted that in spite of the pressure-accelerated reactions, kinetics at 4 and 6 bar are spread in time because of the electro-technically mismatched excitation conditions (see Chapter 3.1). In this case the energy loaded into the plasma is distributed among several excitation pulses.

The electron temperature reflects the heating-cooling of electrons during the secondary discharge excitation pulses. This mismatching effect is more pronounced for the excitation circuit with high parameter  $\rho$  (see Fig. 26, 27).

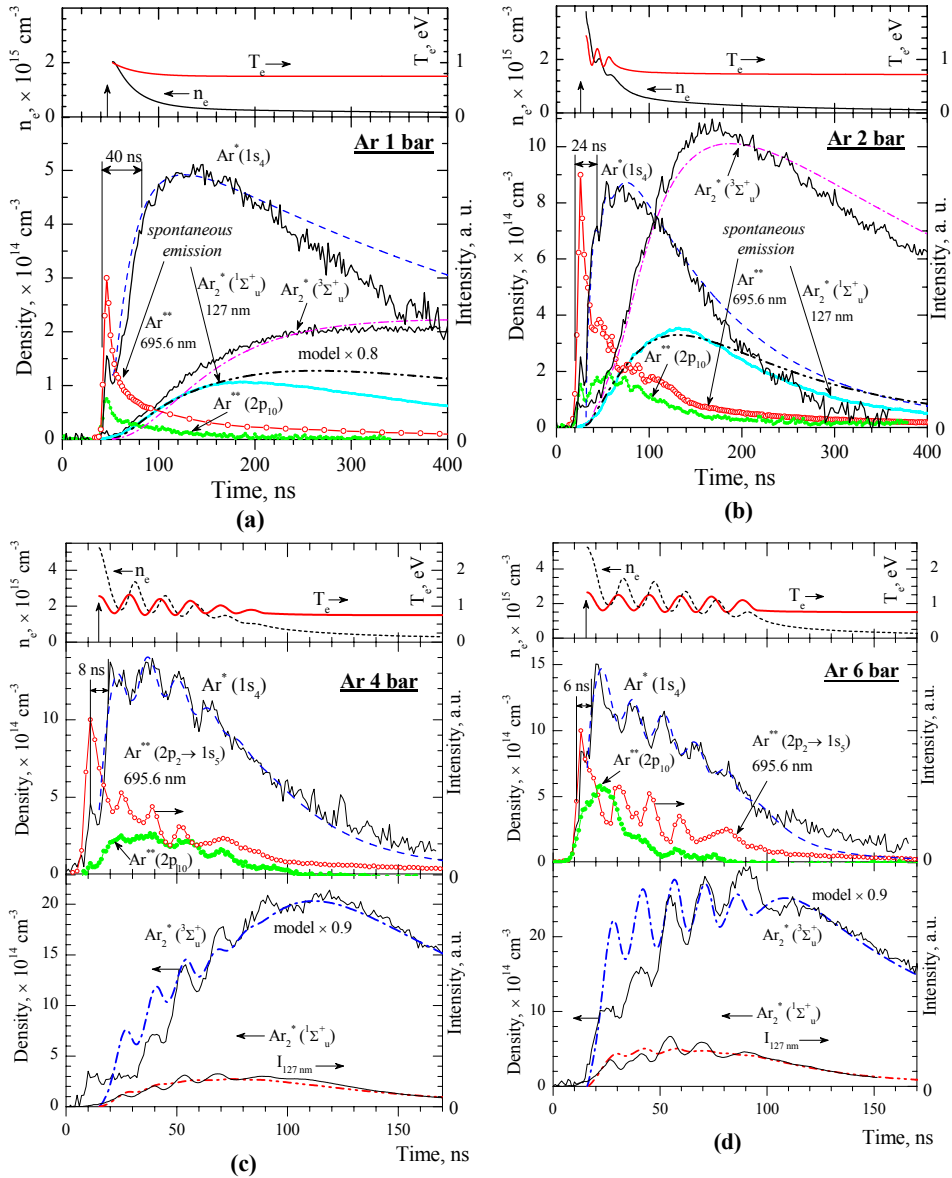


**Figure 24.** Experimental (solid lines) and modeling (dash lines) kinetics for densities of  $\text{Ar}^* 4s, 4p$  states, triplet  $\text{Ar}_2^* \ ^3\Sigma_u^+ (v=0)$  molecules along with kinetics of VUV (127 nm) and red  $\text{Ar}^{**}$  line (696.5 nm) spontaneous emissions of the high-current discharge at different Ar pressure. The initial time point for the modeling is shown by the arrow.

The pressure dependences of the experimentally obtained peak densities of  $\text{Ar}_2^*$  excimer molecules at  ${}^3\Sigma_u^+$  ( $v=0$ ) state and  $\text{Ar}^*$  atoms at  $1s_4$  state, as well as the peak of VUV (127 nm) spontaneous emission, which is proportional to the density of  ${}^1\Sigma_u$  ( $v=0$ )  $\text{Ar}_2^*$  excimers, are shown in Fig. 25. The maximal experimental density of the triplet  ${}^3\Sigma_u$  ( $v=0$ )  $\text{Ar}_2^*$  excimers is equal to  $2.9 \times 10^{15} \text{ cm}^{-3}$  at 6 bar. According to the estimation, the correspondent maximal density of the singlet  $\text{Ar}_2^*$  excimers is about five times smaller than the triplet one (about  $6 \times 10^{14} \text{ cm}^{-3}$ ).

To investigate the influence of the secondary discharge pulses on the emission kinetics, the electrical peaking circuit with the higher parameter  $\rho$  ( $\rho = 1.3 \Omega$ ,  $L_2 = 7 \text{ nH}$ ,  $C_p = 6.8 \text{ nF}$ ), provided the strong oscillations, was specially used. The lower oscillation frequency ( $f \sim 21 \text{ MHz}$ ) enabled to ensure the correct measurement of the voltage on the discharge gap without the phase-frequency distortions, which take place at higher frequencies. Several problems of careful synchronization with optical signals and voltage waveforms were also much easier to solve with a low-frequency contour. Figure 26 shows the voltage between the electrodes for the discharge at 4 bar of Ar in comparison with the kinetics of VUV  $\text{Ar}_2^*$  emission at 127 nm, the UV-VIS continuum (550 nm) and  $\text{Ar}^{**}$  line at 696.5 nm. The secondary excitation pulses modulate the VUV and visible emission intensity with the oscillation frequency equal to the double intrinsic frequency of the peaking contour. During these oscillations, when the plasma resistance does not changed significantly, the current waveform is close to the discharge voltage curve. Thus, the power deposition is roughly proportional to the square of the voltage. The experimental data verified that independent of the pressure and oscillation frequency, the modulations of VUV

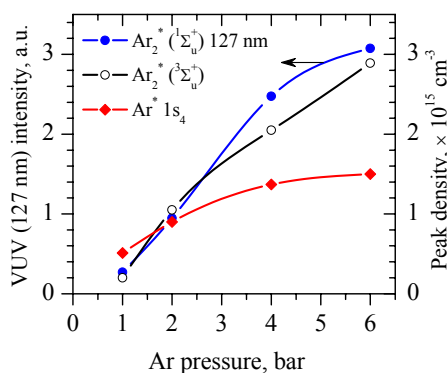


**Figure 25.** Peak densities of the main excited species and the maximal intensity of the VUV (127 nm) spontaneous emission as a function of argon pressure (experimental data from Fig. 24 are used).

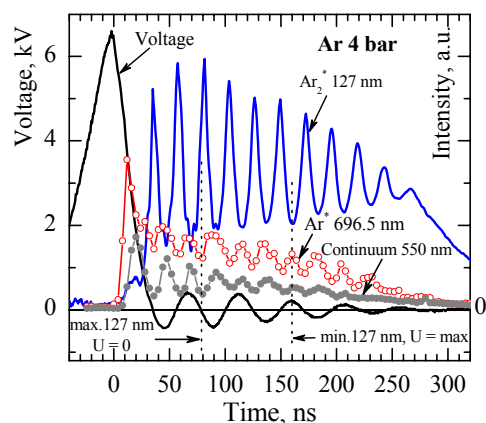


**Figure 26.** Emission kinetics of  $\text{Ar}_2^*$  (127 nm), UV-VIS continuum (550 nm),  $\text{Ar}^{**}$  line (696.5 nm) and the voltage between electrodes in 4 bar of Ar discharge. The peaking circuit with  $\rho = 1.3 \Omega$  and long nickel electrodes were used.

emission are in the opposite phase with the emission of the UV-VIS continuum and Ar\*\* red line. The maxima of VUV radiation observed when the voltage achieves local maxima. It should be noted that the amplitude of the modulations of VUV radiation depends on the homogeneity of the discharge: the more filamentary is the discharge, the more intense is the UV-VIS continuum and the stronger are the modulations in the VUV emission at 127 nm.

The experimental results, obtained at the same discharge conditions as in Fig. 26 and corresponding simulations for kinetics of the density of triplet  ${}^3\Sigma_u(v=0)$  Ar<sub>2</sub>\* excimers and VUV emission from singlet  ${}^1\Sigma_u(v=0)$  Ar<sub>2</sub>\* excimers are shown in Fig. 27. The maximal density of triplet excimers, averaged on the length of electrodes, is about 3 times smaller than at the same pressure for the contour with lower  $\rho$  (Fig. 24c). The modeling gives a good qualitative agreement with the experimental results. However the simulated density of triplet excimers is 6.7 times higher than measured in the experiment. This difference could be explained by the discharge longitudinal fragmentation (see Fig. 13), which takes place after the first powerful excitation peak. From these

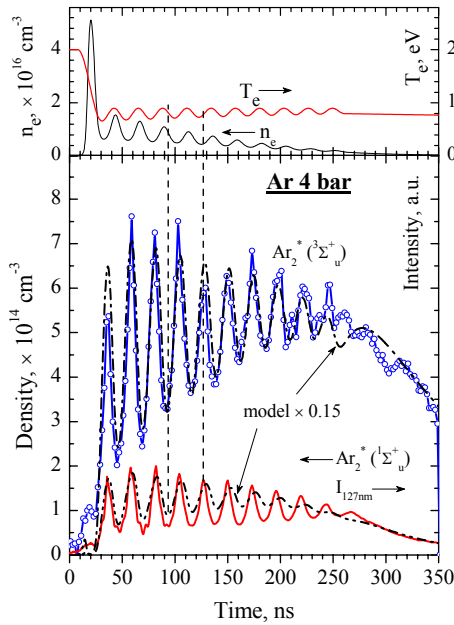


**Figure 27.** Experimental (solid curves) and modeling kinetics for the densities of singlet Ar<sub>2</sub>\*  ${}^1\Sigma_u^+(v=0)$ , triplet Ar<sub>2</sub>\*  ${}^3\Sigma_u^+(v=0)$  molecules and VUV (127 nm) emission. The circuit with a high parameter  $\rho$  ( $\rho = 1.3 \Omega$ ) is used. The modeling kinetics of electron density and temperature are shown in the upper part.

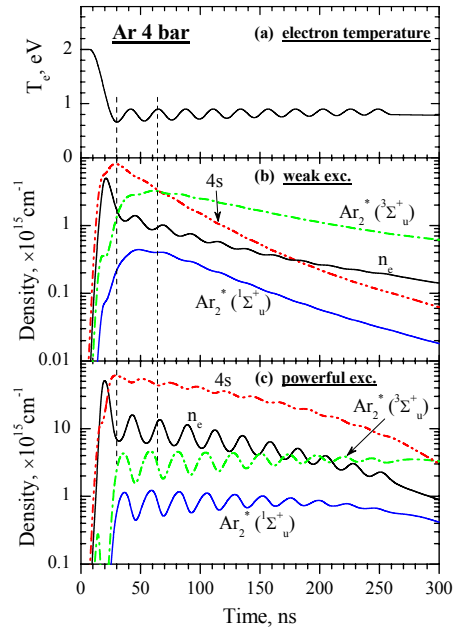


**Figure 28.** The modeling kinetics for plasma species at relatively weak ( $n_{e \max} = 4.8 \times 10^{15} \text{ cm}^{-3}$ ) (b), and powerful ( $n_{e \max} = 4.8 \times 10^{16} \text{ cm}^{-3}$ ) (c) excitation for 4 bar of Ar. Kinetics for  $T_e$  (a) is proposed the same for both regimes and reflects the heating-cooling of electrons in the secondary discharge excitation pulses.

considerations, the effective length of the discharge during the secondary excitation peaks is reduced from 20 cm to about several centimetres.

The modelling shows that the strong modulations of the excited species ( $\text{Ar}^*$ ,  $\text{Ar}_2^*$ ), which follow the behaviour of  $T_e$  during the secondary discharges become apparent only at a high degree of plasma ionization ( $\sim 10^{-3}$ – $10^{-4}$ ). This statement is illustrated by Fig. 28. Two excitation regimes were modeled (the relatively weak and the powerful first pulse). Both regimes are proposed to have the same kinetics for the electron temperature during the secondary discharge pulses (Fig. 28a). At the weak excitation (Fig. 28b), the electrons achieve the maximum density of  $4.8 \times 10^{15} \text{ cm}^{-3}$ . For a powerful regime (Fig. 28c) this value is chosen as 10 times higher. In the first case, the oscillations of the electric field lead to an insignificant modulation of the densities of plasma species. The modulation is more pronounced in the case of a powerful excitation. The main reason of this difference is connected with the relatively strong dependence of the rate constants for reactions R6, R7 on  $T_e$  in the range of about 1 eV. The increase of  $T_e$  and  $n_e$  leads to the rise of the stepwise ionization of  $\text{Ar}^*$  and  $\text{Ar}_2^*$  species, resulting in deep holes in their kinetics. When  $T_e$  falls, the plasma equilibrium shifts to the recombination direction – the electron density decreases and the maxima of  $\text{Ar}^*$  and  $\text{Ar}_2^*$  species are observed. An additional heating of electrons during the secondary discharge pulses is a very undesirable process. It suppresses the recombination flow in the plasma and, as a result, the kinetics are spread in time with decreasing of the peak densities of all excited species. This effect is more pronounced at a high ionization degree of the plasma.

#### 6.4. The role of electrons in the formation of $\text{Ar}_2^*$ excimers

According to the list of reactions in Table 2, there are two possible channels for the formation of  $\text{Ar}_2^*$  excimers in the singlet state: 1) the direct formation of vibronically hot singlet  $\text{Ar}_2^*$  molecules in three-body collisions (reaction R9) with further relaxation in collisions with argon atoms (reaction R10); and 2) electron-induced excitation transfer from triplet to singlet states of  $\text{Ar}_2^*$  excimers (reaction R13). If vibronically hot  $\text{Ar}_2^*$  molecules exist in plasma, then the emission of the first argon continuum should be observed. To estimate the input of these two channels to the excimer formation, emission kinetics of the first and second continua should be measured. For this aim, the low-inductive peaking contour with  $\rho = 0.68 \Omega$  was used. This circuit permits to get the most powerful excitation in the first peak with the smallest secondary discharge peaks, which could be neglected in the model.

The experimental emission kinetics of the first and second continua of argon together with the UV–VIS continuum at 258 nm are shown in Fig. 29. The

measurements were carried out with a VUV monochromator and solar blind photomultiplier at 4 bar of argon. The signal from the first continuum was rather weak, thus correction for the stray light in the monochromator, caused by the strong emission from the second continuum, was carried out. It was verified that the emission kinetics of the first continuum at 115 and 150 nm, corresponding to the right and left turning points on the potential curve of the singlet  $\text{Ar}_2^* \ ^1\Sigma_u^+(v)$  excimer (see Fig. 2), were very similar. Since the vibrational relaxation of hot  $\text{Ar}_2^*$  excimers is very fast (characteristic time of reaction R10 is about 0.1 ns at 4 bar of argon), then only a small part of these species is able to decay spontaneously with the emission of a photon.

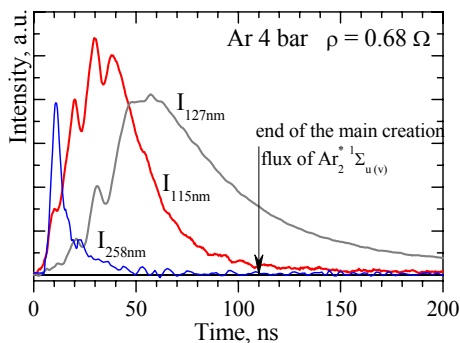


**Figure 29.** Experimental kinetics of the first (115 nm) and second (127 nm) continua of argon along with the UV-VIS continuum (258 nm) in 4 bar Ar discharge. The low-inductive discharge circuit with  $\rho = 0.68 \ \Omega$  and Ni electrodes was used.

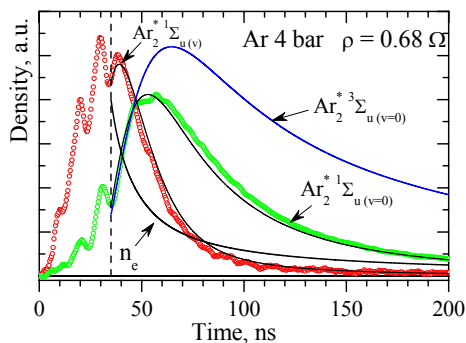


**Figure 30.** Experimental kinetics (points) of the first and second argon continua and calculated behaviours (solid lines) for  $\text{Ar}_2^*$  excimers in singlet  $^1\Sigma_u(v=0)$  and triplet  $^3\Sigma_u(v=0)$  states and electrons  $n_e$ .

The rate constant for electron collision-induced mixing (reaction R13) is taken analogously to the corresponding one for  $\text{Ar}^*$  atom. According to [92] the rate constant of electron-impact-induced excitation transfer from the metastable to the resonant  $\text{Ar}^*$  state is about  $5 \times 10^{-8} \text{ cm}^3 \text{ s}^{-1}$  at  $T_e \approx 1 \text{ eV}$ . The rate constant for the reverse reaction (from singlet to triplet  $\text{Ar}_2^*$  excimers) is three times higher according to the ratio of statistical weights of these states. The same constants have been used also in [33].

The experimental curves in Fig. 29 show that the emission of the first continuum decreases significantly at the stage when most of the electrons, created during the first excitation pulse, are recombined; and  $\text{Ar}^*$  atoms, as the product of the recombination, are converted to  $\text{Ar}_2^*$  excimers. This approximate time point is signified by the arrow. Thus the emission of the second continuum after this point is possible only by the conversion of excimers from a long-lived

triplet reservoir to singlet states by residual electrons. In the frame of the presented model, the decay kinetics of the first and second continua after the short pulse excitation was calculated. The initial densities of the key species were used as the starting parameters. The electron temperature (in eV) was modelled as a falling exponential function  $T_e = 0.25 \times \exp(-t/\tau) + 0.75$ , with  $\tau = 15$  ns. The comparison of the calculated and experimental kinetics is presented in Fig. 30. The initial time point for the calculated kinetics is fixed at 35 ns after the beginning of the experimental curves (this moment is shown by a dashed vertical line). Such simplification was used to avoid the influence of the weak secondary discharge pulses on the kinetics. The best agreement with the experimental data was obtained for the initial densities of electrons and Ar\* atoms of  $2.4 \times 10^{15} \text{ cm}^{-3}$ . The calculated peak densities for the Ar<sub>2</sub>\* excimers have the following values:  $2.2 \times 10^{15} \text{ cm}^{-3}$  for Ar<sub>2</sub>\* <sup>3</sup>Σ<sub>u</sub><sup>+</sup><sub>(v=0)</sub>;  $2.7 \times 10^{14} \text{ cm}^{-3}$  for Ar<sub>2</sub>\* <sup>1</sup>Σ<sub>u</sub><sup>+</sup><sub>(v=0)</sub> and  $1.7 \times 10^{12} \text{ cm}^{-3}$  for Ar<sub>2</sub>\* <sup>1</sup>Σ<sub>u</sub><sup>+</sup><sub>(v)</sub>. Thus, according to the model calculation, the maximal densities of the singlet and triplet Ar<sub>2</sub>\*<sub>(v=0)</sub> excimers differ by eight times. The peak densities of vibrationally hot and cold singlet Ar<sub>2</sub>\* excimers differ by about 160 times. The calculated kinetics in Fig. 30 show that in the afterglow stage, the Ar<sub>2</sub>\* singlet excimers decay faster than triplets. This difference is connected with the continuous decrease in the electron density due to recombination, which slows down the rate of the electron collision-induced mixing reaction. According to the estimation this mixing is dominant in the production of singlet Ar<sub>2</sub>\* excimers at a gas pressure of several bars. This mechanism prevails over the reaction of the direct formation R9 of about 20–30 times in the afterglow stage and of 2–5 times on the build-up of the second continuum emission.

## **6.5. Conditions for amplification of VUV emission from Ar<sub>2</sub>\* excimers**

In this section the lasing possibilities will be considered for the active medium consisting of Ar<sub>2</sub>\* <sup>1</sup>Σ<sub>u</sub><sup>+</sup><sub>(v=0)</sub> excimers. The gain value of  $0.01 \text{ cm}^{-1}$  mentioned in Chapter 2.4 is usually used in the literature for the theoretical estimation of the lasing threshold for the excimer lasers. However, in practice, the net gain  $g = g_0 - k$  could be much lower, because inevitable losses  $k$  inside the resonator (absorption in plasma, losses on the mirrors, deflection of the amplified emission [Paper VI]) have been always presented. The estimations in the frame of the model show that the absorption at 127 nm is negligible for Ar<sub>2</sub><sup>+</sup> ions [96] and Ar\* atoms (the absorption cross section is  $10^{-19} \text{ cm}^2$  [97]). Photoionization of Ar<sub>2</sub>\* gives the main, but relatively small input to the absorption losses. For example, for the high-current discharge excitation of argon at 10 bar, photoionization losses achieve  $0.01 \text{ cm}^{-1}$  (the absorption cross section is  $5 \times 10^{-19} \text{ cm}^2$  [98]). However, as was revealed for the real electron beam-pumped

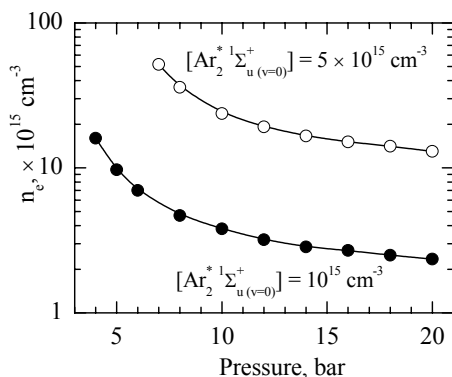
Ar<sub>2</sub> laser devices [33, 99], the dominant absorption losses are due to impurities, possibly originated by evaporation from the laser chamber materials. These unidentified impurities, which gave the absorption losses of about 0.05 cm<sup>-1</sup>, were successfully removed by the cooling of the chamber down to 170 K [99]. With regard to the mirror losses, it is necessary to take into account that the practical number of round trips in the resonator is limited to 5–10 for the fast kinetics of excimers at a high pressure. Commercially available VUV mirrors have a rather low reflection coefficient at 127 nm (~83%), hence, for the relatively short active media (~ several tens of centimetres), a high gain is required for a reliable lasing. Thus, a more realistic threshold density for Ar<sub>2</sub>\* <sup>1</sup>Σ<sub>u</sub><sup>+</sup><sub>(v=0)</sub> excimers is about 5×10<sup>15</sup> cm<sup>-3</sup>, which corresponds to the gain of 0.05 cm<sup>-1</sup>. This gain is close to the experimental values in the existing electron beam pumped Ar<sub>2</sub> excimer lasers [99, 100].

Figure 31 shows the calculations of the electron density, which must be created in the peak of a short pulse discharge excitation to achieve the threshold density of Ar<sub>2</sub>\* <sup>1</sup>Σ<sub>u</sub><sup>+</sup><sub>(v=0)</sub> excimers at different argon pressures. In the model, T<sub>e</sub> of 2 eV was fixed before the breakdown, after the breakdown T<sub>e</sub> fell to 0.75 eV during 10 ns and stabilized at this value during the recombination kinetics. The gas temperature is fixed at 300 K. Two threshold densities of Ar<sub>2</sub>\* <sup>1</sup>Σ<sub>u</sub><sup>+</sup><sub>(v=0)</sub> excimers were chosen: 10<sup>15</sup> cm<sup>-3</sup> (optimistic value) and 5×10<sup>15</sup> cm<sup>-3</sup> (realistic value). According to the modeling, a weaker excitation is required to achieve the threshold at a higher pressure compared with a lower one. This conclusion is explained by the faster formation rate of the triplet excimers at a higher pressure (reaction R8). As follows from Fig. 31, the minimal pressure of 4 bar is required to achieve the threshold of 10<sup>15</sup> cm<sup>-3</sup>. The density balance between singlet and triplet Ar<sub>2</sub>\* excimers is 1:6 in favour of the triplet. To achieve the threshold of 5×10<sup>15</sup> cm<sup>-3</sup>, the gas pressure should be higher than 7 bar and a very high peak density of electrons is necessary. In this case, the residual electron density n<sub>e</sub>(t) remains high enough to deplete the accumulated triplet reservoir more effectively – the density balance is 1:4 in favour of the triplet. A further increase in n<sub>e</sub>(t) leads to insignificant growth of the VUV radiation, because the achievable balance between singlet and triplet states is limited according to their statistical weights as 1:3.

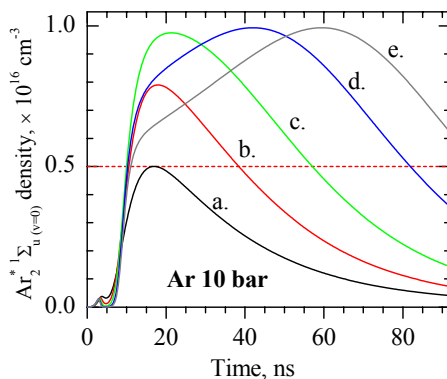
These modeling data is interesting to compare with the density of Ar<sub>2</sub>\* excimers in singlet state, obtained in our real discharge devices (see Fig. 25, 27). The maximal obtained density was 6×10<sup>14</sup> cm<sup>-3</sup> for the homogeneous discharge at 6 bar and about 10<sup>15</sup> cm<sup>-3</sup> for the fragmented discharge at 4 bar. These values are rather close to the estimated optimistic threshold; however that was not enough for the observation of lasing in the experiment. Higher gas pressure and more powerful discharge pumping are necessary. Certainly, it is a big technical challenge to organize the arc-free high-current discharge at the gas pressure of about 10 bar.

Figure 32 shows the calculated kinetics for Ar<sub>2</sub>\* <sup>1</sup>Σ<sub>u</sub><sup>+</sup><sub>(v=0)</sub> excimers for different peak densities of electrons in short pulse excitation at 10 bar of Ar.

The criterion for the realistic VUV lasing at 127 nm could be realized at 10 bar of Ar by a single pulse discharge excitation with a peak electron density of about  $2.4 \times 10^{16} \text{ cm}^{-3}$  under the condition of a fast cooling of electrons to  $T_e$  of 0.75 eV after the excitation pulse. The model predicts that if the electron density exceeds about  $10^{17} \text{ cm}^{-3}$ , the saturation of the peak intensity for the second continuum emission should be observed. At a high electron density, several undesirable reactions become significant: the efficiency of the excimer creation reaction R8 decreases; the rates of destruction reactions R7 (ionization of excimers) and R11 (dissociation of excimers) increase. At the saturation regime, the kinetic of excimers is spread in time and the peak density is delayed.



**Figure 31.** Calculated electron density, which must be created in the peak of a short pulse excitation to achieve the threshold density of  $\text{Ar}_2^* \Sigma_u^+(v=0)$  excimers of  $10^{15} \text{ cm}^{-3}$  (full points) and  $5 \times 10^{15} \text{ cm}^{-3}$  (empty points).



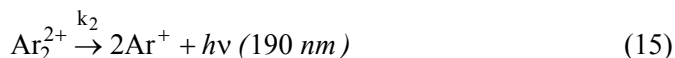
**Figure 32.** Calculated kinetics for  $\text{Ar}_2^* \Sigma_u^+(v=0)$  excimers at different peak densities of electrons at short pulse excitation at 10 bar of Ar. (a)  $2.4 \times 10^{16} \text{ cm}^{-3}$ ; (b)  $5 \times 10^{16} \text{ cm}^{-3}$ ; (c)  $1 \times 10^{17} \text{ cm}^{-3}$ ; (d)  $2 \times 10^{17} \text{ cm}^{-3}$ ; (e)  $2.9 \times 10^{17} \text{ cm}^{-3}$ . The horizontal line shows the realistic threshold for the lasing.

One can suggest that such saturation explains the experimental results obtained in [18]. In this paper after the very powerful discharge pulse excitation at 9 bar of Kr the peak of spontaneous VUV emission of  $\text{Kr}_2^*$  excimers and its lasing at 148 nm were achieved at about 2  $\mu\text{s}$  delay from the breakdown.

## 7. THE THIRD CONTINUUM EMISSION IN THE DISCHARGE AT A REDUCED PRESSURE

### 7.1. About the nature of the third continuum

Besides the intensive second continua, the so-called third continua bands for rare gases have been widely discussed in the literature. For argon this band is centred at about 190 nm at low pressures. Usually, this continuum has been excited by different high-energetic projectile particles: electrons [19], protons [20],  $\alpha$ -particles [23] and heavy ions [21, 22]. In this row, the intensity of the third continuum grows with the energy of the excitation particles and in the case of heavy ions it becomes even comparable with the most intense second continuum. According to paper [101], the key feature of such excitation is a significant multiple ionization of argon atoms in a single collision with a high-energetic projectile particle. For example, with the excitation of argon gas by 34 MeV  $\text{Cl}^{9+}$  ions [102], the ratio of  $\text{Ar}^{2+}/\text{Ar}^+$  production is about 30 %. For electron excitation, this ratio is 5 % and is almost independent of the impact electron energy from 70 to 800 eV [103]. This supports the assignment of the third continuum to the emission of double charged molecular ions  $\text{Ar}_2^{2+}$ . The chain of the reactions leading to the formation of  $\text{Ar}_2^{2+}$  excimers, proposed in paper [104], is the following:



where X is a bombarding particle. The double ionization of Ar atoms by electron impact excitation is shown on the energy level diagram in Fig. 33.

The alternative assumption of assignment the third continuum to the decay of the single charged  $\text{Ar}_2^{+*}$  molecular ions, produced in  $\text{Ar}^{+*} + 2\text{Ar}$  or  $\text{Ar}^* + \text{Ar}^+ + \text{Ar}$  reactions, has also been discussed in the literature [23, 105, 106]. These reaction pathways are unlikely due to several arguments stated, for example, in [107]. In contrast to the high-energetic particle excitation, electrons in discharge plasma are characterized by a much lower energy (the electron temperature is about 1 eV), therefore, the production of  $\text{Ar}^{2+}$  ions seems to be negligible. This explains why the third continuum has not been usually observed under the discharge excitation.

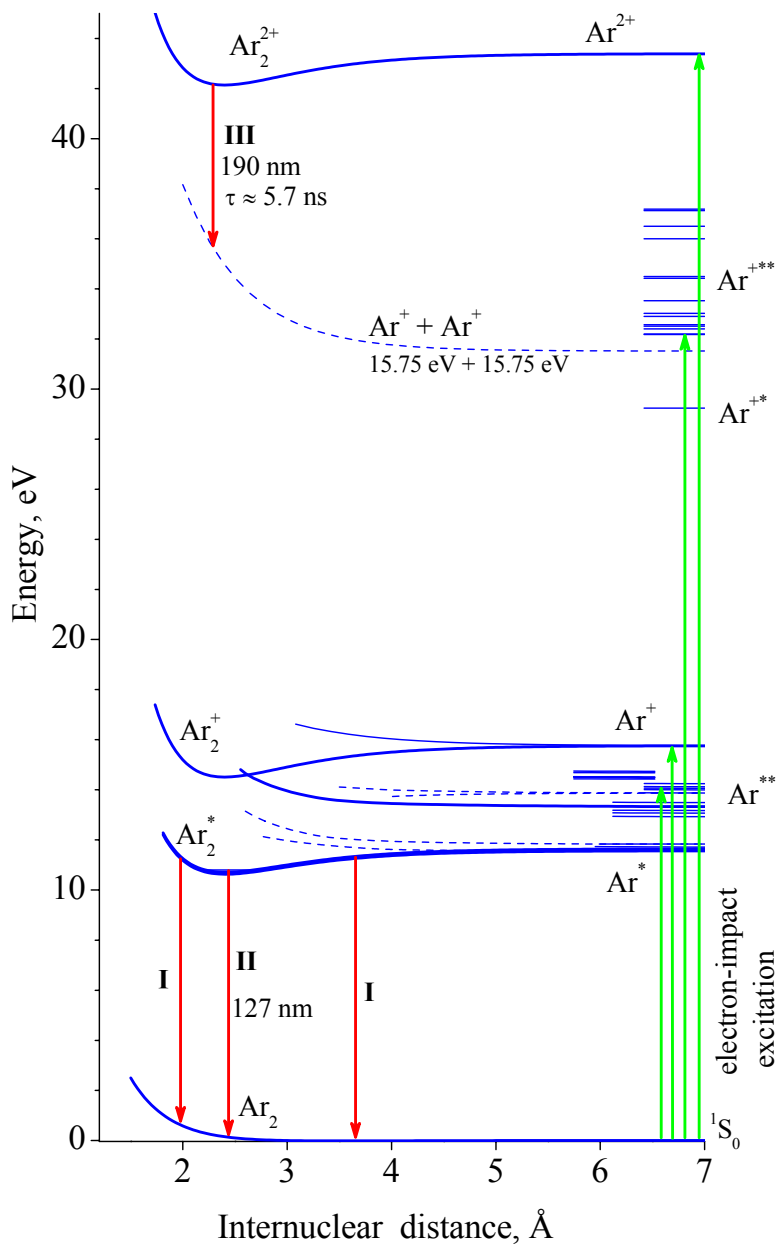
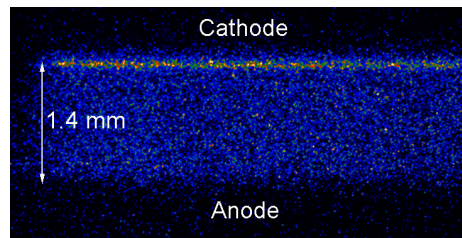


**Figure 33.** Schematic energy level diagram of excited, single and double ionised states of argon.

## 7.2. Spatial structure and time dependent spectra of the third continuum emission

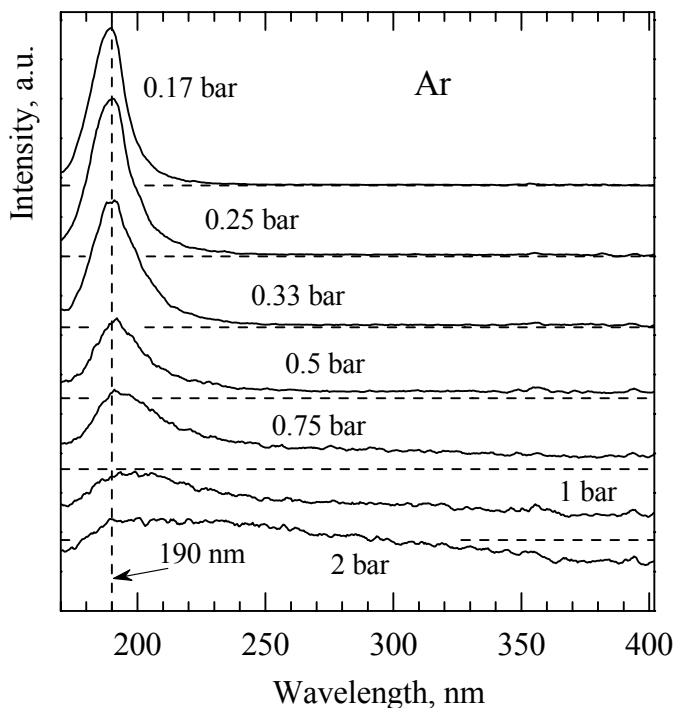
For the detection of the weak third continuum in argon in the VUV-UV region, it is necessary to reduce the intensity of other types of emission. These can be the stray light from the strong second continuum and the UV-VIS photorecombination continuum. The stray light of the second continuum was totally excluded by the quartz cut-off filter, which absorbs the light with the wavelength shorter than 165 nm. The reducing of UV-VIS continuum radiation is technically more complicated task. Emission of the photorecombination continuum prevails in plasma with a high density of electrons due to  $n_e^2$  dependence of its intensity (see Fig. 21). Thus the discharge with reduced  $n_e$  should be used. For this purpose, the excitation scheme (b) from Fig 5 with  $L_2 = 500$  nH and  $C_0 = 0.68$  nF was applied, which produces very homogeneous discharge with a low-current single-pulse excitation. High homogeneity of the discharge is demonstrated in Fig. 34. Here, the stable cathode layer without any hot cathode spots is formed, and the positive column together with the negative glow zone is very uniform. The discharge had the similar structure at the pressure range of 0.17–0.75 bar. At higher pressures separated weak cathode spots began to appear, and at pressure more than 3 bar the discharge constricted.

Figure 35 shows continua spectra of the discharge at different gas pressures. The emission of the plasma was spatially integrated over the whole inter-electrode gap. The spectra were measured with UV photomultiplier R3377 and VUV monochromator at the time points when the peak intensity of 190 nm band was maximal (see Fig. 39). The intensity scale is the same for all the curves. The spectra were not corrected for the spectral sensitivity of the registration system. According to Fig. 35, the maximal intensity of the third continuum is observed at 0.25 bar. At a higher pressure, the peak intensity of the 190 nm band decreases and the band shape spreads out to the red side (an additional broad band, centered at about 220 nm, appears). At the same time, the UV-VIS photorecombination continuum increases. The radiation of the third continuum is difficult to detect at pressures above 1 bar, as its intensity is negligible in comparison with the emission of UV-VIS continuum. A number of  $\text{Ar}^{+*}$  emission lines was also detected in the UV spectral range. The imaging experiments with ICCD camera show that, in contrast to the photorecombination continuum, the third continuum



**Figure 34.** Side-view image of the discharge in Ar at 0.5 bar, measured in the visible light (SZS-21 filter, 340–680 nm). The low-current excitation circuit (b) from Fig. 5 is used. Exposure time – 4 ns, delay – 16 ns after the breakdown.

band at 190 nm and  $\text{Ar}^{+*}$  lines are emitted exclusively from the negative glow zone, but not from the positive column of the discharge.



**Figure 35.** Continua spectra of the discharge in the UV range at different gas pressures. The intensity scale is the same for all the curves.

Figure 36 shows the time-dependent spectra in the UV range for the discharge in Ar at 0.25 bar, with a time step of 4 ns. The emission signal was collected from the negative glow zone. The emission of  $\text{Ar}^{+*}$  lines is observed only during the excitation pulse, but the third continuum exhibits a behaviour, typical for plasma-chemical kinetics. It should be noted that the second continuum of argon has much slower kinetics than the third continuum. The maximum of the VUV emission at 127 nm is achieved when the third continuum has already been decayed.

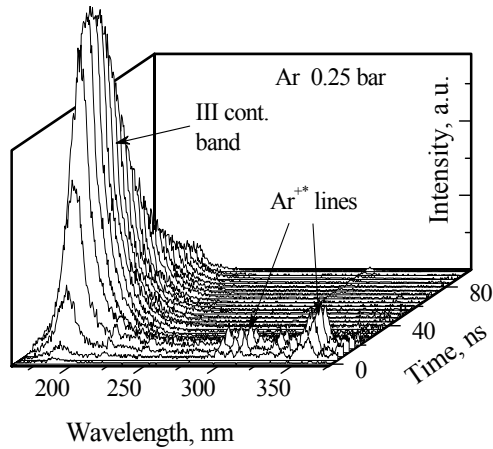


**Figure 36.** Time-dependent spectra in the UV range from the negative glow zone of the discharge in Ar at 0.25 bar.

### 7.3. The excitation mechanism of the third continuum

For the interpretation of presented experimental results, the conception of runaway electrons [108, 109] is applicable. The electrons in a weakly ionized low-temperature discharge plasma get the energy of directional motion from the electric field, and spend this energy mainly for the ionization and excitation of neutral particles (inelastic losses). When the  $E/N$  parameter (the ratio of the electric field to the gas density) is high enough, the electron goes from the drift mode into the mode of continuous acceleration [110]. The correspondent critical field for argon is calculated as  $E_{cr}/N = 4.2 \times 10^{-14} \text{ V cm}^2$  (4.2 kTd). Such a high parameter is experimentally reached in the positive column only in very fast pulse discharges with a strongly non-uniform electric field [111].

Figure 37 demonstrates breakdown voltage  $U_{br}$  at different argon pressures and the correspondent  $E/N$  parameter in the positive column measured for the pulsed discharge excited by the circuit (a) in Fig. 5. Due to the fast rise time of the voltage, the breakdown voltage  $U_{br}$  is approximately twice as high as the static breakdown value, described by the Paschen curve [38]. These data show that in present conditions, the  $E/N$  parameter is 25–100 times lower than is required for the production of runaway electrons in the positive column. However, in the cathode layer, the electric field is much higher than in the positive column and can exceed the critical field  $E_{cr}/N$ , therefore one can suggest that runaway electrons are created in the cathode layer. These electrons could be accelerated further in the positive column if the interelectrode field is high enough (such as, for example, in [111]), but in present case, the electrons

are retarded in the narrow zone of the negative glow. High-current pulse discharges at a reduced pressure are usually operated in the abnormal mode. Such parameters as the cathode fall, the electric field in the cathode layer and the current density significantly exceed the corresponding values for the normal glow discharge [38, 39].

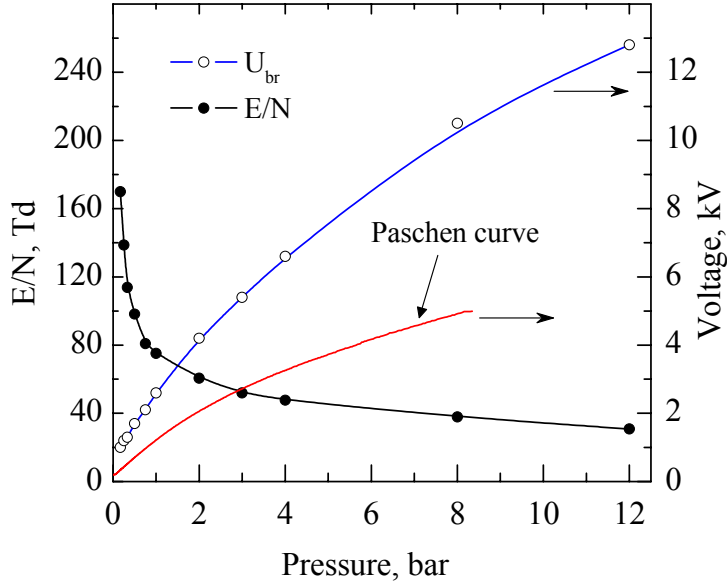


**Figure. 37.** Experimental data for the breakdown voltage and  $E/N$  parameter for the high-current discharge at different Ar pressure (discharge gap is 1.4 mm). The right-hand branch of the Paschen curve for the static breakdown in Ar is shown (data from [38]).

Table 3 demonstrates the experimental and calculated characteristics of the cathode layer for pulse discharge conditions with Ni electrodes at different argon pressures. The maximal current densities (column 2), estimated from the experiment, are much higher than the calculated normal current density (column 3) at a reduced argon pressure. The calculated maximal cathode fall (column 4) is between 130 and 245 V (the normal cathode fall is 130 V). After the calculation of the cathode layer thickness (column 5), the  $E/N$  parameter in the cathode layer is determined (column 6).

The electron in the field  $E/N$  is accelerated up to the energy  $\varepsilon$ , when the balance between the energy acquired from the field and inelastic losses is achieved. According to [110], this condition is described by the formula (16)

$$\frac{E}{N} = 2\pi e^3 \frac{z}{\varepsilon} \ln \frac{2\varepsilon}{I} \quad (16)$$

**Table 3.** Characteristics of the cathode layer for the pulse discharge at different Ar pressures

Pressure (bar)	Experimental max. current density (A/cm <sup>2</sup> )	Normal current density (A/cm <sup>2</sup> )	Cathode fall (V)	Thickness of the cathode layer (μm)	E/N in the cathode layer (kTd)
0.17	81	2.5	245	12.6	19
0.25	97	5.6	201	9.0	11
0.33	105	10	177	7.4	7.4
0.5	138	22.5	157	5.4	4.6
0.75	170	50.6	142	4.1	2.9
1	211	90	136	3.4	2.2
2	360	360	131	2.2	1.2

where  $E/N$  is in V cm<sup>2</sup>,  $I$  is the average energy of inelastic losses (45 eV for Ar),  $z$  is the number of electrons in the atom (18 for Ar), and  $e$  is the elementary charge. The maximal possible electron energy in the cathode layer at the corresponding  $E/N$  parameters (from column 6 in Table 3) is limited by condition (16) or by the cathode fall potential. The corresponding values of the electron energy at different pressures are marked by the points on the solid and dashed limiting curves in Fig. 38. Thus the electrons in the pressure range of 2–0.75 bar can be accelerated only up to the energy of 25–33 eV, since  $E/N < E_{cr}/N$  (the point of  $E_{cr}/N$  is signed on the solid curve). However, at lower pressures the appearance of runaway electrons is possible ( $E/N$  becomes higher than  $E_{cr}/N$ ). The electrons in the cathode layer can achieve the energy of the cathode fall potential: 157–245 eV (column 4 in Table 3). These points are approximated with the dashed curve in Fig. 38. This estimation is rather rough, because the real electric field around the manifold of the sharp micro-protrusions on the surface of the cathode is unknown. According to [112], the electric field near such micro-protrusion can be increased to tens and even hundreds of times, compared to the idealized flat surface. High micro-fields on the cathode surface are sufficient for the generation of runaway electrons by the field emission mechanism. This emission transforms very rapidly to an explosive electron emission, which destroys the cathode layer and terminates the generation of runaway electrons. The explosion delay time is measured as about  $10^{-10}$  s at high current densities [109].

The experimental data support these ideas. Really, in the low-current excitation regime where the cathode layer is not destroyed during the excitation pulse, the third continuum emission was very stable. High-current excitation leads to the explosive electron emission from hot cathode spots in the second half of the excitation pulse. As a result, the cathode layer is destroyed and the signal from the third continuum becomes very noisy.

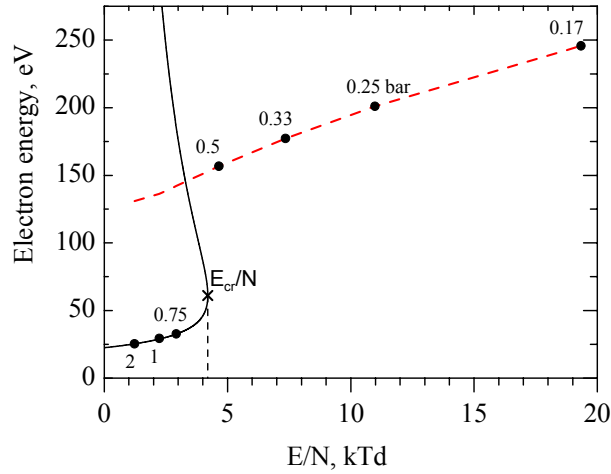


**Figure 38.** The maximal possible energy of electrons (points) in Ar according to the following conditions:

1. Solid curve is calculated from formula (16);
2. Dashed curve is the approximation of the maximal achievable energy of electrons, limited by the cathode fall potential (column 4 in Table 3).

The emission of the observed  $\text{Ar}^{+*}$  lines belongs to the transitions from the excited levels with the energy of 35.5–39.6 eV above the ground state of Ar, which is rather close to the level of double ionization of Ar (43.39 eV). Thus both  $\text{Ar}^{+*}$  and  $\text{Ar}^{2+}$  states are excited by runaway electrons in the negative glow zone. Actually,  $\text{Ar}^{+*}$  states have a very short lifetime due to the fast collisional quenching cascades  $\text{Ar}^{+*} + \text{Ar} \rightarrow \text{Ar}^+ + \text{Ar}$ . According to [113], the rate constant of this reaction is estimated as  $1\text{--}10 \times 10^{-10} \text{ cm}^3 \text{ s}^{-1}$ . Moreover, low-lying excited  $\text{Ar}^{+*}$  states decay also by fast resonant radiative transitions [44], which are not reabsorbed in the gas (the density of  $\text{Ar}^+$  ions is rather low). If the proposed in [23, 105, and 106] reaction scheme  $\text{Ar}^{+*} + 2\text{Ar} \rightarrow \text{Ar}_2^{+*} + 2\text{Ar}$  is correct, the emission of  $\text{Ar}_2^{+*}$  species would be very weak and fast. The experimentally observed long time behaviours of the third continuum emission is compatible only with a relatively long-lived precursor, such as  $\text{Ar}^{2+}$ .

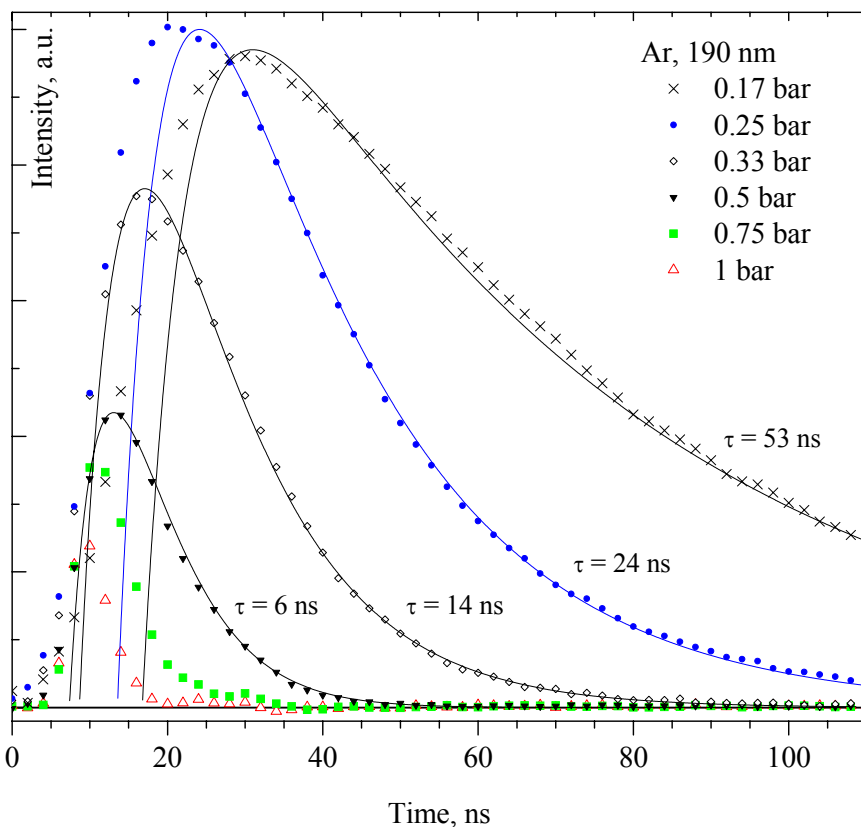
## 7.4. The modeling of the third continuum emission kinetics

Figure 39 shows the temporal evolution of the emission, measured at 190 nm at different pressures, with the subtraction of the background, originating from the photorecombination continuum. The latter one has the emission duration of about 5–8 ns, slightly dependent on the gas pressure. However, the kinetics of the third continuum accelerates with the pressure due to the square dependence on the gas density for the reaction (14) and at 1 bar practically coincides with the photorecombination pulse. To explain these temporal behaviours, a simulation was carried out according to reactions (14) and (15)

$$\frac{d[\text{Ar}_2^{2+}]}{dt} = k_1[\text{Ar}^{2+}][\text{Ar}]^2 - k_2[\text{Ar}_2^{2+*}] \quad (17)$$

A single short excitation pulse was used in the model. Rate constants  $k_1$  and  $k_2$  were used as independent fitting parameters for the modeling of experimental points in Fig. 39. The theoretical kinetics (solid curves in Fig. 39) show rather good coincidence to the experimental points with the exception of the build-up front, as the kinetics of  $\text{Ar}^{2+}$  ions formation during the breakdown pulse was not taken into account. The best fitted theoretical curves were obtained for  $k_1 = 1.23 \times 10^{-30} \text{ cm}^6 \text{ s}^{-1}$  and  $k_2 = 1.75 \times 10^8 \text{ s}^{-1}$  constants. These parameters are very close to the values, measured for reactions (14) and (15) for  $\alpha$ -particles [114] and heavy ions [22] excitations.

The emission band at about 220 nm, which appears at elevated pressures on the spectra in Fig. 35, could belong to  $\text{Ar}_3^{2+}$  trimers, which are created from  $\text{Ar}_2^{2+}$  excimers by the fast reaction  $\text{Ar}_2^{2+} + 2\text{Ar} \rightarrow \text{Ar}_3^{2+} + \text{Ar}$ . The same presumed assignment is presented in several other publications [90, 107]. In present experiments, the kinetics of the emission at 220 nm are similar with the 190 nm band, which means that  $\text{Ar}_3^{2+}$  trimers are not stable and their decay occurs faster than their formation.



**Figure 39.** Temporal behaviour of the third continuum 190 nm band in Ar at different gas pressures. The solid lines for pressures of 0.17–0.5 bar correspond to the model calculations according to equation (17)

## 7.5. Emission of 190 nm band in the afterglow stage

It should be noted that a similar band at 190 nm was detected in paper [115] not only during the excitation pulse, but also in the afterglow stage of the barrier discharge at high Ar pressure. The origin of this afterglow emission was not definitely established in [115]. As was revealed in the present experiments (see Fig. 40), the late afterglow emission at 190 nm as well as at 260 nm bands was detected only in the condition without gas flow through the getter cleaning system. The spectral shape of these afterglow bands did not change with the pressure in the range of 0.5–8 bar. Moreover, the shape of the 190 nm afterglow band is slightly different from the true third continuum band. The left side of both bands in Fig. 40 is somewhat distorted by the silica window of the photomultiplier. As it was established in present imaging experiments with the ICCD camera, the afterglow bands are emitted from the positive column of the

discharge, not from the negative glow zone, as in the case of the true third continuum.

To verify the nature of this emission, the calibrated amounts ( $\sim 10^{-2}$ –1 mbar) of several gas impurities such as O<sub>2</sub>, N<sub>2</sub>, NO, and CO were specially added, but no correlated increase in these bands was observed. For example, with an addition of O<sub>2</sub>, the band at 190 nm disappeared totally and the well-known ArO\* bands [116, 117] at 185 nm (FWHM 3 nm) and 205 nm (FWHM 7–9 nm) were detected in the spectra. Additives of NO led to a shortening of the emission kinetics of the afterglow 190 nm band without any rise in its intensity, which indicated to an accelerated quenching of Ar\*, Ar<sub>2</sub>\* species by NO additives. The presence of N<sub>2</sub> and CO additives up to 1 mbar has no influence on the kinetics of the afterglow 190 nm band. It was revealed also that traces of H<sub>2</sub>O vapours can't be the reason of this band in the experiments. It is expected that the possible origin of 190 nm and 260 nm afterglow bands could be connected with the traces of carbon-containing contaminants, which accumulate inside the discharge chamber. Energy transfer reactions of these contaminants with long-lived Ar\* and Ar<sub>2</sub>\* excited species could be the reason of fluorescence in the afterglow plasma.

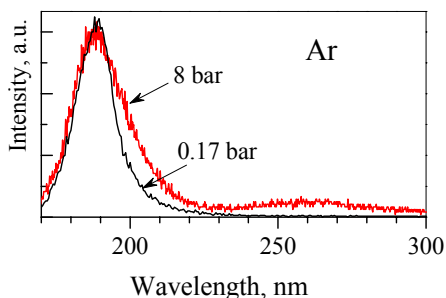


**Figure 40.** Emission spectra, measured at two different conditions: 0.17 bar of Ar, the time point  $t = 30$  ns in Fig. 39, with gas circulation through the getter; 8 bar of Ar, late afterglow stage, without gas circulation through the getter.

## SUMMARY

The aim of the present theses is the experimental and modeling study of high-pressure (up to 10 bar) argon plasma under the high-power pulsed volume discharge excitation to reveal the electron-assisted processes (excitation, recombination, mixing, quenching), which have influence on the production of  $\text{Ar}_2^*$  excimers and VUV-VIS emission of plasma in the breakdown and recombination stages of the discharge.

Spatial-time VUV-VIS spontaneous emission of the discharge plasma and dye laser absorption probing data were used for the diagnostics. The quality of the discharge was monitored by VUV-VIS imaging techniques with ns-time resolution. Quantitative experimental data about densities of key excited atomic and molecular species have been obtained for the estimation of the discharge pumping efficiency and how close to the lasing threshold conditions we are able to approach in the real discharge devices.

The main results of the present study are the following:

- Homogeneous volume discharge in Ar at pressure from 0.17 to 10 bar has been obtained.
- The VUV  $\text{Ar}_2^*$  excimer emission at 127 nm and  $\text{Ar}^{**}$  red lines had a uniform distribution across the positive column of the discharge. As for the UV-VIS continuum, it was emitted very uniformly from the positive column at the breakdown stage of the discharge, but at the high-current regime it was concentrated mainly in the negative glow zone.
- The passing of the discharge from the uniform stage to the constricted one was detected by the change in the spectral shape of the UV-VIS continuum. This spectral transformation is explained by the difference in the positive charge carriers in the arc (atomic  $\text{Ar}^+$  ions) and homogeneous (molecular  $\text{Ar}_2^+$  ions) phases of the discharge. It is suggested that on the analogy of atomic  $\text{Ar}^+$  ions, the electron could be captured by molecular  $\text{Ar}_2^+$  ion and transferred into an  $\text{Ar}_2^*$  energy level with the emission of a photon:  $\text{Ar}_2^+ + e \rightarrow \text{Ar}_2^* + h\nu$ . The intensity of this photorecombination continuum is proportional to the square of the electron density. The emission kinetics of  $\text{Ar}^{**}$  red lines and UV-VIS photorecombination continuum reflected the loss of electrons by dissociative recombination in the afterglow plasma.
- The temporal behaviours of the absolute densities of  $\text{Ar}^*$  (4s, 4p) and  $\text{Ar}_2^* \ ^3\Sigma_u^+(v=0)$  excited species in the discharge were measured by the absorption probing technique. For the theoretical description, the kinetic model, including the main reactions in the discharge plasma, has been created. The experimentally obtained kinetics of excited species were compared with the calculated ones. It was shown, that secondary discharge excitation pulses have a strong influence on the emission kinetics – modulation of the VUV  $\text{Ar}_2^*$  emission is in the opposite phase with the emission of UV-VIS continuum and  $\text{Ar}^{**}$  red lines. The maxima of the VUV

radiation occur when the voltage between the electrodes is zero and minima are observed when the voltage achieves local maxima.

- The experimental data and modeling show that the heating of electrons during the secondary discharge pulses is a very undesirable process. It suppresses the recombination flow in plasma and, as a result, the kinetics of all excited species are spread in time with the decrease of the peak values of their densities. The model predicts that VUV (127 nm) emission is saturated, if the peak electron density exceeds  $10^{17} \text{ cm}^{-3}$ . It was revealed that the main mechanism responsible for the production of  $\text{Ar}_2^* \ ^1\Sigma_u^+ (v=0)$  excimers is the electron collision-induced mixing of triplet and singlet states of  $\text{Ar}_2^*$  excimers. For  $\text{Ar}_2^*$  excimer molecules, used as an active medium for VUV laser, the realistic threshold density of  $\text{Ar}_2^* \ ^1\Sigma_u^+ (v=0)$  excimers is estimated to be about  $5 \times 10^{15} \text{ cm}^{-3}$  for the gain of  $0.05 \text{ cm}^{-1}$ , which is feasible in the case of single-pulse discharge pumping with the peak electron density of  $2.4 \times 10^{16} \text{ cm}^{-3}$  and gas pressure of 10 bar.
- The third continuum band of argon at 190 nm in a pulsed volume discharge was observed at reduced gas pressure. The spatial-time kinetics and spectral transformation of the third continuum were measured and analyzed at different pressures. Time-resolved imaging experiments with ICCD camera have shown that the third continuum and  $\text{Ar}^{+*}$  lines are emitted exclusively from the negative glow zone. The emission of  $\text{Ar}^{+*}$  lines is observed only during the excitation pulse, but the third continuum emission exhibits a behaviour, typical to plasma-chemical kinetics. These facts indicate the existence of runaway electrons, accelerated in the electric field of the cathode layer and retarded in the negative glow zone. The runaway electrons can achieve the energy of the cathode fall potential (130–250 eV) and create  $\text{Ar}^{2+}$  ions in the negative glow zone. The radiative decay of  $\text{Ar}_2^{2+}$  ions, created from  $\text{Ar}^{2+}$  precursors, is modeled and compared with experiment. The results support the assignment of the third continuum to the emission of  $\text{Ar}_2^{2+}$  ionic excimers.

## SUMMARY IN ESTONIAN

Töö pealkiri: “Kõrgrõhu impulss-gaaslahendus argoonis: spektroskoopiline diagnostika, modelleerimine ja arendus”.

Käesoleva väitekirja eesmärgiks on argooni suure võimsusega impulssruumilahenduse kõrgrõhuplasma (kuni 10 bar) eksperimentaalne uurimine ja teoreetiline modelleerimine, et välja selgitada elektronidega seotud protsesside (ergastamine, rekombinatsioon, segunemine, kustutamine), millel on mõju  $\text{Ar}_2^*$  eksimeride tekkimisele ja vaakuumultravioletse-nähtava (VUV-VIS) plasma kiirgusele lahenduse läbilöögi ja rekombinatsiooni staadiumis.

Ruumilis-ajaliselt lahutatud VUV-VIS lahendusplasma spontaanse kiirguse mõõtmise ning värvlaseri neeldumissondeerimise andmeid on kasutatud lahenduse diagnostikaks. Lahenduse kvaliteeti jälgiti ICCD kaamera abil, mis võimaldas fikseerida protsesse VUV-VIS piirkonnas ns lahutusega. On saadud kvantitatiivsed eksperimendi andmed peamiste ergastatud atomaarsete ja molekulaarsete osakeste tiheduse kohta lahenduses. Neid andmeid on kasutatud pumpamise efektiivsuse hindamiseks. Samuti on hinnatud, kui lähedale generatsiooni lävele on võimalik saada kasutades reaalselt elektrilahendus-seadet.

Käesoleva töö põhitulemused on järgmised:

- On saadud homogeenne ruumilahendus argoonis rõhuvahemikus 0.17–10 bar.
- $\text{Ar}_2^*$  eksimeri VUV kiirgus 127 nm juures ja  $\text{Ar}^{**}$  punased jooned olid ühtlase jaotusega piki lahenduse positiivset sammast. Läbilöögi staadiumis kiirgus laia spektriga UV-VIS kontiinum väga homogeenest positiivsest sambast, kuid tugevvoolu staadiumis koondus see peamiselt huumhelenduse tsooni.
- Lahenduse üleminek ühtlasest kokkutõmbunuks on detekteeritud UV-VIS kontiinuumi spektraalse kuju muutumise järgi. Sellist spektraalset muutust seletatakse erinevate positiivse laengu kandjatega kaarlahenduse (atomaarsed  $\text{Ar}^+$  ioonid) ja ühtlase lahenduse (molekulaarsed  $\text{Ar}_2^+$  ioonid) faasis. On oletatud, et analoogiliselt atomaarsele  $\text{Ar}^+$  ioonidele võib elektron olla haaratud molekulaarse  $\text{Ar}_2^+$ iooni poolt, millega kaasneb footoni kiirgumine ning  $\text{Ar}_2^*$  moodustumine:  $\text{Ar}_2^+ + e \rightarrow \text{Ar}_2^* + hv$ . Fotorekombinatsiooni kontiinuumi intensiivsus on võrdeline elektronide tiheduse ruuduga. Punaste  $\text{Ar}^*$  joonte kiirguse kineetika koos UV-VIS fotorekombinatsiooni kontiinuumi kineetikaga kajastavad elektronide kadu dissotsiatiivse rekombinatsiooni tõttu järelhelenduse plasmas.
- Ergastatud osakeste  $\text{Ar}^*$  (4s, 4p) ja  $\text{Ar}_2^* \ ^3\Sigma_u^+ (v=0)$  absoluutsete tiheduste ajaline käik lahenduses on mõõdetud neeldumise teel. Teoreetiliseks kirjeldamiseks on loodud kineetiline mudel, mis haarab lahendusplasmas toimuvaid peamisi reaktsioone. Eksperimendis mõõdetud ergastatud osakeste kineetilised kõverad on kooskõlas arvatud kõveratega. On näidatud, et lahenduse järgnevatel ergastusimpulssidel on oluline mõju kiirgumise

kineetikale –  $\text{Ar}_2^*$  VUV kiirguse modulatsioon on vastandfaasis võrreldes UV-VIS fotorekombinatsiooni kontiinuumi ja  $\text{Ar}^{+*}$  punaste joonte kiirgusega. VUV kiirgus on suurim hetkel, kui elektrodidevaheline pinge läbib nulli ja väikseim hetkel, kui pinge on maksimaalne.

- Eksperimentaalsed andmed ja mudelarvutus näitavad, et elektronide kuumenemine järgnevatel lahedusimpulsside vältel on väga ebasoovitav protsess. See surub alla rekombinatsioonivoo plasmas, mistõttu kõikide ergastatud osakeste aegsõltuvused jaotuvad ümber pikemale ajavahemikule vähendades osakeste tihedust. Mudel ennustab VUV kiirguse ( $\lambda = 127 \text{ nm}$ ) intensiivsuse küllastatust, kui elektronide tihedus ületab  $10^{17} \text{ cm}^{-3}$ . On selgitatud, et peamine mehhanism, mis vastutab  $\text{Ar}_2^* \ ^1\Sigma_u^+ (v=0)$  eksimeride tekkimise eest, on  $\text{Ar}_2^*$  triplett- ja singlett-seisundite segunemine põrgetel elektronidega. Realistlik lävitihedus VUV laseri genereerimiseks  $\text{Ar}_2^* \ ^1\Sigma_u^+ (v=0)$  eksimeride jaoks on hinnangu järgi umbes  $5 \times 10^{15} \text{ cm}^{-3}$ , kui eeldada  $0.05 \text{ cm}^{-1}$  võimendust. Selline eksimeride tihedus on saavutatav elektrilahenduse pumpamise korral üksikimpulssiga, kui elektronide tihedus on  $2.4 \times 10^{16} \text{ cm}^{-3}$  ja gaasi rõhk on 10 bar.
- Madalama gaasi rõhu korral ilmub argooni impulss-ruumilahenduse spektris kolmas kontiinum maksimumiga 190 nm juures. On mõõdetud ja analüüsitud erinevatel rõhkudel selle kontiinuumi ruumilis-ajalist kineetikat ja spektraalset muundumist. Kujutise registreerimisel põhinevad eksperimendid ICCD kaamera abil näitasid, et kolmas kontiinum ja  $\text{Ar}^{+*}$  jooned kiiratakse eranditult huumhelenduse tsoonist.  $\text{Ar}^{+*}$  joonte kiirgus avaldub ainult ergastusimpulsi kestel, aga kolmanda kontiinuumi kiirgus esineb ka hiljem. Need faktid näitavad ärajooksvate elektronide olemasolu, mis kiirenduvad katoodikihi elektriväljas ning pidurduvad huumhelenduse tsoonis. Ärajooksvad elektronid võivad saavutada katoodilähisele pingelangule vastava energia (130–250 eV) ning tekitada  $\text{Ar}^{2+}$  ioone huumhelenduse tsoonis.  $\text{Ar}^{2+}$  prekursor-ioonidest tekkinud  $\text{Ar}_2^{2+}$  ionide kiirguslik lagunemine on modelleeritud kineetiliselt ja võrreldud eksperimendiga. Tulemused kinnitavad, et kolmanda kontiinuumi kiirguse annavad  $\text{Ar}_2^{2+}$  ionid.

## **ACKNOWLEDGEMENTS**

I have a great pleasure to thank people, who worked together with me, and the organizations, which contributed to the completion of this thesis.

First of all I wish to thank my supervisor Head of Laboratory of Laser Techniques Dr. Alexey Treshchalov for introducing me to the fascinating topics of gas discharge plasma, for initiating all these investigations, continuous support, help and advices. Working with him was useful, memorable and very pleasant experience.

I would like to express my words of acknowledgement to engineers of Laboratory of Laser Techniques Sergey Tsarenko, Aavo Kippasto and Vladimir Tsubin for technical support and elegant engineer solutions without which the productive experimental work would be impossible. I am grateful to Dr. Viktor Peet and Dr. Erko Jalviste for many useful advices, support, teaching and help. Next, I would like to say words of acknowledgements to Dr. Alexey Krasnikov and Dr. Veera Krasnenko for being my friends and for help.

I would be glad to thank Prof. Reinhold Hallin from the Angström Laboratory, University of Upsala, Sweden and D. Sc. Boris Krylov from S. I. Vavilov State Optics Institute, Sankt-Petersburg, Russia for useful collaboration and memorable and pleasant experience that I have received during my working in the Angström Laboratory.

In addition, I would like to mention separately Dr. Lilli Paama, Dr. Marco Kirm and Prof. Jaak Kikas for organizing of Doctoral School of Material Science and Material Technologies that allowed me to participate in the international conferences and Summer School for Plasma Physics in Bad Honnef, Germany.

I report my acknowledgements to Estonian Science Foundation for financial support during all these years.

I am also very thankful to my family for support and help.

## REFERENCES

- [1] B. Eliasson and U. Kogelschatz, *IEEE Trans. on Plas. Sci.* **19**, 309 (1991).
- [2] S. Kubodera, M. Kitahara, J. Kawanaka, W. Sasaki and K. Kurosawa, *Appl. Phys. Letters* **69**, 452 (1996)
- [3] A. A. Lisenko, M. I. Lomaev, V. S. Skakun and V. F. Tarasenko, *Phys. Scr.* **76**, 211 (2007)
- [4] G. N. Gerasimov, *Physics-Uspeski* **47**, 149 (2004).
- [5] A. Morozov, T. Heindl, R. Krücken, A. Ulrich, and J. Wieser, *J. Appl. Phys.* **103**, 103301 (2008)
- [6] N. G. Basov, A. V. Danilychev, Y. M. Popov and D. D. Khodkevich, *JETP Letters* **12**, 329 (1970)
- [7] H. A. Koehler, L. J. Ferderber, D. L. Redhead and P. J. Ebert, *Appl. Phys. Letters* **21**, 198 (1972)
- [8] J. B. Gerardo and A. W. Johnson, *IEEE J. Quant. Elect.* **QE-9**, 748 (1973)
- [9] P. W. Hoff, J. C. Swingle and C. K. Rhodes, *Optics Comm.* **8**, 128 (1973)
- [10] P. W. Hoff, J. C. Swingle and C. K. Rhodes, *Appl. Phys. Letters* **23**, 245 (1973)
- [11] W. M. Hughes, J. Shannon and R. Hunter, *Appl. Phys. Letters* **24**, 488 (1974)
- [12] T. Sakurai, N. Goto and C. E. Webb, *J. Phys. D: Appl. Phys.* **20**, 709 (1987)
- [13] H. Ninomiya and K. Nakamura, *Opt. Commun.* **134**, 521 (1997)
- [14] S. K. Lam, D. Lo, C. E. Zheng, C. L. Yuan, C. Shangguan, T. L. Yang and I. V. Kochetov, *Appl. Phys. B: Lasers Opt.* **75**, 723 (2002)
- [15] O. A. Zakharenko, A.A. Kuznetsov, V. N. Slinko and S. S. Sulakshin, *Sov. J. Quantum Electron.* **20**, 813 (1990)
- [16] S. K. Hong, N. Hayashi, S. Ihara, S. Satoh, C. Yamabe and S. B. Wee, *Opt. Commun.* **256**, 149 (2005)
- [17] K. Nakamura, Y. Ooguchi, N. Umegaki, T. Goto, T. Jitsuno, T. Kitamura, M. Takasaki and S. Horiguchi, *Proc. SPIE* **4747**, 286 (2002)
- [18] W. Sasaki, T. Shirai and S. Kubodera, *Opt. Lett.* **26**, 503 (2001)
- [19] R. Sauerbrey, F. Emmert, and H. Langhoff, *J. Phys. B* **17**, 2057 (1984)
- [20] G. S. Hurst, T. E. Bortner, and T. D. Strickler, *Phys. Rev.* **178**, 4 (1969)
- [21] T. Griegel, H. W. Drotleff, J. W. Hammer, and K. Petkau, *J. Chem. Phys.* **93**, 4581 (1990)
- [22] W. Krötz, A. Ulrich, B. Busch, G. Ribitzki, and J. Wieser, *Phys. Rev. A* **43**, 6089 (1991)
- [23] G. Klein and M. J. Carvalho, *J. Phys. B* **14**, 1283 (1981)
- [24] A. Ulrich, A. Görtler, G. Kornfeld, R. Krücken, A. Morozov, F. Mühlberger, A. Peters, R. Steinhübl, J. Wieser, R. Zimmermann, *Proc. ICPIG XXVI* **3**, 245 (2003)
- [25] N. Thonnard and G.S. Hurst, *Phys. Rev.* **5**, 1110 (1972)
- [26] R. S. Mulliken, *J. Chem. Phys.* **52**, 5170 (1970)
- [27] D. C. Lorents, *Physica* **82C**, 19 (1976).
- [28] D. C. Lorents, R.E. Olson and G.M. Conklin, *Chem. Phys. Letter* **20**, 589 (1973)
- [29] T. L. Gilbert and A.C. Wahl, *J. Chem. Phys.* **55**, 5247 (1971)
- [30] S. O. Colgate, J.E. Jordan, I. Amdur and E.A. Mason, *J. Chem. Phys.* **51**, 968 (1969)
- [31] I. M. Parson, P. E. Siska and Y. T. Lee, *J. Chem. Phys.* **56**, 1511 (1972)

- [32] K. Gillen, R. Saxon, D. C. Lorents, G. Lee and R.E. Olson, *IX International Conference on the Physics of Electronic and Atomic Collisions*, J.S. Risley and R. Geballe, eds., University of Washington Press, Seattle (1975)
- [33] S. Neeser, T. Kunz and H. Langhoff, *J. Phys. D: Appl. Phys.* **30**, 1489 (1997)
- [34] A. Fedenev, A. Morozov, R. Krücken, S. Schoop, J. Wieser and A. Ulrich, *J. Phys. D: Appl. Phys.* **37**, 1586 (2004)
- [35] T. Möller, J. Stapelfeldt, M. Beland and G. Zimmerer, *Chem. Phys. Lett.* **117**, 301 (1985)
- [36] M. Kaku, T. Higashieuchi, S. Kubodera, W. Sasaki, *Phys. Rev. A: Atomic, Molecular, and Optical Physics* **68**, 238031 (2003)
- [37] M. Katto, M. Kaku, K. Oda, T. Kamikihara, A. Yokotani, S. Kubodera, N. Miyanaga and K. Mima, *Proc. of SPIE* **7196**, 71960L (2009)
- [38] Y. P. Raizer, *Gas Discharge Physics* (Springer, New York, 1991)
- [39] A. Fridman and L. A. Kennedy, *Plasma Physics and Engineering* (Taylor & Francis, London, 2004).
- [40] Yu. D. Korolev and G. A. Mesiats, *Physics of Pulsed Gas Breakdown* (Moscow: Nauka, 1991)
- [41] *Spectroscopy of gas discharge plasma*, Ed. by S. E. Frish (Nauka, Leningrad, 1970) [in Russian]
- [42] J. W. Keto and C.-Y. Kuo, *J. Chem. Phys.* **74**, 6188 (1981)
- [43] R. S. F. Chang and D. W. Setser, *J. Chem. Phys.* **69**, 3885 (1978)
- [44] W. L. Wiese, M. W. Smith and B. M. Miles, *Atomic Transition Probabilities vol 2* (Washington DC: National Bureau of Standards), pp. 187–200 (1966)
- [45] C. Shannon and J.G. Eden, *J. Chem. Phys.* **89**, 6644 (1988)
- [46] N. Conrad, W. Giessl, C. Leisner, R. Tietz, H. Langhoff, *Z. Phys. D – Atoms, Molecules and Clusters* **16**, 71 (1990)
- [47] D. J. Kane, S. B. Kim, D. C. Shannon, C. M. Herring and J. G. Eden, *J. Chem. Phys.* **96**, 6407 (1992)
- [48] T. Kunz, S. Neeser, H. Langhoff, *Z. Phys. D.* **42**, 101 (1997)
- [49] F. H. Mies, *Mol. Phys.* **26** 1233 (1973)
- [50] O. Cheshnovsky, B. Raz and J. Jortner, *Chem. Phys. Lett.* **15**, 475 (1972)
- [51] P. Dube, M. J. Kiik and B. P. Stoicheff, *J. Chem. Phys.* **103**, 7708 (1995)
- [52] *Excimer Lasers*, Ed. by C. K. Rhodes (Springer, Berlin, 1979; Mir, Moscow, 1981)
- [53] A. Treshchalov, *Proc. Int. Symp. on High Pressure Low Temperature Plasma Chemistry HAKONE VI (Cork, Ireland)*, p. 298 (1998)
- [54] V. I. Gibalov and G. J. Pietsch, *J. Phys. D: Appl. Phys.* **33**, 2618 (2000)
- [55] A. Treshchalov, E. Jalviste, A. Smerechuk, G. Gerasimov, R. Hallin, A. Arnesen, *Proc. Int. Symp. on High Pressure Low Temperature Plasma Chemistry HAKONE VIII, (Tartu, Estonia)*, p. 291 (2002)
- [56] G. Gerasimov, R. Hallin, B. Krylov, A. Treshchalov, A. Morozov, A. Lissovski, G. Zwereva and A. Arnesen, *Proc. SPIE* **6263**, 626311 (2006)
- [57] M. Young, *Appl. Optics* **10**, 2763 (1971)
- [58] R. Dreiskemper, G. Schröder and W. Bötticher, *IEEE Trans. Plasma Sci.* **23**, 180 (1995)
- [59] R. Dreiskemper and W. Bötticher, *IEEE Trans. Plasma Sci.* **23**, 987 (1995)
- [60] S. Chen and C.P. Grigoropoulos, *Appl. Phys. Lett.* **71**, 3191 (1997)
- [61] A. Anders, S. Anders, M. A. Gundersen, *J. Appl. Phys.* **76**, 1494 (1994)
- [62] Yu.D. Korolev and K. Frank, *IEEE Trans. Plasma Sci.* **27**, 1525 (1999)

- [63] A.V. Phelps and Z. Lj. Petrovic, *Plasma Sources Sci. Technol.* **8**, R21 (1999)
- [64] S. O. Macheret, M. N. Shneider and R. C. Murray, *Phys. Plasmas* **13**, 023502 (2006)
- [65] D. S. Nikandrov, L. D. Tsendin, V. I. Kolobov and R. R. Arslanbekov, *IEEE Trans. Plasma Sci.* **36**, 131 (2008)
- [66] V. Yu. Kozhevnikov, A. V. Kozyrev and Yu. D. Korolev *Plasma Phys. Rep.* **32**, 949 (2006)
- [67] M. A. Lieberman and A. J. Lichtenberg, *Principles of Plasma Discharges and Materials Processing* 2nd edn. (New York: Wiley 2005)
- [68] H. R. Griem, *Spectral Line Broadening by Plasmas* (New York: Academic 1974)
- [69] A. Batal, J. Jarosz and J. M. Mermet, *Spectrochim. Acta B* **36**, 983 (1981)
- [70] J. M. de Regt, J. Van Dijk, J. A. M. van der Mullen and D. C. Schram, *J. Phys. D: Appl. Phys.* **28**, 40 (1995)
- [71] A. T. M. Wilbers, G. M. W. Kroesen, C. J. Timmermans and D. C. Schram, *J. Quant. Spectrosc. Radiat. Transfer* **45**, 1 (1991)
- [72] J. Park, I. Henins, H. Herrmann and G. Selwyn, *Phys. Plasmas* **7**, 3141 (2000)
- [73] A. Rutscher and S. Pfau, *Physica C* **81**, 395 (1976)
- [74] J. Jonkers, M. van de Sande, A. Sola, A. Gamero, A. Rodero and J. van der Mullen
- [75] N. A. Dyatko, Y. Z. Ionikh, I. V. Kochetov, D. L. Marinov, A. V. Meshchanov, A. P. Napartovich, F. B. Petrov and S. A. Starostin, *J. Phys. D: Appl. Phys.* **41**, 055204 (2008)
- [76] W.-C. F. Liu and D. C. Conway, *J. Chem. Phys.* **62**, 3070 (1975)
- [77] F. J. Mehr and M. A. Biondi, *Phys. Rev.* **176**, 322 (1968)
- [78] V. S. Marchenko, *Sov. Phys.—JETP* **58**, 292 (1983)
- [79] A. Treshchalov, A. Lissovski and E. Chikeev, *Proc. SPIE* **4747**, 253 (2002)
- [80] Ya. B. Zel'dovich and Yu. P. Raizer, *Physics of Shock Waves and High-Temperature Hydrodynamic Phenomena* (New York and London: Academic 1966)
- [81] C. Duzy and H. A. Hyman, *Phys. Rev. A* **22**, 1878 (1980)
- [82] L. G. D'yachkov, Y. K. Kurilenkov and Y. Vitel, *J. Quant. Spectrosc. Radiat. Transfer* **59**, 53 (1998)
- [83] A. Bogaerts, *J. Anal. At. Spectrom.* **22**, 502 (2007)
- [84] M. A. Biondi, *Applied Atomic Collision Physics. Vol 3: Gas Lasers* ed. E. W. McDaniel and W. L. Nighan (New York: Academic 1982) chapter 6
- [85] Y.-J. Shiu and M. A. Biondi, *Phys. Rev. A* **17**, 868 (1978)
- [86] C.-Y. Kuo and J. W. Keto, *J. Chem. Phys.* **78**, 1851 (1983)
- [87] A. Bogaerts and R. Gijbels, *Phys. Rev. A* **52**, 3743 (1995)
- [88] C. M. Herring, S. B. Kim, J.G. Eden, M.L. Ginter, *J. Chem. Phys.* **101**, 4561 (1994)
- [89] I. K. Bronic and M. Kimura, *J. Chem. Phys.* **104**, 8973 (1996)
- [90] E. Robert, A. Khacef, C. Cachoncinlle and M. Pouvesle, *IEEE J. Quantum Electron.* **33**, 2119 (1997)
- [91] L. Goubert, E. Desoppere, W. Wieme, R. Pol'ak, I. Paidarov'a and G. D. Billing, *J. Phys. Chem.* **99**, 15479 (1995)
- [92] V. M. Donnelly, *J. Phys. D: Appl. Phys.* **37**, R217 (2004)
- [93] S. K. Lam, C.-E. Zheng, D. Lo, A. Dem'yanov and A. P. Napartovich, *J. Phys. D: Appl. Phys.* **33**, 242 (2000)

- [94] A. Yanguas-Gil, J. Cotrino and L. L. Alves, *J. Phys. D: Appl. Phys.* **38**, 1588 (2005)
- [95] P. Millet, A. Birot, H. Brunet, H. Dijols, J. Galy and Y. Salamero, *J. Phys. B: At. Mol. Phys.* **15**, 2935 (1982)
- [96] H. H. Michels, R. H. Hobbs and L. A. Wright, *J. Chem Phys.* **71**, 5053 (1979)
- [97] K. J. McCann and M. R. Flannery, *Appl. Phys. Lett.* **31**, 599 (1977)
- [98] R. Sauerbrey, *IEEE J. Quantum Electron.* **23**, 5 (1987)
- [99] S. Neeser, M. Schumann and H. Langhoff, *Appl. Phys. B:Lasers Opt.* **63**, 103 (1996)
- [100] W.-G. Wrobel, H. Röhr and K.-H. Steuer, *Appl. Phys. Lett.* **36**, 113 (1980)
- [101] A. Ulrich, H. J. Körner, W. Krötz, and G. Ribitzki, *J. Appl. Phys.* **62**, 357 (1987)
- [102] C. L. Cocke, *Phys. Rev. A* **20**, 749 (1979)
- [103] J. A. Syage, *J. Phys. B* **24**, L527 (1991)
- [104] H. Langhoff, *Opt. Commun.* **68**, 31 (1988)
- [105] A. K. Amirov, O. V. Korshunov, and V. F. Chinnov, *J. Phys. B* **27**, 1753 (1994)
- [106] A. M. Bojchenko, V. F. Tarasenko, and S. I. Yakovlenko, *Laser Phys.* **9**, 1004 (1999)
- [107] J. Wieser, A. Ulrich, A. Fedenev, and M. Salvermoser, *Opt. Commun.* **173**, 233 (2000)
- [108] L. P. Babich, T. V. Loiko, and V. A. Tsukerman, *Usp. Fiz. Nauk* **160**, 49 (1990)
- [109] G. A. Mesyats, *JETP Lett.* **85**, 109 (2007)
- [110] G. A. Mesyats, *Phys. Usp.* **49**, 1045 (2006)
- [111] V. F. Tarasenko, E. K. Baksht, A. G. Burachenko, I. D. Kostyrya, M. I. Lomaev, and D. V. Rybka, *Plasma Devices Oper.* **16**, 267 (2008)
- [112] Y. D. Korolev and G. A. Mesyats, *Field-Emission and Explosive Processes in Gas Discharges* (Nauka, Moscow, 1982)
- [113] H. Langhoff, *J. Phys. B* **27**, L709 (1994)
- [114] A. Birot, H. Brunet, J. Galy, P. Millet, and J. Teyssier, *J. Chem. Phys.* **63**, 1469 (1975)
- [115] C. Cachoncinlle, M. Pouvesle, F. Davanloo, J. J. Coogan, and C. B. Collins, *Opt. Commun.* **79**, 41 (1990)
- [116] S. Neeser, M. Voitik, and H. Langhoff, *J. Chem. Phys.* **102**, 1639 (1995)
- [117] D. E. Johnson, *Chem. Phys. Lett.* **238**, 71 (1995)



## **PUBLICATIONS**

# CURRICULUM VITAE (CV)

## Aleksandr Lissovski

Date and place of birth: 27.01.1979, Narva, Estonia  
Citizenship: Estonian  
Current employment: Institute of Physics, University of Tartu, Laboratory of Laser Techniques (researcher)  
Address: Institute of Physics, University of Tartu, Riia str. 142, 51014 Tartu, Estonia  
Phone: +372 5559 7703  
E-mail: aleks\_ls@fi.tartu.ee

### Education

1986–1997 Narva Pähklikmäe Gymnasium  
1997–2001 B.Sc. in physics, Faculty of Physics and Chemistry, University of Tartu  
2001–2004 M.Sc. in physics (optics and spectroscopy), Faculty of Physics and Chemistry, University of Tartu  
2004–2010 PhD student (optics and spectroscopy), University of Tartu

### Employment

2004–2007 Laboratory of Laser Techniques, Institute of Physics, University of Tartu, engineer  
2007–2010 Laboratory of Laser Techniques, Institute of Physics, University of Tartu, researcher  
2005–2008 Doctoral School of Material Science and Material Technologies, researcher

### Scientific work

Main field of research: physics of gas discharge plasma – electrical and spectroscopic diagnostics and computer modeling  
Publications: 15 scientific articles

### Awards

2005 Best poster prize in “AMPL-VII (Atomic and Molecular Pulsed Lasers)“, September 12–16, 2005, Tomsk, Russia

# ELULOOKIRJELDUS (CV)

## Aleksandr Lissovski

Sünniaeg ja -koht: 27.01.1979, Narva, Eesti  
Kodakondsus: Eesti  
Praegune töökoht: Tartu Ülikooli Füüsika Instituut, Lasertehnika labor,  
erakorraline teadur  
Aadress: Tartu Ülikooli Füüsika Instituut, Riia tn. 142, 51014  
Tartu  
Telefon: +372 5559 7703  
E-post: aleks\_ls@fi.tartu.ee

### Haridus

1986–1997 Narva Pähklimäe Gümnaasium  
1997–2001 B.Sc. füüsikas, Tartu Ülikooli füüsika-keemiateaduskond  
2001–2004 M.Sc. füüsikas (optika ja spektroskoopia), Tartu Ülikooli  
füüsika-keemiateaduskond  
2004–2010 doktorantuur (optika ja spektroskoopia), Tartu Ülikooli  
LOTE teaduskond

### Teenistuskäik

2004–2007 Tartu Ülikooli Füüsika Instituudi Lasertehnika labor,  
insener  
2007– ... Tartu Ülikooli Füüsika Instituudi Lasertehnika labor,  
erakorraline teadur  
2005–2008 Tartu Ülikooli Materjaliteaduse ja Materjalide Tehno-  
loogia Doktorikool, erakorraline teadur

### Teadustegevus

Peamine töosuund: gaaslahendusplasma füüsika – elektriline ja spekt-  
roskoopiline diagnostika ja arvutimodelleerimine  
Publikatsioonid: 15 teaduslikku publikatsiooni

### Teaduspreemiad

2005 Parima stendiettekande preemia konverentsil “AMPL-  
VII (Atomic and Molecular Pulsed Lasers)“, 12–16.  
september, 2005, Tomsk, Venemaa

## DISSERTATIONES PHYSICAE UNIVERSITATIS TARTUENSIS

1. **Andrus Ausmees.** XUV-induced electron emission and electron-phonon interaction in alkali halides. Tartu, 1991.
2. **Heiki Sõnajalg.** Shaping and recalling of light pulses by optical elements based on spectral hole burning. Tartu, 1991.
3. **Sergei Savihhin.** Ultrafast dynamics of F-centers and bound excitons from picosecond spectroscopy data. Tartu, 1991.
4. **Ergo Nõmmiste.** Leelishalogeniidide röntgenelektronemissioon kiiritamisel footonitega energiaga 70–140 eV. Tartu, 1991.
5. **Margus Rätsep.** Spectral gratings and their relaxation in some low-temperature impurity-doped glasses and crystals. Tartu, 1991.
6. **Tõnu Pullerits.** Primary energy transfer in photosynthesis. Model calculations. Tartu, 1991.
7. **Olev Saks.** Attoampri diapsoonis voolude mõõtmise füüsikalised alused. Tartu, 1991.
8. **Andres Virro.** AlGaAsSb/GaSb heterostructure injection lasers. Tartu, 1991.
9. **Hans Korge.** Investigation of negative point discharge in pure nitrogen at atmospheric pressure. Tartu, 1992.
10. **Jüri Maksimov.** Nonlinear generation of laser VUV radiation for high-resolution spectroscopy. Tartu, 1992.
11. **Mark Aizengendler.** Photostimulated transformation of aggregate defects and spectral hole burning in a neutron-irradiated sapphire. Tartu, 1992.
12. **Hele Siimon.** Atomic layer molecular beam epitaxy of  $A^2B^6$  compounds described on the basis of kinetic equations model. Tartu, 1992.
13. **Tõnu Reinot.** The kinetics of polariton luminescence, energy transfer and relaxation in anthracene. Tartu, 1992.
14. **Toomas Rõõm.** Paramagnetic  $H^{2-}$  and  $F^+$  centers in CaO crystals: spectra, relaxation and recombination luminescence. Tallinn, 1993.
15. **Erko Jalviste.** Laser spectroscopy of some jet-cooled organic molecules. Tartu, 1993.
16. **Alvo Aabloo.** Studies of crystalline celluloses using potential energy calculations. Tartu, 1994.
17. **Peeter Paris.** Initiation of corona pulses. Tartu, 1994.
18. **Павел Рубин.** Локальные дефектные состояния в  $CuO_2$  плоскостях высокотемпературных сверхпроводников. Тарту, 1994.
19. **Olavi Ollikainen.** Applications of persistent spectral hole burning in ultrafast optical neural networks, time-resolved spectroscopy and holographic interferometry. Tartu, 1996.
20. **Ülo Mets.** Methodological aspects of fluorescence correlation spectroscopy. Tartu, 1996.
21. **Mikhail Danilkin.** Interaction of intrinsic and impurity defects in CaS:Eu luminophors. Tartu, 1997.

22. **Ирина Кудрявцева.** Создание и стабилизация дефектов в кристаллах KBr, KCl, RbCl при облучении ВУФ-радиацией. Тарту, 1997.
23. **Andres Osvet.** Photochromic properties of radiation-induced defects in diamond. Tartu, 1998.
24. **Jüri Örd.** Classical and quantum aspects of geodesic multiplication. Tartu, 1998.
25. **Priit Sarv.** High resolution solid-state NMR studies of zeolites. Tartu, 1998.
26. **Сергей Долгов.** Электронные возбуждения и дефектообразование в некоторых оксидах металлов. Тарту, 1998.
27. **Каupo Kukli.** Atomic layer deposition of artificially structured dielectric materials. Tartu, 1999.
28. **Ivo Heinmaa.** Nuclear resonance studies of local structure in  $\text{RbBa}_2\text{Cu}_3\text{O}_{6+x}$  compounds. Tartu, 1999.
29. **Aleksander Shelkan.** Hole states in  $\text{CuO}_2$  planes of high temperature superconducting materials. Tartu, 1999.
30. **Dmitri Nevedrov.** Nonlinear effects in quantum lattices. Tartu, 1999.
31. **Rein Ruus.** Collapse of 3d (4f) orbitals in 2p (3d) excited configurations and its effect on the x-ray and electron spectra. Tartu, 1999.
32. **Valter Zazubovich.** Local relaxation in incommensurate and glassy solids studied by Spectral Hole Burning. Tartu, 1999.
33. **Indrek Reimand.** Picosecond dynamics of optical excitations in GaAs and other excitonic systems. Tartu, 2000.
34. **Vladimir Babin.** Spectroscopy of exciton states in some halide macro- and nanocrystals. Tartu, 2001.
35. **Toomas Plank.** Positive corona at combined DC and AC voltage. Tartu, 2001.
36. **Kristjan Leiger.** Pressure-induced effects in inhomogeneous spectra of doped solids. Tartu, 2002.
37. **Helle Kaasik.** Nonperturbative theory of multiphonon vibrational relaxation and nonradiative transitions. Tartu, 2002.
38. **Tõnu Laas.** Propagation of waves in curved spacetimes. Tartu, 2002.
39. **Rünno Lõhmus.** Application of novel hybrid methods in SPM studies of nanostructural materials. Tartu, 2002.
40. **Kaido Reivelt.** Optical implementation of propagation-invariant pulsed free-space wave fields. Tartu, 2003.
41. **Heiki Kasemägi.** The effect of nanoparticle additives on lithium-ion mobility in a polymer electrolyte. Tartu, 2003.
42. **Villu Repän.** Low current mode of negative corona. Tartu, 2004.
43. **Алексей Котлов.** Оксианионные диэлектрические кристаллы: зонная структура и электронные возбуждения. Tartu, 2004.
44. **Jaak Talts.** Continuous non-invasive blood pressure measurement: comparative and methodological studies of the differential servo-oscillometric method. Tartu, 2004.
45. **Margus Saal.** Studies of pre-big bang and braneworld cosmology. Tartu, 2004.

46. **Eduard Gerškevičš.** Dose to bone marrow and leukaemia risk in external beam radiotherapy of prostate cancer. Tartu, 2005.
47. **Sergey Shchemelyov.** Sum-frequency generation and multiphoton ionization in xenon under excitation by conical laser beams. Tartu, 2006.
48. **Valter Kiisk.** Optical investigation of metal-oxide thin films. Tartu, 2006.
49. **Jaan Aarik.** Atomic layer deposition of titanium, zirconium and hafnium dioxides: growth mechanisms and properties of thin films. Tartu, 2007.
50. **Astrid Rekker.** Colored-noise-controlled anomalous transport and phase transitions in complex systems. Tartu, 2007.
51. **Andres Punning.** Electromechanical characterization of ionic polymer-metal composite sensing actuators. Tartu, 2007.
52. **Indrek Jõgi.** Conduction mechanisms in thin atomic layer deposited films containing TiO<sub>2</sub>. Tartu, 2007.
53. **Aleksei Krasnikov.** Luminescence and defects creation processes in lead tungstate crystals. Tartu, 2007.
54. **Küllike Rägo.** Superconducting properties of MgB<sub>2</sub> in a scenario with intra- and interband pairing channels. Tartu, 2008.
55. **Els Heinsalu.** Normal and anomalously slow diffusion under external fields. Tartu, 2008.
56. **Kuno Kooser.** Soft x-ray induced radiative and nonradiative core-hole decay processes in thin films and solids. Tartu, 2008.
57. **Vadim Boltrushko.** Theory of vibronic transitions with strong nonlinear vibronic interaction in solids. Tartu, 2008.
58. **Andi Hektor.** Neutrino Physics beyond the Standard Model. Tartu, 2008.
59. **Raavo Josepson.** Photoinduced field-assisted electron emission into gases. Tartu, 2008.
60. **Martti Pärs.** Study of spontaneous and photoinduced processes in molecular solids using high-resolution optical spectroscopy. Tartu, 2008.
61. **Kristjan Kannike.** Implications of neutrino masses. Tartu, 2008.
62. **Vigen Issahhanjan.** Hole and interstitial centres in radiation-resistant MgO single crystals. Tartu, 2008.
63. **Veera Krasnenko.** Computational modeling of fluorescent proteins. Tartu, 2008.
64. **Mait Müntel.** Detection of doubly charged higgs boson in the CMS detector. Tartu, 2008.
65. **Kalle Kepler.** Optimisation of patient doses and image quality in diagnostic radiology. Tartu, 2009.
66. **Jüri Raud.** Study of negative glow and positive column regions of capillary HF discharge. Tartu, 2009.
67. **Sven Lange.** Spectroscopic and phase-stabilisation properties of pure and rare-earth ions activated ZrO<sub>2</sub> and HfO<sub>2</sub>. Tartu, 2010.
68. **Aarne Kasikov.** Optical characterization of inhomogeneous thin films. Tartu, 2010.

69. **Heli Valtna-Lukner.** Superluminally propagating localized optical pulses. Tartu, 2010.
70. **Artjom Vargunin.** Stochastic and deterministic features of ordering in the systems with a phase transition. Tartu, 2010.
71. **Hannes Liivat.** Probing new physics in  $e^+e^-$  annihilations into heavy particles via spin orientation effects. Tartu, 2010.
72. **Tanel Mullari.** On the second order relativistic deviation equation and its applications. Tartu, 2010.